12-2010

Characteristics and Stability of Oxide Films on Plutonium Surfaces

Harry Guillermo García Flores
University of Nebraska-Lincoln, hggf@unlserve.unl.edu

CHARACTERISTICS AND STABILITY OF OXIDE FILMS ON PLUTONIUM SURFACES

by

Harry G. García Flores

A DISSERTATION

Presented to the Faculty of

The Graduate College at the University of Nebraska

In Partial Fulfillment of Requirements

For the Degree of Doctor of Philosophy

Major: Chemistry

Under the Supervision of Professor Marjorie A. Langell

Lincoln, Nebraska

December, 2010

CHARACTERISTICS AND STABILITY OF OXIDE FILMS ON PLUTONIUM SURFACES

Harry Guillermo García Flores, Ph.D.

University of Nebraska, 2010

Adviser: Marjorie A. Langell

The oxidation of plutonium (Pu) metal continues to be an area of considerable activity. The reaction characteristics have significant implications for production use, storage, and disposition of this radiological material. Developing an accurate physical model of the structures, oxidation states, and oxygen concentration gradients present during oxidation are essential to understanding this process. Traditionally, the stable oxides of Pu have been thought to be plutonium sesquioxide (Pu_2O_3, O/Pu = 1.5, Pu^{3+}) and plutonium dioxide (PuO_2, O/Pu = 2.0, Pu^{4+}), existing in a layered structure on Pu metal. Many of the notions of the layered Pu oxide model are based on extrapolations of data acquired on bulk oxides with only a few supported with results from actual Pu oxide film studies.

This dissertation involves a detailed study using x-ray photoelectron spectroscopy (XPS) and Auger electron spectroscopy (AES) to measure the relative concentrations of oxygen and plutonium, as well as the resulting oxidation states in the near-surface region. A model to fit the XPS data has been developed for the accurate and reliable quantification of oxide film stoichiometries (O^{2-}/Pu^{Tot}), and a relative sensitivity factor

(RSF) has been determined. The influence of temperature, pressure and exposure time on oxide film characteristics was investigated.

The results indicate that, like PuO_2, the sesquioxide is not stable on a clean metal substrate under reducing conditions, resulting in substoichiometric films (Pu_2O_{3-y}). The Pu_2O_{3-y} films prepared exhibit a variety of stoichiometries as a function of preparation conditions. This study show a much greater than anticipated extent of auto-reduction of PuO_2 and challenge the commonly held notion of the stoichiometric stability of Pu_2O_3 thin films, especially in the presence of plutonium metal. The fate of gallium and carbon impurities after oxidation of plutonium surfaces was probed. Both remain at the metal-oxide interface upon oxidation of the metal. A new model of the plutonium/oxygen thin-film system will be proposed and its applicability to thicker-films will be discussed.

Acknowledgements

It has been a long time since this journey began in 1993. After a six year hiatus, I was given a second opportunity in 2005 to return to Nebraska in order to continue my studies. This would not have been possible without my two mentors. Professor Marjorie Langell at the Chemistry Department in Nebraska who took me into her lab and provided me with guidance, encouragement, and gloves and scarves to keep me warm during the winter. Dr. David Pugmire who supervised my work while at Los Alamos National Laboratory (where the investigation presented here was performed) and provided guidance through the myriad safety and security protocols regulating work at a nuclear facility. Thank you, both, for everything. I will always be grateful.

The other members of my Supervisory Committee deserve recognition as well for their time and attention in evaluating this work: Dr. Choe, Dr. Harbison, Dr. Schubert, and Dr. Zeng. A special thanks is warranted for Dr. Harbison who offered useful counsel when I was contemplating a return to Nebraska. Especially the assurance that I would not have to take cum exams again. Two RUI's and two OPO's were not a problem but I do not think I could have handled a second set of those exams...

Several individuals at Los Alamos deserve recognition. Troy Nothwang, Amanda Broach, and Sue Duncan for lending their expertise in the handling of nuclear materials. Not only did they provide assistance in the movement of nuclear material in and out of the instruments but often offered a helping hand in performing instrument maintenance –

and always with a smile. Dr. David Moore's expertise in actinide materials and AES data acquisition/interpretation were invaluable for this work. The plutonium samples studied in this work were graciously provided by Dr. Franz Freibert. Dr. Paul Roussel (AWE in the United Kingdom) needs to be acknowledged for his encyclopedic knowledge of the plutonium literature and his willingness to share it with me –even answering my emails from South Africa while attending the World Cup. I also want to thank Dr. Rollin Lakis who suggested I go back to school and for introducing me to the Los Alamos National Laboratory's Graduate Research Assistance (GRA) program, which supported me during the course of this work.

This document has been reviewed by LANL's SAFE-1 Classification Group and received the following release number: LA-UR-10-07870.

TABLE OF CONTENTS

Chapter 1 : Introduction

1.1 Background

Since the moment it was first isolated by man in February 23, 1941 [1], and sufficient quantities of the metallic form were produced, scientists have been studying the properties of plutonium. Knowledge obtained by scientists during the Manhattan Project was essential if the new element was to be processed, handled, and used for the ultimate goal: a nuclear weapon device. Today, while the primary interest of studying plutonium is still centered on nuclear weapons, peaceful uses of the element have emerged [2].

Fifty years ago, NASA developed radioisotope thermal generators (RTG) that convert the heat from the radioactive decay of plutonium-238 into electricity [3]. Space exploration missions from the historic Pioneer 10 & 11 (the first crafts to explore the edges of interstellar space), the Viking (Mars), and Voyager (outer planets) missions to the more recent Galileo (Jupiter) and Cassini (Saturn & moons) spacecrafts, have all utilized plutonium RTGs to provide the power needed by scientific and communications instrumentations. In all of these cases, crafts have ventured to region of the outer Solar System and beyond, where more conventional energy sources such as solar cells, are impractical.

With the current concerns regarding greenhouse emissions from the combustion of fossil fuels, nuclear energy is experiencing a renaissance. Most of the current nuclear

power production involves the fission of uranium for electricity production. However, plutonium (as well as thorium) can also be utilized for nuclear power. Indeed, Japan routinely sends its spent nuclear rods to Europe for reprocessing and ships the plutonium back to the island to be used in higher 'burnup ratios' reactors [4]. The United States, with its enormous surplus of plutonium from Cold War weapons inventory, has actively invested in technologies to reprocess weapons grade plutonium into a fuel grade mixed oxide (U & Pu) for reactors. Unfortunately, there are no commercial nuclear power reactors capable of burning plutonium fuel in the U.S. That may change in the near future with the recent national energy policy changes emphasizing nuclear energy [5].

An unexpected discovery was made recently regarding plutonium and superconductivity. While probing the magnetic properties of the compound $PuCoGa_5$, measurements revealed diamagnetic behavior, a common indicator of superconductivity; actinide group elements usually form magnetic compounds [6]. Later investigations revealed that for this material, superconductivity is achieved at 18 K, not around 1 K as most metals that are not considered very good superconductors, i.e., the low temperature makes them undesirable for practical applications [7]. According to current theories, due to the magnetic properties of heavy elements in the actinide group, such as plutonium, this class of compounds should not superconduct, suggesting a new superconducting mechanism not explained by current theories. Newer theories dealing with d-wave pairing and spin fluctuation are being formulated to explain the superconductivity properties of actinide elements.

1.2 Properties of Plutonium

From the first observations of the initial few milligrams produced, plutonium has been surprising scientists with its unusual properties. Density measurements provided one of the first indications that plutonium is not your typical metal. Manhattan Project teams at the University of Chicago and at Los Alamos disagreed on the actual density of the new element. The measured values ranged from 12 to 22 g/cm^3 [2]. The fluctuating densities were later determined to be due to the different solid phases of the measured sample. Plutonium undergoes six crystalline phase transitions, as listed on Table 1.1 [8].

Table 1.1: The crystal structures and densities of plutonium metal solid phases [8].

Phase	Crystal Structure	Density (g/cm^3)
α	Simple monoclinic	19.86
β	Face-centered monoclinic	17.70
γ	Face-centered orthorhombic	17.14
δ	Face-centered cubic	15.92
δ'	Body-centered tetragonal	16.00
ε	Body centered cubic	16.51
Liquid		16.65

As the metal is heated, the density of these distinct phases fluctuates by more than 20%. The brittle α-phase, an unusual low-symmetry monoclinic structure stable at room temperature, expands at five times the rate of iron when heated. The high-symmetry, face centered-cubic (fcc) δ-phase, stable at 310^o C [9], contracts with rising temperature. At 640^o C, plutonium melts; the aqueous phase has a high surface tension and the greatest

viscosity of any element in the Periodic Table. The δ-phase of plutonium can be stabilized at room temperature with a small amount (~2%) of gallium or aluminum. Gallium stabilized, δ-phase plutonium metal is a poly-crystalline material, as can be observed in Figure 1.1.

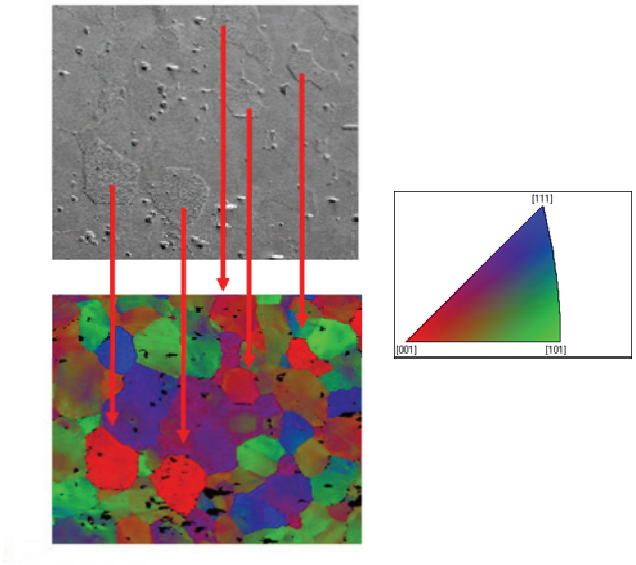

Figure 1.1: Poly-crystalline nature of δ-plutonium metal. An electron micrograph (top left, black/white) shows its multigrain structure. An electron back-scattered diffraction (EBSD) pattern (bottom left, color) of the same surface region contrasts the different domains by color as a function of the crystalline direction shown in the legend (right, colored triangle).

While this fcc (δ) phase is the closest packed structure of the six allotropes, it has the lowest density. The main advantages of stabilizing the δ-phase with gallium are the increased temperature stability range and the increased malleability of an fcc phase vs. monoclinic, which allows for easier machining of the metal.

Plutonium's strange behavior is not confined to the number of crystalline phases it can accommodate. It is a poor electrical and thermal conductor; the electrical resistivity increases as the temperature is lowered to 100 K. This anomalous behavior is generally attributed to the 5f electrons numerous competing states near the ground state and the shape of the 5f band [10].

1.3 Chemistry of Plutonium

As a consequence of the Cold War, the United States and the former Soviet Union account for the vast majority of the environmental releases. Because of different philosophies regarding storage and discharge of radionuclides, the amounts differ (~$2.6*10^6$ Ci in US vs. ~$1.7*10^9$ Ci in USSR) [11]. Not surprisingly, most of the releases occurred around nuclear material complexes. In the US, the Hanford Site and the Savannah River Site are the main centers for reprocessing waste storage. Environmental contamination is a major concern at these sites. Studies have shown that plutonium undergoes numerous reactions in water and with minerals. The low solubility in most natural water bodies and high sorption to minerals create a natural barrier against the spread of accidental spills [11]. The plutonium uptake by plants is very limited (< 0.01%). Since plutonium is an alpha emitter, it must enter the body to deliver a radiation dose. Fortunately, the human body has natural barriers to minimize uptakes of the material. Only 5-25% of the inhaled plutonium is retained in the lungs, lymphs, liver, or bones. Of the ingested plutonium 0.05% enters the blood stream; the rest is excreted. Absorption through skin cuts is a serious danger, particularly to plutonium workers as it

offers a complete retention of plutonium in the body. Very high doses of ionizing radiation, such as those from criticality accidents, are harmful and potentially fatal.

The corrosion chemistry of plutonium has been studied under different conditions in order to ascertain the effect of relative humidity, oxygen content, and temperature (among others) on the extent of the metal surface reaction [12]. While these studies were performed on the different allotropes of plutonium as well, the following discussion will only concern the delta- phase of plutonium. Corrosion of plutonium is of importance because as the metal oxidizes, its surface spallates forming small particles of oxide that are readily dispersible, creating an inhalation hazard that may endanger nuclear workers at the workplace or the general population during an accidental release. In dry air and at room temperature plutonium readily oxidizes forming plutonium oxide layers on the metal. This protective oxide layer grows at a rate of 20 pm/hr [13]. Between PuO_2 and the metal, a thin layer of plutonium sesquioxide (Pu_2O_3) is thought to exist.

The oxidation of plutonium by water vapor is significantly faster than in dry air. At room temperature, the reaction with water vapor (100% relative humidity) is 100 times faster; at 100^{o} C, the corrosion occurs at 100,000 times faster than dry air [14]. Models devised to explain this increased reactivity assumed faster diffusivity of hydroxide ions (OH^-) as the driving force of the enhanced corrosion. Others have invoked a water-mediated catalytic oxidation of plutonium to explain the oxidation behavior [15]. However, little experimental data exists to support the different hypotheses.

In one of the initial investigations of plutonium oxidation, several authors reported on the reactivity of plutonium to inert (argon) atmosphere [16]. Surprisingly, they reported that the plutonium sample gained weight, i.e., oxidized, faster in an inert atmosphere (argon gas) than in an oxygen atmosphere. The explanation stated by the authors is that exposure to oxygen yields a protective layer against further oxidation. They presented additional experiment with varying concentrations of oxygen in argon showing that the rate of the oxidation *decreased* with increasing oxygen content, offering further support to the hypothesis for a protective oxide layer formed by oxygen. It is likely that the perceived higher reactivity to an inert atmosphere was likely due to small amounts of water vapor in the gas.

An important consideration when interpreting historical results of plutonium oxidation and formulating oxidation models is the experimental techniques utilized for these initial studies. Most of the studies involved the measurement of the metal sample weight gain with respect to time [17]. The reaction rate units of measurement were reported as micrograms of weight gained per sample area per minute ($\mu g/cm^2/min$). The initial increases in sample weight were usually several hundreds of micrograms over a period of several hours. When units are converted from weight gain to oxide thickness, the detection limits of the technique is approximately 50 nm. Furthermore, in order to acquire meaningful data with as small noise levels (biggest actual weight increase per unit time) as possible, the weight gains were measured at higher than ambient temperatures where the oxidation rate is faster allowing for more data points within the time of the experiment. These inherent experimental limitations prevented the study of

the initial stages of plutonium oxidation. Additionally, characterization of the original metal surface prior to the oxidation experiments was not possible. Without experimental data of the initial stages of the oxidation of plutonium or information regarding the initial conditions of the metal surface being studied, suggested hypotheses explaining the Pu oxidation kinetics and how it occurs at the atomic level, remained unproven and little more that conjectures.

1.4 Surface Science of Plutonium

Any investigation of plutonium involves more hazards than comparable studies on the typical non-radioactive elements. Challenges involving human exposure, environmental release, and security issues make the study of plutonium difficult. Despite all of these vicissitudes, using microgram quantities and a special experimental set-up, Veal [18] first reported the binding energies of the prominent core levels of plutonium oxide via x-ray photoelectron spectroscopy (XPS). Because of the small amount of material involved in the experiments, the oxidation state of the metal was not measured independently, but assumed to be the dioxide from the preparation. Larson [19] successfully prepared a clean plutonium metal surface and performed oxygen gas reaction studies via XPS and AES. These experiments showed that the oxidation of plutonium occurs in two stages. The first is a rapid reaction to a “suboxide”, a term used in the paper to describe an oxide where the plutonium is not in the oxidation state of 4+, as shown by the Pu 4f photoelectron signal. The second stage of the oxidation is a steadily decreasing conversion from the “suboxide” to plutonium dioxide. The different oxides were determined from changes in the XPS Pu 4f core level after exposure to

oxygen. This two stage oxidation mechanism was confirmed with high resolution photoelectron spectroscopy (PES) performed at -196^{o} C [20]. In a more detailed study of plutonium metal and its oxides, Courteix [21] prepared plutonium metal thin films which were exposed to air and analyzed by X-ray diffraction (XRD) to confirm the PuO_2 composition as well as XPS analysis to determine the Pu 4f core level binding energy for Pu^{4+}, as in PuO_2. This work confirmed the existence of a "suboxide", as reported by Larson [19], not only as the product of the oxidation of a clean Pu metal surface, but also observed after ion bombardment of a PuO_2 thin film with Ar^{+} which is expected to result in reduction through preferential removal of the lattice oxygen. Courtiex assigned the formula ~Pu_2O_3 to the suboxide formed, based on the binding energy shift of the Pu 4f photoelectron signal as a function of Pu oxidation state. A short time after this study, the same group published the binding energies for photoelectrons of a clean Pu metal surface [22].

While plutonium oxide films on metal surfaces were characterized by XPS, there was still no knowledge of how the plutonium binding energy relates to actual oxidation of the metal or the effect of different oxidizing conditions on the composition of the thin plutonium oxide film. To that end, Courtiex [23] monitored the oxidation of a Pu metal surface with XPS to determine the effect of the oxidizing gas (oxygen and water vapor) on the surface. As described in earlier reports [19, 21], upon exposure to oxygen gas, the plutonium surface initially converted to a suboxide (Pu_2O_3) followed by a slow conversion to the dioxide (PuO_2) after several hours of oxygen exposure. When the same experiment was performed with water vapor as the oxidizing gas, the metal surface

quickly oxidized to Pu_2O_3. The dioxide (PuO_2) was not observed. It was hypothesized that oxidation by water vapor occurs via a radical hydroxyl mechanism. These findings, while not conclusive, supported the gravimetric oxidation experiments performed in the past which showed oxidation of plutonium occurring 100 times faster with water vapor (measured as sample weight gain) as opposed to oxidation with oxygen gas.

In addition to probing the typical products of the oxidation process of the metal surface, XPS has also been employed to probe other plutonium compounds, and how their surfaces change as a function of preparation or conditions. Native oxides grown in air have been analyzed to determine the type of species formed [24]. PuO_2 exposed to water vapor showed evidence of Pu species of higher valence with the formula PuO_{2+x} indicating the formation of hydroxyls at the surface. Another compound, PuO_2CO_3, was found to be predominantly Pu^{6+} which over time decomposed to Pu^{4+}. Several alloys of Pu, such as PuSe and $PuSi_2$ have been studied in an effort to determine the effect of 5f valence electron on screening of the 4f core electron [25]. Plutonium carbides of varying compositions (PuC_{1-x}) have also been prepared and studied for this purpose [26]. The corrosion of Pu metal by carbon monoxide (CO) was investigated [27] and found to result in the formation of oxide, carbide, and graphitic carbon. An interesting behavior of plutonium oxide films, the auto-reduction of plutonium dioxide (PuO_2) to plutonium sesquioxide (Pu_2O_3) under a reducing (UHV) environment, was described and utilized [28] to calculate the diffusion coefficient of oxygen through a plutonium dioxide film. This process will be described in more detail in a following chapter.

1.5 Surface Oxidation of Plutonium

The preceding sections presented an overview of the current state of knowledge of the oxidation of plutonium metal as well as a summary of some surface science investigations dealing with plutonium. After all this work, the oxidation of plutonium is still poorly understood, particularly during the early stages. Yet, this knowledge is of importance if the elucidation of the oxidation kinetics of plutonium metal is to be achieved. Corrosion is an important factor that must be accounted for during the processing of plutonium metal into useful components. Plutonium has been known to "spontaneously combust" [29] in glove boxes where metal machining operations take place. Safe environmental parameters to ensure the stability of plutonium metal during storage and waste disposal as well as safeguarding the reliability, safety, and surveillance of nuclear weapons are also areas that can be improved with better understanding of the oxidation of plutonium.

This dissertation aims to improve the understanding of the oxidation characteristics of plutonium. To that end, surface science techniques, particularly XPS and Auger electron spectroscopy (AES), are employed to probe the metal surface and the oxides that develop on it during exposure to oxygen. The work is divided into four main sections. The first deals with very thin oxide films that form during the initial stages of oxidation at low pressures. The second part is an investigation of the auto-reduction of PuO_2. The investigation of the stoichiometry and stability of plutonium oxide films will be addressed in the third part. The effects of impurities, both introduced and those intrinsic to plutonium metal are addressed in the final section.

References

[1] Michaudon, A. F. and Buican, I. G., *Los Alamos Science*, **26** (2000) 4.

[2] Hammel, E. F., *Plutonium Metallurgy at Los Alamos: 1943-1945*, Los Alamos Historical Society, 2000.

[3] *Atomic Power in Space: A History*, DOE Report # NE 32117 H1, 1987.

[4] Katahara, E., *The Nonproliferation Review*, Fall 1997, 53.

[5] U.S. Public Law 109-58, 109th Congress: Nuclear Policy Act of 2005.

[6] Sarrao, J. L., Morales, L. A., Thompson, J. D., Scott, B. L., Stewart, G. R., Wastin, F., Rebizant, J., Boulet, P., Colineau, E., Lander, G. H., *Nature*, **420** (2002) 297.

[7] Los Alamos National Laboratory Report # LALP-06-072, April 2006.

[8] Hecker, S. S., Harbur, D. R., Zocco, T. G., *Progress in Materials Science*, **49** (2004) 429.

[9] Wick, O. J., Plutonium Handbook- A Guide to the Technology, Vol. I & II, (American Nuclear Society:1980), p. 33.

[10] Hecker, S. S., Timofeeva, L. F., *Los Alamos Science*, **26** (2000) 244.

[11] Hecker, S. S., *Los Alamos Science*, **26** (2000) 36.

[12] Colmenares, C. A., *Prog. Solid St. Chem.*, **9** (1975) 139.

[13] Hasckhe, J. M., Allen, T. H., Stakebake, J. L., *J. Alloys Comp.*, **243** (1996) 23.

[14] Stakebake, J. L., Larson, D. T., Haschke, J. M., *J. Alloys Comp.*, **202** (1993) 251.

[15] Colmenares, C. A., *Prog. Solid St. Chem.*, **15** (1984) 257.

[16] Raynor, J. B., Sackman, J. F., *Nature,* **197** (1963) 587.

[17] Plutonium 1965: Proceedings of 3rd International Conference on Plutonium, London, Kay, A. E. & Waldron, M. B., eds. (*Institute of Metals*, Chapman & Hall:1965)

[18] Veal, B. W., Lam, D. J., Diamond, H., Hoekstra, H. R., *Phys. Rev. B*, **15** (1977) 2929.

[19] Larson, D. T., *J. Vac. Sci. Technol.*, **17** (1980) 55.

[20] Butterfield, M., Durakiewicz, T., Guziewicz, E., Joyce, J. J., Moore, D. P., Arko, A. J., Morales, L. A., *Mat. Res. Soc. Proc.*, **802** (2004) 81.

[21] Courteix, D., Chayrouse, J., Heintz, L., Baptist, R., *Solid State Comm.*, **39** (1981) 209.

[22] Baptist, R., Courteix, D., Chayrouse, J., Heintz, L., *J. Phys. F:Met. Phys.*, **12** (1982) 2103.

[23] Courteix, D., Fontaine, J. M., Lozes, G., CEA-CONF 8863, *Seminar on Surface Analysis*, Oct 1986.

[24] Farr, J. D., Schulze, R. K., Neu, M. P., *J. Nucl. Mater.*, **328** (2004) 124.

[25] Gouder, T., Havela, L., *J. Alloy. Compd.*, **444-445** (2007) 149.

[26] Gouder, T., Havela, L., Shick, A. B., Huber, F., Wastin, F., Rebizant, J., *J. Phys.: Condens. Matter*, **19** (2007) 476201.

[27] Tull S., 2003 *Ph.D.* Thesis, University of Wales, Cadiff, U.K.

[28] Morrall, P., Tull, S., Glascott, J., Roussel, P., *J. Alloy. Compd.*, **444-445** (2007) 352.

[29] Haschke, J. M., Allen, T. H., Morales, L. A., *Los Alamos Science*, **26** (2000) 252.

Chapter 2: Experimental Section

Corrosion is defined by the International Union of Pure and Applied Chemistry (IUPAC) as an irreversible interfacial reaction of a material with its environment which results in consumption of the material or dissolution into the material of a component of the environment [1]. During the oxidation of plutonium metal, oxygen diffuses through the metal-gas interface forming an oxide film on the surface. Since the surface is the starting point and the gateway through which oxidation occurs, an ideal experimental technique to investigate this process is one which has enhanced surface sensitivity.

2.1 Electron Spectroscopy

One of the most appealing characteristics of electron spectroscopy is its sensitivity to the surface of a material. As an electron is emitted from the material, collisions attenuate the energy intensity of escaping electrons.

$$I_S = I_O e^{-d/\lambda}$$

Where I_O is the intensity of the electron emitted at a depth d, I_S is the intensity of the electron as it reaches the surface, and λ is the inelastic mean free path (IMFP). Within a path length λ, 63% of all electrons are scattered. The sampling depth is generally defined as the depth from with 95% of all electrons emitted are scattered by the time they reach the surface (3λ). The IMFP of an electron is proportional to the kinetic energy of the electron.

2.2 X-ray Photoelectron Spectroscopy

Electron spectroscopy for chemical analysis (ESCA), also referred as x-ray photoelectron spectroscopy (XPS), involves the irradiation of a surface with soft x-rays and analysis of the kinetic energy of the emitted photoelectrons, as illustrated in Figure 2.1. The photoemission process can be divided into three steps: (1) photon absorption and

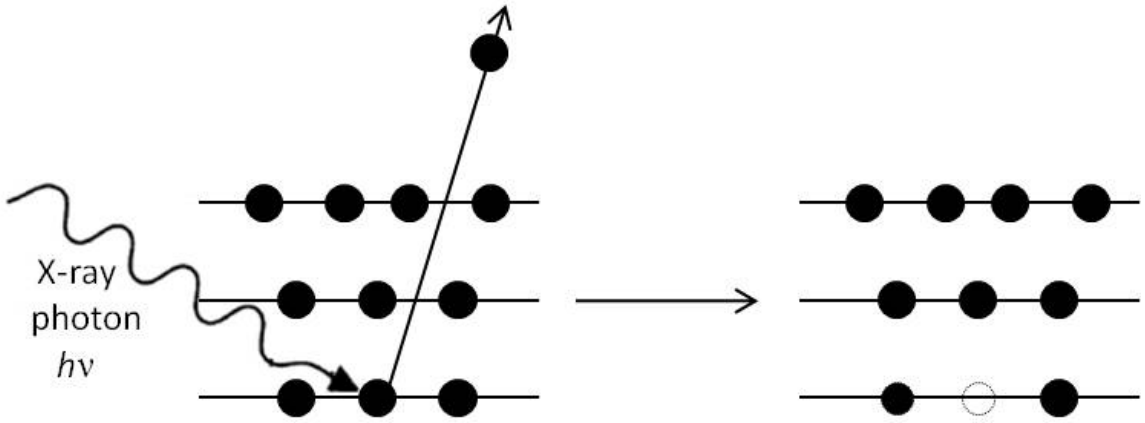

Figure 2.1: Conceptual illustration of the electron photoemission process.

ionization (initial state effects), (2) relaxation of the atom and creation of the photoelectron (final state effects) and (3) the transport of the ejected electron to the surface (extrinsic effects). The energy of the ejected photoelectron is directly related to the atom, from which it emerges,

$$BE = h\nu - KE - \phi$$

where $h\nu$ is the energy of the photon (x-ray), *KE* is the kinetic energy of the ejected photoelectron, ϕ is the combined spectrometer and sample work function and *BE* is the binding energy of the electron. Not only is elemental identification possible, but the

chemical state of the element can also be probed via XPS due to the sensitivity of the ejected electron to the nearest atoms. Interpretation of the binding energies of core electrons in an XP spectra of became feasible with the formulation of Koopmans' theorem [2], which equates the negative of the biding energy (BE) defined above to the energy of the core electron in the XPS experiment. While useful, the theorem assumes that there is no interaction between the ejected electron and the changing element in the solid as the remaining electrons shift to shield the charged atom. The neglected atomic orbital relaxation may cause underestimation of the calculated initial state energy of the electron in the solid from the values measured. Nevertheless, the calculated binding energies are generally qualitatively correct, for the given element. The width of the XPS signal peak, full-width at half the maximum peak height (FWHM), is a function of several factors including the linewidth of the x-ray source, the resolution of the electron analyzer, and the natural line width of the transition. Core level transitions with a half-life of 10^{-15} to 10^{-19} second yield line widths of between 0.05 and 4 eV [3].

An XP spectrum is characterized by peaks with a rising background to the higher binding energy side of each set of peaks. The step-like pattern of the rising background is caused by inelastically scattered photoelectrons. The height of the step can be utilized to extract information on the depth of the atom from which the photoelectron emanated [4, 5]. Photoelectrons from atoms near the surface will exhibit a small background. Photoelectrons from atoms near the surface will exhibit a small background rise while those from atoms deeper beneath the surface show a steep rise in the background which

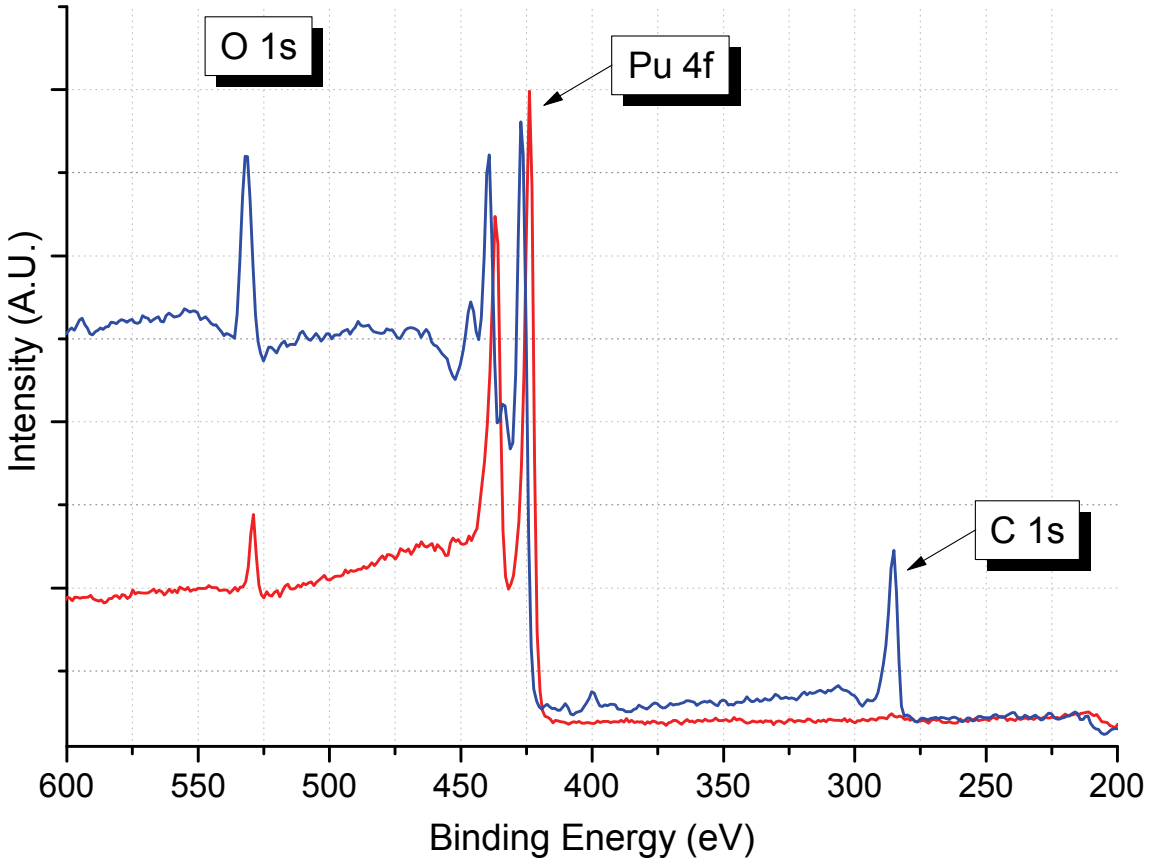

Figure 2.2: XP spectra illustrating the effect of an adsorbed layer on a plutonium oxide surface. The oxide surface with a carbon adlayer (blue trace) exhibits a steep rise in background in the high binding energy side of the Pu 4f photoelectron signals. Following a brief ion sputtering cleaning of the surface (red trace), the carbon 1s signal disappears and the background step of the Pu 4f signal decreases.

may even swamp the main photoelectron peak. Surface contamination on a surface,may even swamp the main photoelectron peak. Surface contamination on a surface, typically from residual gases within the vacuum chamber, causes attenuation of the underlying metal photoelectron resulting in a steep increase of the inelastically scattered electrons background signal in the spectrum, as shown in Figure 2.2.

The structural features of core level photoelectron signals observed in an XP spectrum can be attributed to several factors. Core photoelectrons from levels other than *s* ($l > 0$), are doublets. The separation between the two peaks is due to the coupling (quantum number, *j*) of the spin (quantum number, *s*) and the orbital angular momentum (quantum number, *l*) of the photoejected core electron. The relative intensity of the doublet is determined by the degeneracy *2j+1*. Table 2.1 tabulates the relationship between these quantum properties of the core electron.

A core level photoelectron is especially sensitive to the chemical environment of the element in the solid. This environmental dependence, illustrated in Figure 2.3, is one

Table 2.1: X-ray photoelectron spectroscopy *l-s* coupling for core electron signals.

Quantum number			*Degeneracy* $2j + 1$	*Spectroscopic Level*
n	*l*	$j = l \pm s$		
1 2 3 4	0	0	1	1s 2s 3s 4s
2 3 4	1	1/2 , 3/2	1:2	$2p_{1/2}$, $2p_{3/2}$ $3p_{1/2}$, $3p_{3/2}$ $4p_{1/2}$, $4p_{3/2}$
3 4	2	3/2, 5/2	2:3	$3d_{3/2}$, $3d_{5/2}$ $4d_{3/2}$, $4d_{5/2}$
4	3	5/2, 7/2	3:4	$4f_{5/2}$, $4f_{7/2}$

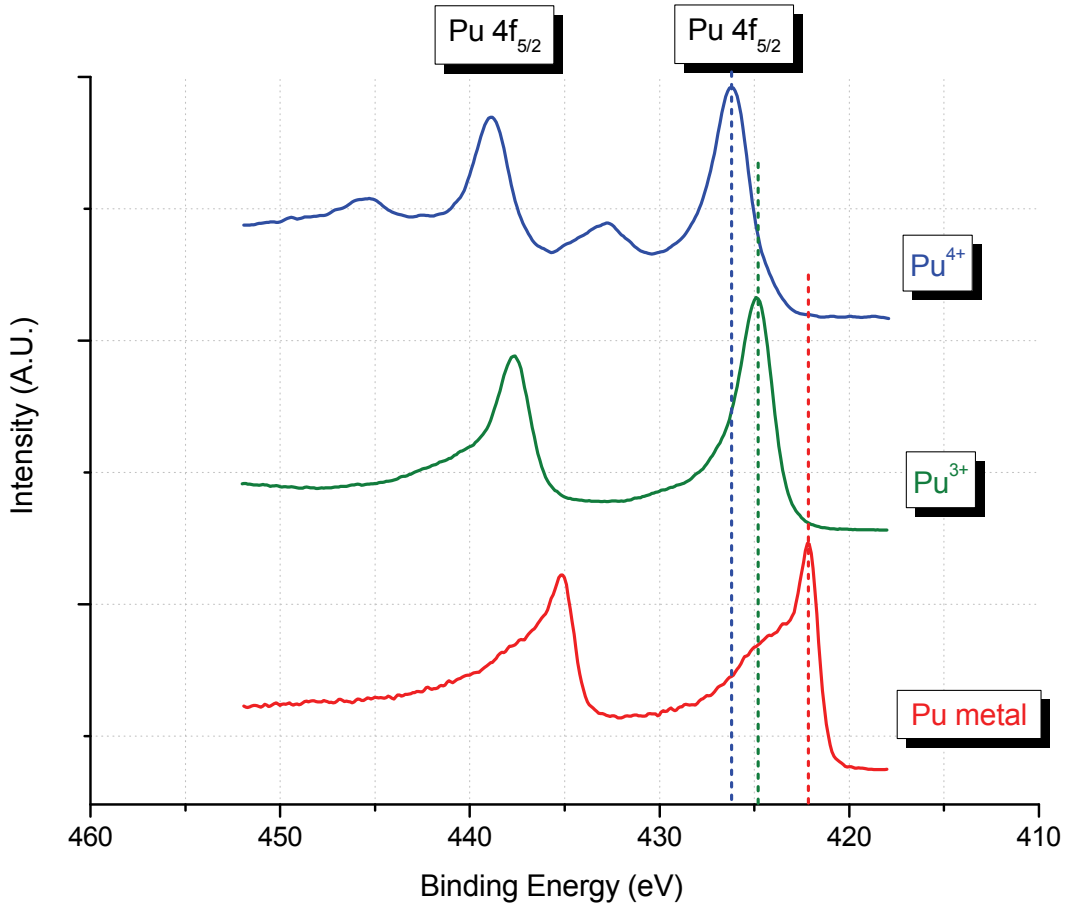

Figure 2.3: Chemical shift of the plutonium 4f photoelectron signal as a function of oxidation state. Plutonium metal (red), Pu^{3+} (green), and Pu^{4+} (blue) signal shifts toward higher binding energy with increasing formal charge. In addition to displaying the highest binding energy of the three species, Pu^{4+} exhibits a set of 'shake-up' satellites.

of the more appealing and powerful features of x-ray photoelectron spectroscopy. The chemical shift of the binding energy can be correlated to the overall charge of the atom, number of substituents, the electronegativity of substituents, and the formal oxidation state of the atom. That last property of the atom may not be a reliable predictive factor in chemical shift depending on the ionic/covalent character of the bond [3]. Thus, the spin orbital splitting, the peak area ratio, and the binding energy value of a signal in a XP

spectrum assist in elemental identification and chemical environment of the atoms at the surface.

Secondary structure is often observed along with core level photoelectron signal in an XP spectrum. Multiplet splitting arises from the interaction of unpaired electrons in the valence levels with the core level photoelectron. The multiplet splitting is strongest when the electrons involved are in the same shell (i.e., 3p-3d, 4d-4f) but is also observed for interactions of unpaired electrons of different shells. When the core level unpaired electron has a spin parallel to the valence electrons, electrostatic interactions can occur which will manifest as lower binding energy peak than when the core level unpaired electron has anti-parallel spin relative to the valence electron. The energy different is small; consequently the main effect of the multiplet splitting is the broadening of the XPS peak resulting in asymmetry. Another common feature of the photoelectron spectrum is occurrence of the "shake-up" satellites. The creation of a core electron hole via photoelectron emission causes a major perturbation in an atom. The effect is an increase in the effective nuclear charge experienced by the valence electrons. The excitation of one (or more) of these electrons to a higher unoccupied level may be a result of the reorganization of the valence electrons. The energy required for this transition accounts for an additional peak observed at higher binding energy (lower kinetic energy) side of the main photoelectron peak. An example of multiple shake-up satellites can be seen in Figure 2.4. In a similar manner to 'shake-up' satellites, a valence electron can be ejected from the atom, resulting in a doubly ionized atom with a core level and a valence level vacancy. This 'shake-off' satellite typically occurs at a significantly lower kinetic energy

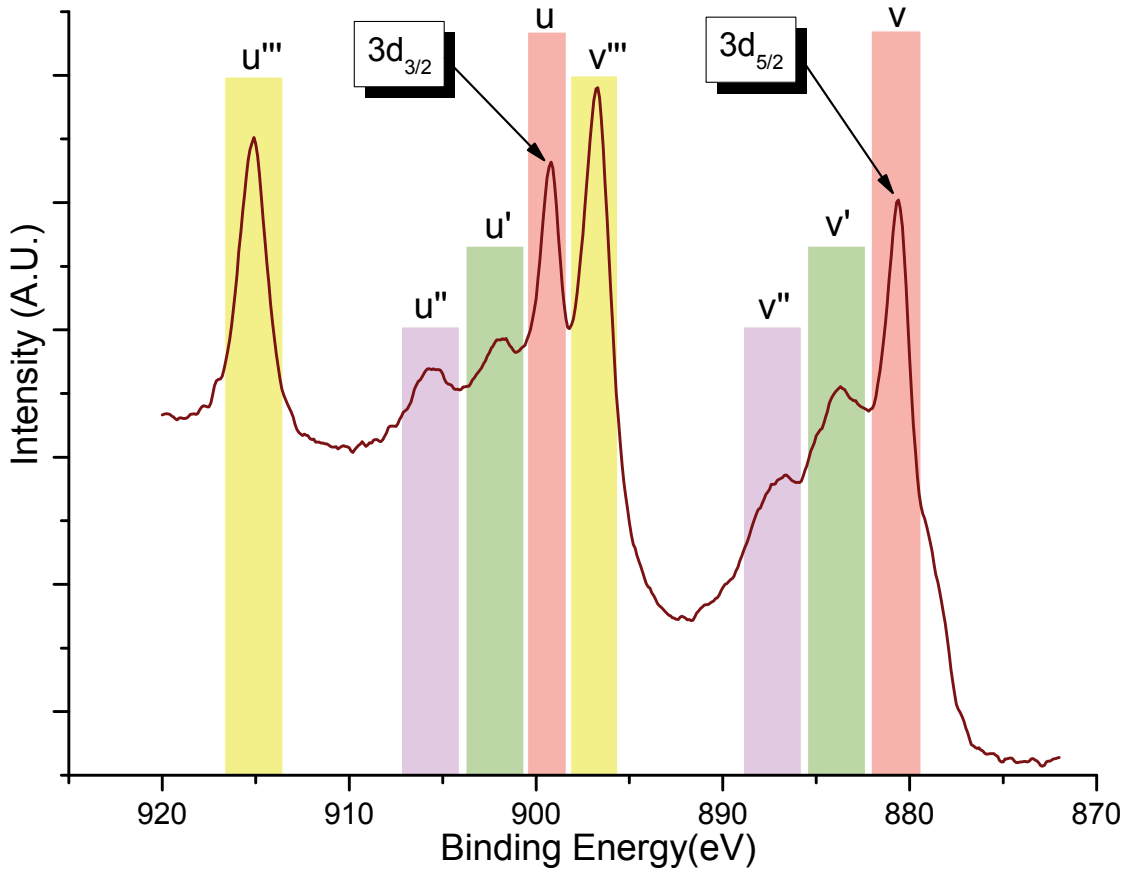

Figure 2.4: The 3d XP spectrum of cerium oxide (CeO_2) represents a striking example of shake-up satellites. The $3d_{5/2}$ and $3d_{3/2}$ doublets are labeled v & u, respectively (in red). The three pairs of primed peaks represent the three sets of shake-up satellites. The biding energy difference between the core photoelectrons (v & u) is the spin-orbit spitting. Notation of peaks follows previously assigned convention [7].

from the photoelectron peak than the 'shake-up' satellites and is not easily discernible from the inelastic scattering background of the photoelectron signal.

A fourth type of XP spectra structure is the result of interactions between the ejected photoelectron and the collective oscillation modes of electrons in the conduction band of the metal. Similar to shake-up and shake off satellites, these plasmon loss features are found at higher binding energies (lower electron kinetic energy) than the

main photoelectron peak. The energy difference is equal to the excitation energy of the plasmon. Both bulk and surface plasmon may be detected [6].

The core level hole created by the ejected photoelectron is an excited and unstable system. There are two mechanisms by which the core hole can be neutralized. In the first, an electron from a higher level drops down and releases its excess energy in the form of a photon. This process is the basis for x-ray fluorescence spectroscopy [8]. In the

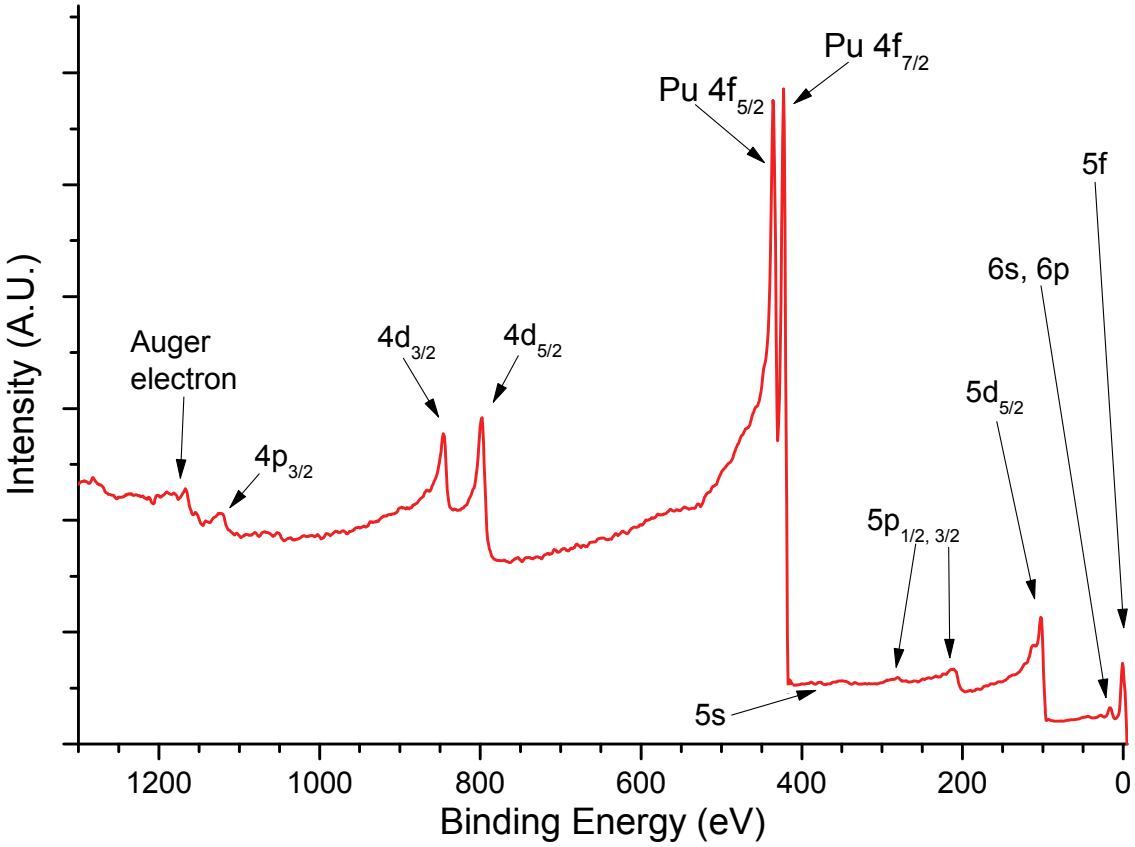

Figure 2.5: XP spectrum of a clean plutonium metal surface showing the photoelectrons emitted as well as the Auger electron transitions.

second, the excess energy, released by an electron to occupy the original core level hole, may instead be transferred to another electron, which is then ejected from the atom. The ejected electron is referred to as the Auger electron, after Pierre Auger who first described the process [9, 10]. A series of peaks at a binding energy of ~1185 eV in the XP spectrum of plutonium metal, shown in Figure 2.5, is due to the Auger electrons emitted during the relaxation of the core hole [11]. The probability of either event occurring is a function of the atomic number (Z) of the atom. Auger electron emission is favored for elements with low Z (less than 33) while x-ray fluorescence has a higher probability for elements with Z greater than 33. Electron core hole relaxation of a plutonium atom, with $Z = 94$, occurs predominantly via x-ray fluorescence thus, the weak Auger electron signal observed in Figure 2.5.

The photoelectrons that are detected via XPS analysis can be seen in the XP spectrum in Figure 2.5. A cursory glance at the spectrum shows why the 4f photoelectron is the signal of choice when analyzing plutonium with XPS: its large cross-section yields the largest peaks facilitating analysis at low concentrations and minimizing data acquisition times. An overview of positions for the characteristic plutonium lines in the spectrum shown in Figure 2.5 is shown in Table 2.2. The Al Kα x-rays (1486.6 eV) only has enough energy to probe the core levels of plutonium up to 4p level.

Table 2.2: Plutonium binding energies for the various photoelectron lines that are detected with XPS using Al Kα radiation. The most intense lines used for analysis throughout this thesis (Pu 4f) are shown in bold type. The $4p_{1/2}$ is not determined as it interferes with the Auger transition (NOV) at ~1185 eV (noted in Figure 2.5) [11].

Photoelecton Level	Binding Energy (eV)	Photoelecton Level	Binding Energy (eV)
$4p_{1/2}$	N/A	$5p_{1/2}$	284.2
$4p_{3/2}$	1122.6	$5p_{3/2}$	211.1
$4d_{3/2}$	844.8	$5d_{3/2}$	113.7
$4d_{5/2}$	798.1	$5d_{5/2}$	101.3
$4f_{5/2}$	**435.1**	6s	~49
$4f_{7/2}$	**422.1**	$6p_{1/2}$	~30.6
5s	366	$6p_{3/2}$	~17.2

2.3 Angle Dependent XPS

Earlier in this chapter, it was discussed how the surface sensitivity of the XPS technique is an inherent characteristic, and advantage, of the technique due to the small inelastic mean free path (IMFP or λ) of the ejected photoelectron through the sample. By varying the angle θ, between the sample surface and the analyzer, as illustrated in Figure 2.6, the surface sensitivity of the technique can be enhanced. At large angles, the photoelectrons signal in the XP spectrum is generated at the outer-most atomic layer of the surface or very near the surface. The equation for the intensity of the ejected

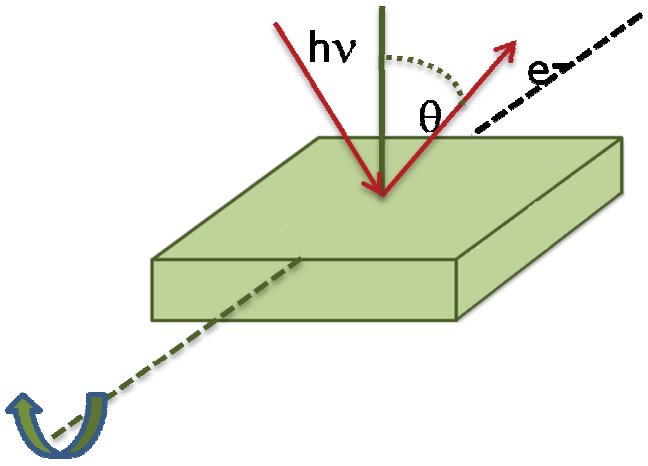

Figure 2.6: Schematic diagram for angle dependent XPS experiment.

photoelectron can be re-written as:

$$I_S = I_O e^{-d/\lambda * \cos\theta}$$

to account for the angle of analysis, θ,where I_o is the intensity of the electron emitted at a depth d, I_S is the intensity of the electron as it reaches the surface, and λ is the inelastic mean free path (IMFP). Angle-resolved XPS has been used to determine the thickness of oxide layers on metallic substrates [12-14] and metallic layers deposited on different metallic substrates [15-17]. This technique will be employed, as part of this thesis, to confirm the layered oxide model of the plutonium oxide films prepared.

2.4 Auger Electron Spectroscopy

The Auger process, illustrated in Figure 2.7 and described in the previous section as one of the relaxation mechanisms for the core level hole created during XPS analysis, forms the basis for Auger electron spectroscopy (AES). In this technique, rather than

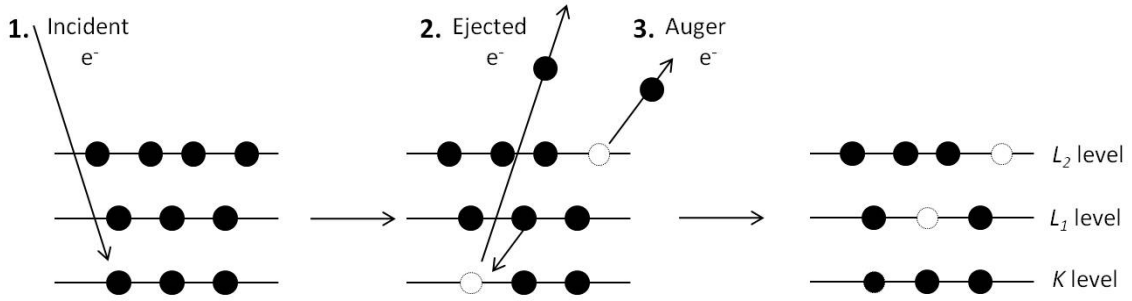

Figure 2.7: Conceptual diagram of the Auger electron emission process after the creation of the core hole via electron ionization. Because of the number of electrons involved, the Auger process is described as a three electron process.

utilizing a photon to create the core hole in the atom, the sample is bombarded with an electron beam of energies at least five times the core level energy. In the diagram shown in Figure 2.7, the incident electron beam excites a core electron at the *K* level which is consequently ejected from the atom. An electron at a higher core level (L_1 level) drops to fill the initial core hole transferring the excess energy to a third electron at the L_2 level , the Auger electron, which is ejected creating a doubly-ionized atom. The kinetic energy of the Auger electron is independent of the energy of the electron beam used to create the initial core hole formation and can be written as

$$E_{Auger} = E_K - \left(E_{L_1} - E_{L_2}\right)$$

where E_K is the energy of the *K* level, E_{L1} is the energy of the L_1 level electron, E_{L2} is the energy of the L_2 level, and E_{Auger} is the energy of the Auger electron. For the three electronic levels in Figure 2.7, there are several possible Auger transitions:

$$KL_1L_1 \vdots KL_1L_2 \vdots KL_2L_2$$

thus, there may be several transitions of varying intensity observed for a given element. For plutonium in particular, with 94 electrons, the number of possible permutations is staggering. The most intense Auger transitions for plutonium metal are listed in Table 2.3; the differentiated Auger transition energies are listed in Table 2.4.

In an Auger electron (AE) spectrum, the signals are situated on a steeply-sloping background of inelastic scattered electrons, as can be observed in Figure 2.8. The Auger transition for carbon and oxygen appear at 501 eV and 275 eV, respectively. In order to resolve the Auger peaks from the inelastic background and to increase the accuracy of quantification, Auger spectra are often differentiated, as shown in Figure 2.9**.** The *PVV* Auger transition yields the most intense signal of all the transitions thus, is might seem like an ideal candidate to be utilized for quantification. However, Auger signals at low kinetic energy of the spectrum are susceptible to drastic changes that are not solely due to the quantity of the element. For instance, chemical changes at the surface, as is the case in the oxidation of a metal, cause changes in the work function of the surface and in the valence band. These changes are manifested in the low kinetic energy region of the AE spectrum and can significantly decrease the accuracy of quantification. In fact, attempts to develop a reliable sensitivity factor for quantification of Pu utilizing the *PVV* transition were unsuccessful. The *NOV* transition, while less than a third as intense as the *PVV* transition, yielded consistent and accurate quantifications of Pu. Thus, the signal at 317 eV has been chosen as the quantification transition for plutonium in this investigation.

Table 2.3: Kinetic energies of the Auger electron transitions for plutonium metal. These ten transitions are the most intense, although many more are possible due to the large number (94) of electrons. The values agree well with those previously published [18].

Auger Transition	Kinetic Energy (eV)	Auger Transition	Kinetic Energy (eV)
$P_1 VV$ $O_4 P_3 V$	78	***$N_7 O_5 V$*** ***$N_6 O_4 V$***	**313.5**
$O_4 VV$	96	$N_6 O_5 V$	326
$O_5 VV$	101.5	$N_6 P_2 V$	400.5
$O_3 VV$	209	$N_7 P_3 V$	416.5
$N_7 O_4 V$	298	$N_7 VV$	428.5

Table 2.4: Kinetic energies of the differentiated Auger electron transitions for plutonium metal. The Auger transition line used for analysis throughout this thesis is shown in bold type.

Auger Transition	Kinetic Energy (eV)	Auger Transition	Kinetic Energy (eV)
$P_1 VV$ $O_4 P_3 V$	80.5	***$N_7 O_5 V$*** ***$N_6 O_4 V$***	**317**
$O_4 VV$	98.5	$N_6 O_5 V$	329
$O_5 VV$	103	$N_6 P_2 V$	403
$O_3 VV$	214	$N_7 P_3 V$	418.5
$N_7 O_4 V$	300	$N_7 VV$	431.5

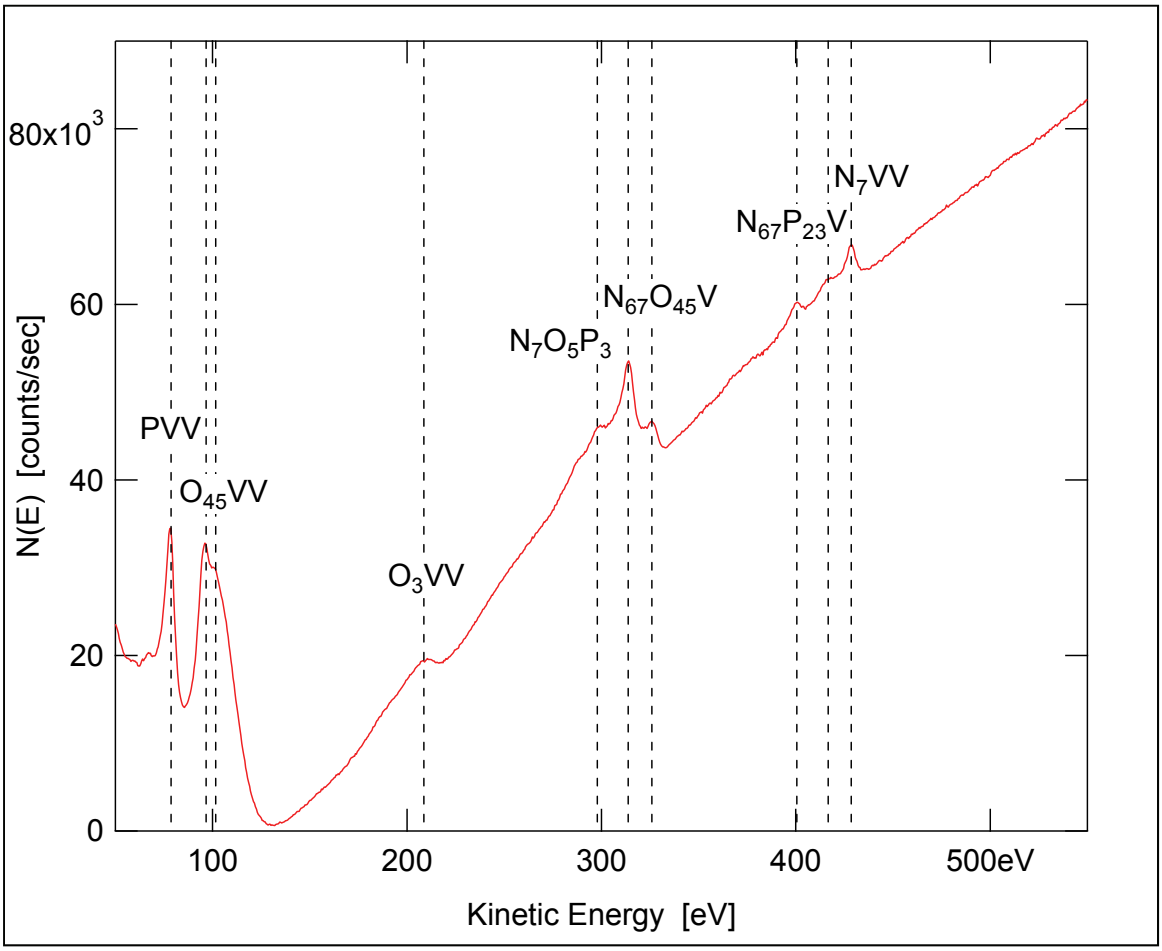

Figure 2.8: Auger electron (AE) spectrum of a clean plutonium metal sample. The dash lines mark the position of the AE transitions. An overview of the main transitions is in Table 2.3 [19].

A main disadvantage of AES for studying oxide layers of plutonium is its low sensitivity. As mentioned previously, because of its high atomic number, x-ray fluorescence is favored over the Auger process, resulting in a low sensitivity factor. Additionally, AES is not particularly effective at probing the chemical state of atoms; it is not able to differentiate between the oxidation states of plutonium, although it can discern the Pu metal atom from oxidized Pu, since the two species have Auger kinetic energies of

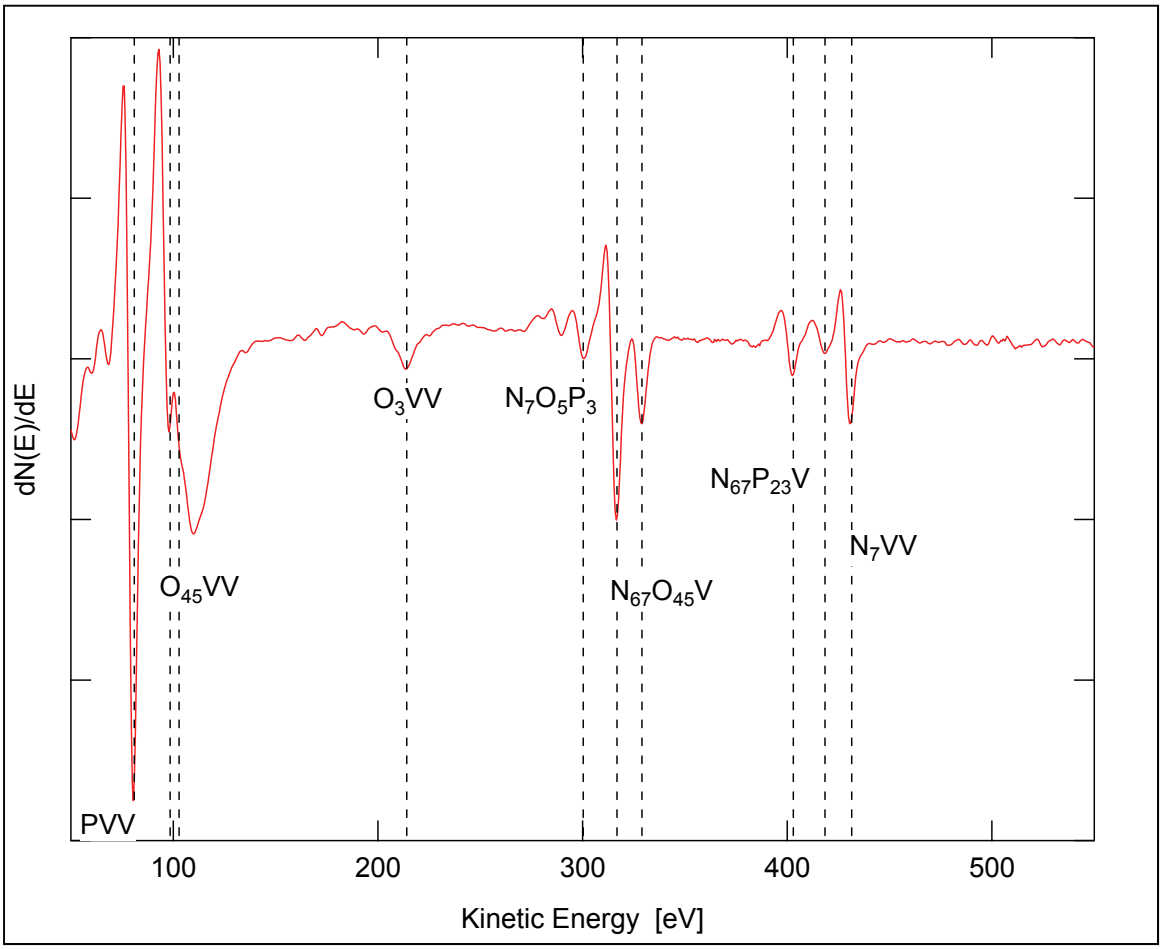

Figure 2.9: Differentiated Auger electron (AE) spectrum of a clean plutonium metal sample. The dash lines mark the position of the AE transitions. An overview of the main transitions is Table 2.4 [19].

slightly different values. Nevertheless, it can be useful for the detection of impurities, as the relative sensitivity factors of carbon, oxygen, and gallium to Pu are larger than in XPS. Because of the design of the instrument, AES data can be acquired while the sample is being exposed to oxygen, allowing the investigation of the evolution of the oxide film as it is being formed. This is only possible with XPS for very low pressures (less than $5*10^{-8}$ Torr) as the x-ray generator cannot be operated at higher pressures. The

field emission gun used to initiate the Auger process forms a sharply focused electron beam which allows the acquisition of electron micrographs of the metal surface and AES analysis of very small areas of the sample, approximately 300 nm^2.

2.5 Instrumentation

A critical requirement for performing any electron spectroscopy experiment is a good ultra high vacuum (UHV) normally defined as a vacuum with a pressure of 10^{-9} Torr or lower [12]. Both the XPS and AES instruments utilized for acquiring the data in this thesis exhibit a base pressure of less than $5*10^{-10}$ Torr. The low pressures are attained will a combination of turbomolecular, ion, and titanium sublimator pumps.

The Kratos XPS is installed in a Category I nuclear facility in Los Alamos, NM and thus its installation and operation must comply with the safety and security operational requirements associated with the handling of nuclear materials. Many instrument modifications had to be performed before authorization to introduce plutonium into the instrument was issued. As a defense against the risk of instrument damage from seismistic activity, the UHV chamber and components were securely attached to the laboratory floor with ½ inch steel brackets and steel bolts that were drilled to the floor. A back-up power supply was installed to prevent disruption of instrument operation and to allow the safe and orderly shutdown of the instrument in the event of an extended power outage.

Modifications were also performed in all the input and output outlets of the system to prevent the accidental release of nuclear material into the laboratory and environment. The exhaust lines of all the pumps attached to the system are equipped with HEPA filters which in turn are connected to the controlled air circulation system of the radiological facility. As a backup system to these HEPA filters, a pneumatically-powered gate valve with a custom-made circuitry which automatically closes the valve in the event of a power failure was installed between the UHV chamber and the main turbo molecular pump. In the event of failure of the pumps' HEPA filters, the gate valve prevents the evacuated chamber (P $\sim 10^{-10}$ Torr) from suctioning the air in the facility's controlled air circulation system into the system. The leak valves employed for introducing gases into the analysis chamber during experiments are equipped with in-line filters that prevent the movement of radioactive material into the gas manifolds. Additionally, all the stainless steel lines that connect the XPS system to gas cylinders were welded instead of using Swagelok® [20] connectors and also equipped with redundant double gas regulators in order to decrease the risk of catastrophic gas regulator failure. Such an event can, potentially positively pressurize the UHV chamber causing a breach of containment as the excessive pressure damages the glass viewports releasing radioactive material into the laboratory. These instrument hardware improvements do not affect the analytical performance of the instrument, however they present challenges as far as instrument maintenance is concern.

Sample handling and mounting protocols must also be adapted to maintain compliance with the safety regulations. The Kratos Axis Ultra XPS is supplied from

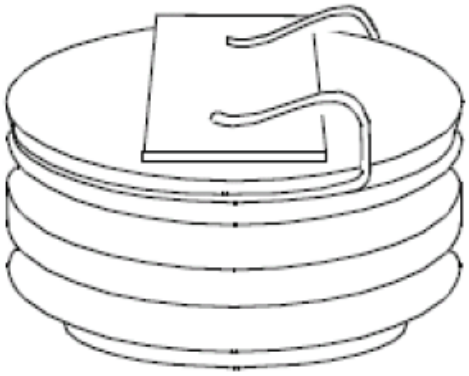

Figure 2.10: Standard sample stub with spring clip supplied by Kratos Analytical [21].

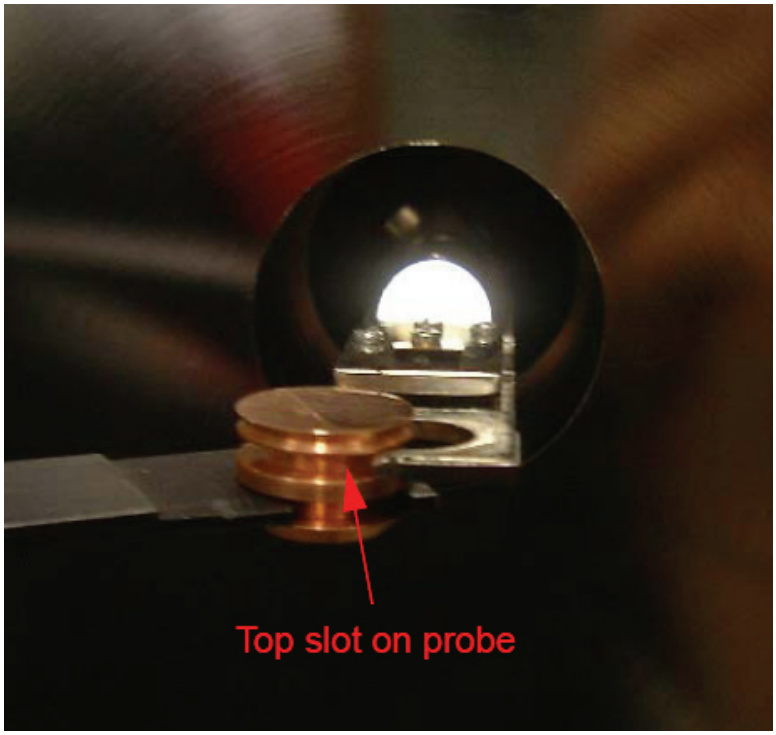

Figure 2.11: Introduction of sample stub into the instrument loading dock with the loading tool (black rod to the left of picture) [21].

factory with a standard 15 mm diameter sample stubs made of copper or stainless steel. The sample is attached to the stub with a spring clip that holds it in place, as illustrated in Figure 2.10. The picture in Figure 2.11 illustrates how the sample is introduced into the instrument through the loading dock. While this set-up method is versatile and simple, it is not conducive for safe handling of radiological materials. It is not inconceivable to imagine a scenario where the spring clip may dislodged inside the instrument causing the sample to fall to the bottom of the chamber. Even more critical would be the dislodging of the spring clip causing the radiological sample to fall to the floor creating and undesirable situation in the laboratory. To mitigate the situation, the sample stub was

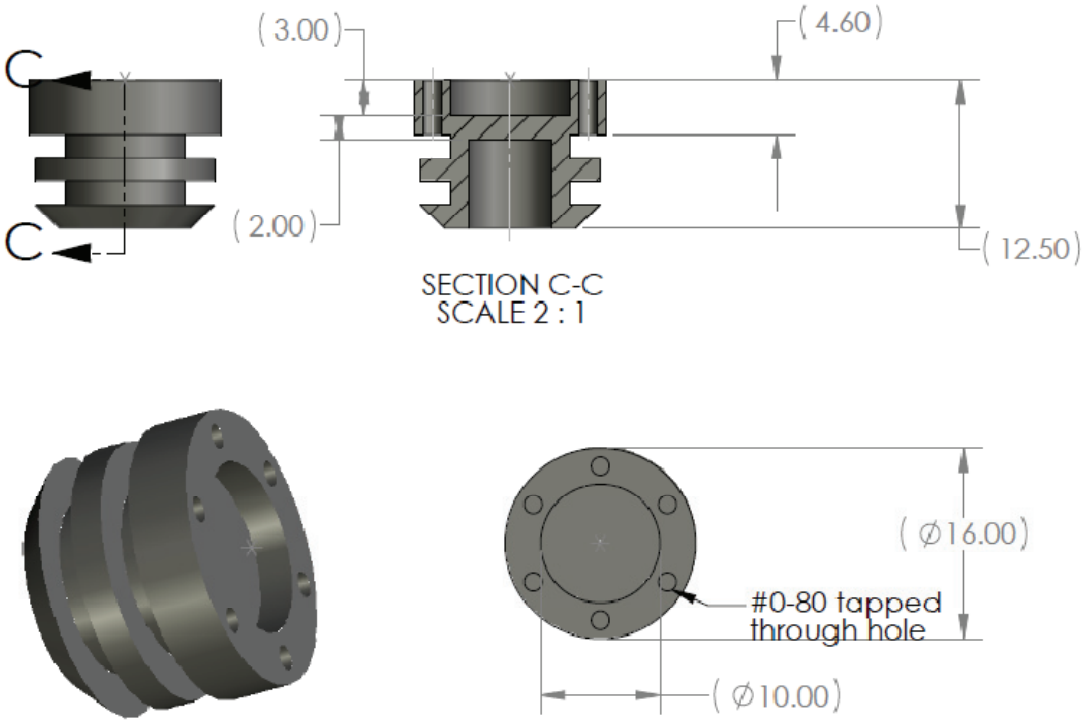

Figure 2.12: Modified sample "cup" holder designed for XPS analysis of nuclear materials in a Kratos Axis Ultra. The tapped holes allow the mounting of a mask to retain the sample firmly in place.

modified to create not only a more infallible manner of attaching the plutonium sample to the stub, but to contain it as much as possible. Figure 2.12 shows a drawing of a sample 'cup' design to contain radiological samples safely. The design, with tapped holes on the lip of the cup, allows the placement of a mask to keep the radiological material firmly in place. The masks, made from tantalum disks, have a centered round hole with a diameter of 5 mm to allow for analysis of the surface while holding the sample in place.

Because of its extreme reactivity toward most elements, an important consideration when working with plutonium is materials compatibility. The sample holders provided with the Kratos XPS are made from 316 stainless steel (316 SS) which has a melting point ~1,400^{o} C. Plutonium and iron, however, are known to form an eutectic compound [22-23]. In a eutectic reaction, a small change in composition could result in a very large change in the melting temperature [24]. In the case of plutonium and iron, the compound Pu_6Fe melts at ~ 400^{o} C. Thus, heating a sample of Pu metal in a sample holder made from 316 SS could potentially result in the Pu_6Fe melting a hole through the bottom of the container when heated to > 400^{o} C. With a desire to avoid that scenario, the sample cup holders used in this investigation were machined from a 16 mm in diameter tantalum metal rod (99.95%) [25]. Tantalum (Ta) is one of the few elements that does not form intermediate solid phases with Pu. The solubility of Pu in Ta is 0.5 at. % at 1,000^{o} C [26]. The favorable compatibility of Ta and its melting point (~3,010^{o} C) make it an ideal material for sample holders. However, Ta is a soft metal not unlike gold, making machining of parts with tight tolerances particularly challenging.

2.5.1 XPS Instrument

The instrument used in the experiments presented here is a Kratos Axis Ultra^{DLD} instrument, shown in Figure 2.13. The vacuum chamber is fabricated from 316 non

Figure 2.13: Kratos Axis Ultra^{DLD} XPS instrument equipped with a hemispherical analyzer, dual Mg/Al x-ray anode, monochromatic Al x-ray anode and ion gun for sputter cleaning. The base pressure is typically less than $5*10^{-10}$ Torr [21].

magnetic stainless steel with all flanges sealed with CF copper gaskets. All materials inside the chamber are UHV compatible allowing achievement of a base pressure of $<5*10^{-10}$ Torr. Achieving a good vacuum ($< 10^{-9}$ Torr) is critical in order to avoid surface reactions or contamination with the background residual gases inside the chamber. At a pressure of 10^{-6} Torr, if every collision between a gas molecule and a surface results in the gas molecule adsorbing to the surface (sticking coefficient of 1) a clean surface will be covered with a monolayer of gas in 1 sec (e.g., 1 Langmuir (L) = 10^{-6} Torr*sec) [27]. At a pressure of 10^{-3} Torr, the surface will be covered with a monolayer of gas in 0.001

seconds. At 10^{-9} Torr, it takes 1000 seconds for the surface coverage to be one monolayer. Thus, at UHV levels, the accumulation of contaminants on a surface is minimal during the course of acquiring spectra. Other advantages of the UHV include: minimized collisions of the electron with gas molecules allowing them to reach the detector, the elimination of adsorption of the soft x-rays by air, and enabling the cleaning of contaminants on the surface with an ion beam, typically argon.

Achieving UHV levels inside the instrument chamber is a time consuming endeavor. Whenever instrument maintenance requires venting the instrument to atmosphere to replace worn components, a common practice is to slowly introduce the nitrogen gas bubbling from a liquid nitrogen container. This practice minimizes the introduction of water vapor into the chamber. Safety regulations at the nuclear facilities in Los Alamos, precludes the use of this technique as a way of preventing the over-pressurization from accidental introduction of liquid nitrogen into the chamber. As an alternative, laboratory air is introduced into the system through a gas manifold equipped with a HEPA filter and a Drierite® Laboratory [28] that removes the water vapor from the air.

The pumping station of the system is not sufficient to bring the vacuum down to UHV by itself. A bake out process is necessary to remove adsorbed gases from the chamber walls and internal components. There are integrated bake-out heaters located between the chamber walls and the outer claddings at various places on the instrument which heat the entire system to ~150^{o} C. The high temperature enables the accelerated

desorption of the gases, mainly water, from the walls inside the chamber. The process generally lasts 36-48 hours. After degassing all the filaments in the instrument, the base pressure inside the chamber is ~$2*10^{-10}$ Torr. During data acquisition, the operating pressure is < $2*10^{-9}$ Torr.

The pressure inside the system is measured via an electron bombardment nude gauge [29] equipped with a thorium coated iridium filament and an Edwards Active Ion Gauge Controller [30]. The working pressure range of this gauge is $3*10^{-11}$ - $5*10^{-3}$ Torr. The pumping system for the XPS includes a BOC Edwards 240 L/s turbo molecular pump backed up with a BOC Edwards XDS-5 dry scroll pump. The main analysis chamber also has a Varian ion pump with a MidiVac controller and titanium sublimation pump (TSP) [31].

The Kratos Ultra XPS is equipped with a dual Al-Mg and an Al monochromatic x-rays source. The dual source provides two different source energies, listed in Table 2.5: the Al Kα line at 1486.6 eV and the Mg Kα line at 1253.6 eV. The Mg line is slightly narrower. The main advantage of having two x-ray sources is the ability to differentiate between photoelectron and Auger peaks in an XP spectrum. Since Auger electrons are independent of *kinetic* energy, the peaks will appear to shift by 233 eV (energy difference of the two sources) in *binding* energy while the photoelectron peaks will remain constant in an XP spectrum. In addition to the main Kα lines, these sources also produce other transition lines referred as x-ray satellites arising from less probable transition. The most

Table 2.5: Energies and widths (FWHM) for the two materials used as x-rays sources in XPS [3].

Source Line	Energy (eV)	FWHM (eV)	FWHM-Monochromatic (eV)
Mg Kα	1253.6	0.7	N/A
Al Kα	1486.6	0.85	< 0.26

Table 2.6: Relative position and intensity of the satellite lines for the Al and Mg x-ray sources [3].

	Mg		Al	
X-ray line	Separation from Kα	Relative Intensity (Kα =100 %)	Separation from Kα	Relative Intensity (Kα =100 %)
$K\alpha_3$	8.4 eV	9.2 %	9.6 eV	7.8 %
$K\alpha_4$	10.0 eV	5.1 %	11.5 eV	3.3 %

common transitions for both sources are listed in Table 2.6.

The advantage of a monochromatic source is a narrow x-ray line produced by Bragg diffraction in a toroidal $(10\bar{1}0)$ plane of a quartz crystal since only the major Al Kα component is diffracted. This results in an XP spectrum with narrower peaks without the ghost peaks from the x-rays satellites, listed in Table 2.6, that are inherent to the dual anode sources. The single anode, maintained at 15 kV is bombarded by electrons from a filament heated by applying a ~4.0 Ampere current. The heat generated from the 15 keV electron beam impinging the Al is dissipated by cooled water flow behind the anode. The

Al anode and the filament form the x-ray gun. The dual Al-Mg anode described above has a similar set-up.

The x-rays generated at the gun are monochromatized with a quartz crystal backplane set on a Rowland circle with a radius R. The larger the radius R, the smaller the energy spread in the x-ray spot [3]. The Kratos XPS uses a 500 mm Rowland circle monochromator, as shown in Figure 2.14. Overall, the monochromatized x-ray beam has only a fraction of the intensity that is obtained from a dual x-ray source since the monochromator filters all but the Al Kα transition line. All the x-rays, however, are focused on a spot at the sample surface approximately 350 μm in diameter producing a

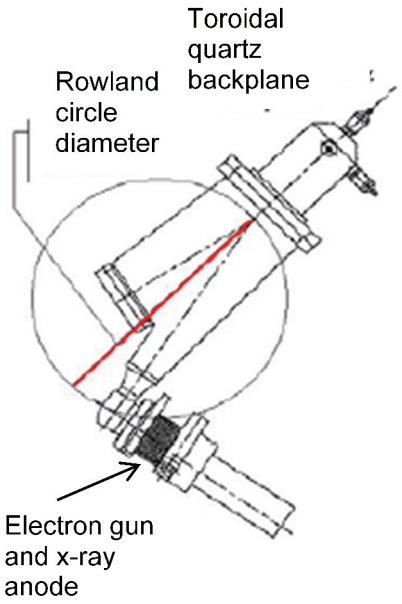

Figure 2.14: Schematic of the Al x-ray monochromator in the Kratos XPS [21]. The (1,0,-1,0) plane of quartz has the perfect lattice (4.25 Å, θ= 78.5^{o}) to diffract the Al Kα radiation of 1486.6 eV (8.33 Å).

high-flux x-ray beam. The high flux can complicate the XPS analysis of insulating materials that may accumulate surface charge while being irradiate with the intense beam.

The Kratos XPS uses a charge neutralization system to counteract the surface charging effects that may appear in the XP spectra of insulating materials. It consists of a

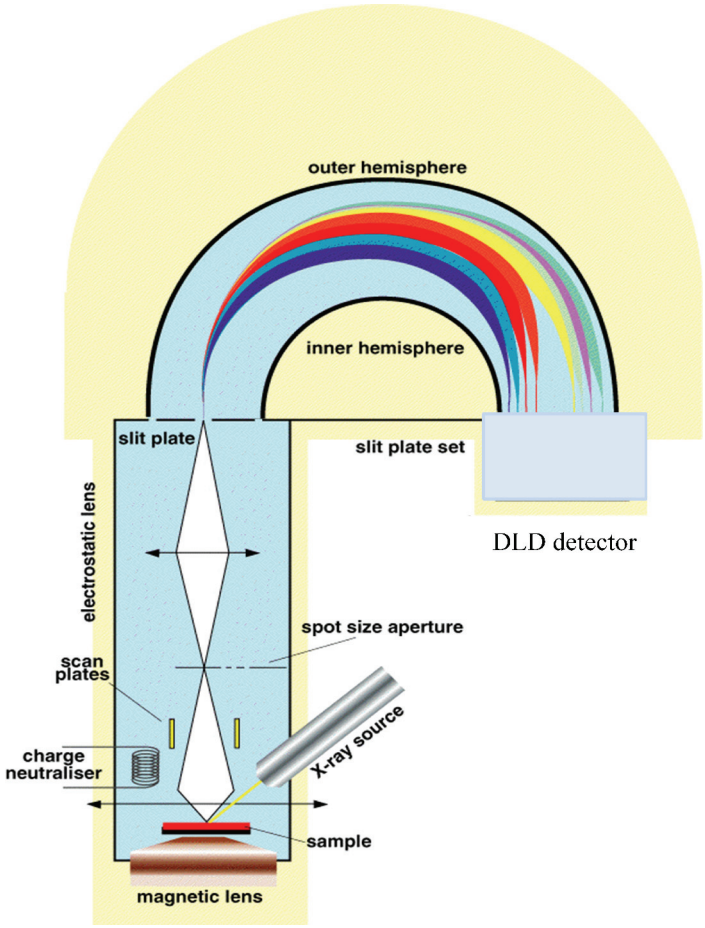

Figure 2.15: Diagram of the XPS experimental set-up. The emitted electrons, guided by the magnetic and electrostatic lenses, are focused at the slit plate of the electron analyzer (HAS). The HAS filters the electrons by kinetic energy as they enter the DLD detector [21].

filament to generate low energy thermionically emitted electrons and an electrode plate above the sample to transport the electrons to the surface of the sample. The effectiveness of the charge neutralizer in plutonium samples was investigated. Even though the oxides of plutonium are insulating in nature, particularly PuO_2, no charging effects were observed in the XP spectra of the metal samples with thin oxides on the surface. Nevertheless, the charge neutralizer was employ for data acquisition.

The electrons emitted from the sample are guided by a set of magnetic and electrostatic lenses to the entrance slit of the electron energy analyzer. This particular XPS system utilizes a 165 mm hemispherical sector analyzer (HSA) [32]. Figure 2.15 illustrates the experimental set-up of the components in the XPS instrument. The analyzer consists of two concentric hemispherical electrodes between which the electrons pass on their way to the delay line detector (DLD). The electrostatic fields within the (HSA) are set to only allow electrons of a given pass energy to arrive at the detector slits. The relationship of the pass energy *E*, and the applied potential *V* between the two concentric electrodes is given by the equation,

$$E = V\left[\frac{R_1}{R_2} - \frac{R_2}{R_1}\right]$$

where R_1 is the radius of the inner hemisphere and R_2 the radius of the outer hemisphere. The term within the brackets is referred to as the spectrometer constant. For XPS experiments, the analyzer and the lenses systems operated in the fixed analyzer transmission (FAT) mode. In this mode, the pass energy of the analyzer is held constant

while the lenses system retards the kinetic energy of the electrons to the range accepted by the analyzer. The pass energy setting determines the energy resolution of the analyzer. Higher pass energies reduce the energy resolution but increase sensitivity, as can be observed in Figure 2.16 and Figure 2.17. Figure 2.16 shows a set of XP spectra of a plutonium oxide film with both Pu^{4+} and Pu^{3+}. The binding energy difference between the two signals is 1.6 eV (426.0 eV vs. 424.4 eV). At a pass energy of 80 eV, it is difficult to

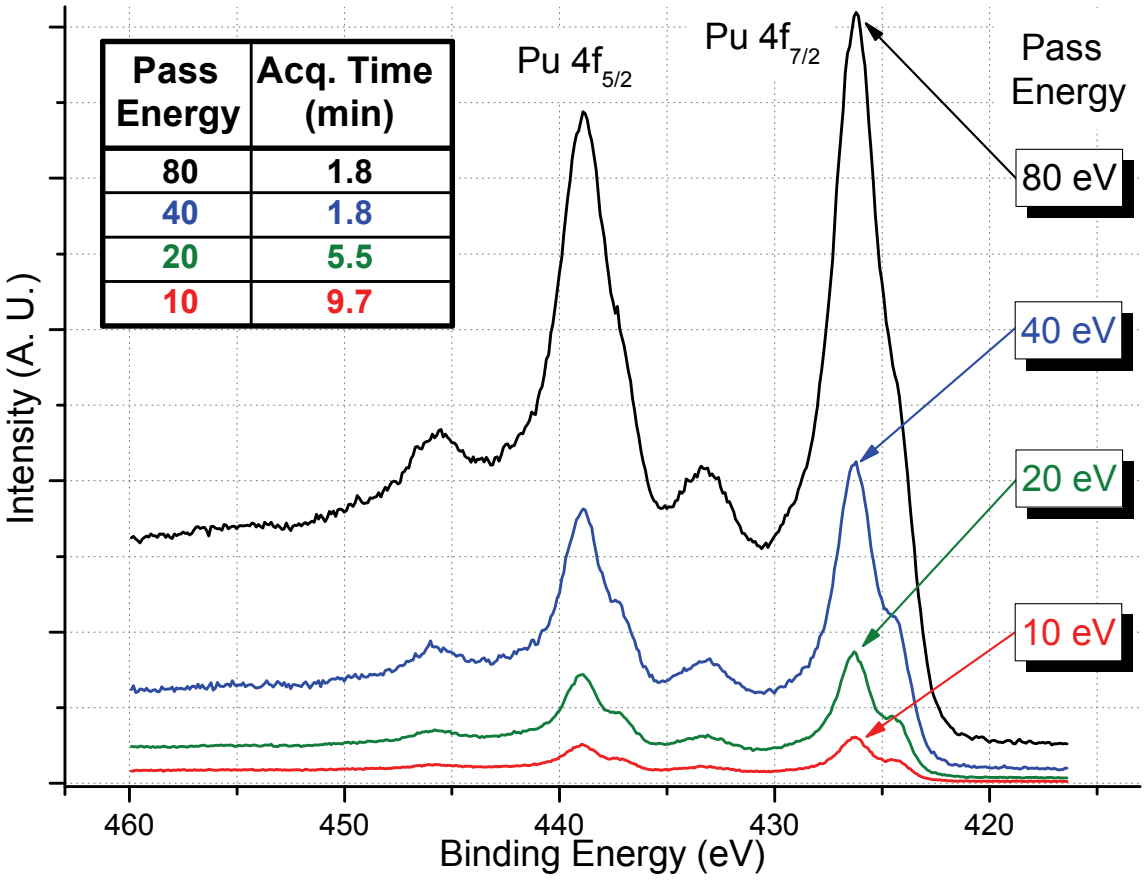

Figure 2.16: Pu 4f XP spectra of a plutonium oxide film as a function of analyzer pass energy. As the pass energy of the analyzer is decreased the energy resolution increases but the signal intensity decreases necessitating an increase in the data acquisition time (inset table) in order to maintain the signal to noise level.

see more than an inflection point in the line whereas at pass energies of 40, 20, and 10 eV it can clearly be seen. The XP spectra acquired at pass energies of 20, and 10 eV, when observed in the normalized plot in Figure 2.17, are practically identical indicating that the line width of the x-ray source has become the limiting factor in the resolution. For this work, the data acquired was collected at a pass energy of 40 eV, unless otherwise noted. This was done as a compromise between the resolution of the data and the acquisition time needed to obtain spectra of satisfactory signal to noise. While spectra collected at a

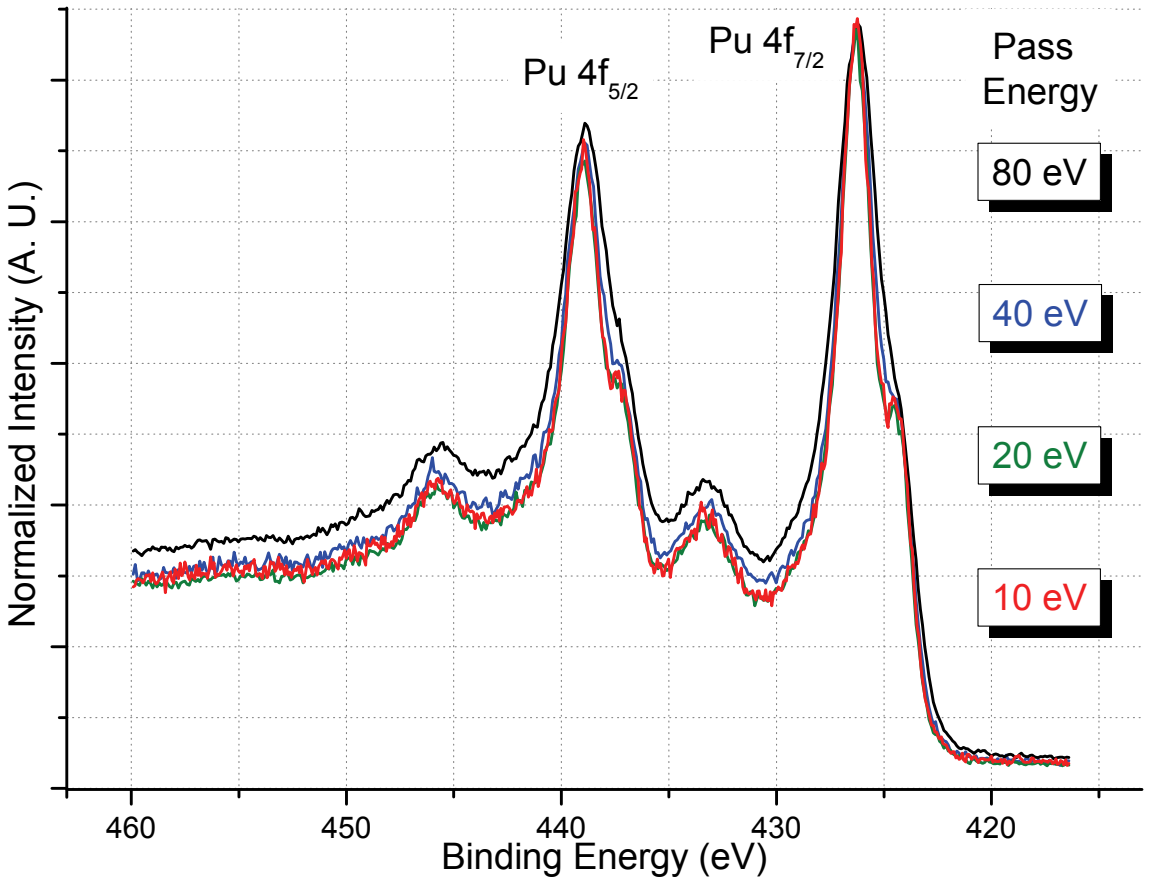

Figure 2.17: Normalized Pu 4f XP spectra of a plutonium oxide film as a function of analyzer pass energy. Spectra are the same as those in Figure 2.16 that have been normalized to the Pu $4f_{7/2}$ signal to better illustrate the increased resolution with decreasing pass energy.

pass energy of 20 eV offers slightly better resolution, the collection time is more than three times (5.5 vs. 1.8 minutes) longer than for spectra acquired at a pass energy of 40eV. The shorter collection time is vital for the experiments investigating a dynamic process such as the auto-reduction of PuO_2 to Pu_2O_3.

When a sample is introduced into an UHV system, it contains surface impurities that must be removed in order to acquire XPS data of the material. Sample cleaning is accomplished with ion sputtering of the surface. The Kratos XPS is equipped with a Mini-Beam III ion source gun [21]. This ion gun can operate between 1.0 and 5.0 kV to provide a high current density, scannable ion beam. The ion gun control provides the power and voltages necessary to operate the ion gun. The ion source is differentially pumped with a turbo molecular pump that allows the pressure inside the main analysis chamber to remain 10^4 times lower inside the ion source. Normal operation involves leaking argon gas into the gun where it is ionized by electron bombardment inside the ionization chamber, diagramed in Figure 2.18. The electrons, which normally are 200 eV in energy, are extracted from a rhenium filament through a grid. Ions generated in the center of the grid cylinder, are accelerated though the grid into the middle of the ionization region by the extraction electrode and extracted through a small aperture which acts as the source. The ionization chamber is at a high voltage with the beam energy equal to that of the filament. As the ions emerged from the extractor, they enter a set of plates and lenses, shown in Figure 2.19, which control the beam's direction and coherence. The X deflectors direct the beam's trajectory into the condenser lens, L_1. This lens determines the size of the beam; ions are focused near L_1 for small size or on the

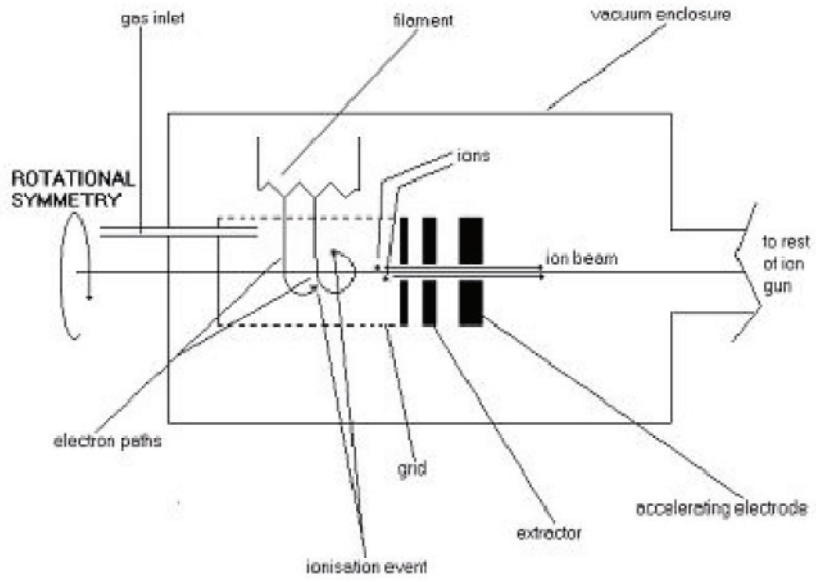

Figure 2.18: Diagram inside the ionization chamber of the Mini-Beam III ion source installed in the Kratos XPS [21].

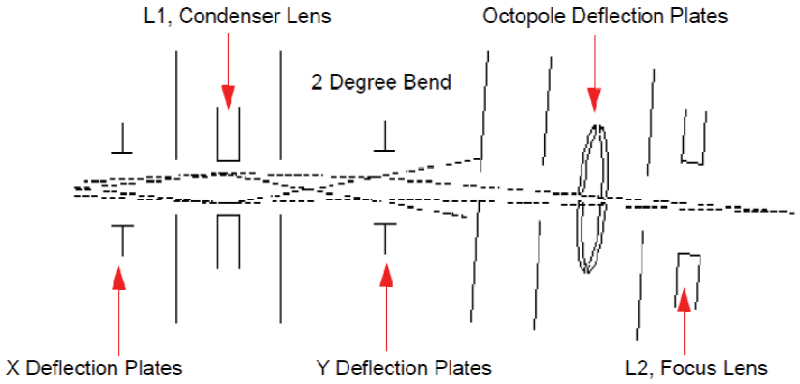

Figure 2.19: Schematic of plates and lens to control the beam of ions emerging from the extractor [21].

final aperture for large beam size. The Y deflection plates guide the ion beam around a 2^{o} bend in the ion column which removes energetic neutral argon atoms from the beam while guiding the ion beam toward the final lens. The octopole deflection plates raster the beam across the sample surface while the focus lens L_2 provides final adjustment of the sharpness of the ion spot on the surface.

During normal operation of the Mini-Beam III ion source, argon gas is introduced into the gun to a pressure of no more than $5*10^{-7}$ Torr. The energy of the beam is adjusted between 1.0 and 5.0 kV, the ion emission current is set to 10-30 mA, and the raster size and speed of the ion beam is selected. The ion filament current can vary between 1.6 to 2.2 A, depending on conditions. The UHV chamber does not have a valve between the analysis chamber and the ion pump. Thus, it is advisable to lower the ion pump voltage from the normal operating value of 5.0 kV to 3.0 kV to prevent the pump from overheating and shutting off during the sample cleaning cycles.

2.5.2 AES Instrument

The Auger electron spectra were acquired in a JEOL Jamp-7830F field emission Auger microprobe with incident electron energy of 10 kV and in constant retarding ratio mode (CRR=0.34). The sample was cleaned with 2 kV argon ion sputtering. Differentiated peak positions were used for elemental identification as follows: Pu metal at 317 eV, oxidized Pu peak at 314 eV, and oxygen at 511 eV [18]. Atomic concentrations and O/Pu ratios were determined using the differentiated peak-to-peak height and Pu (0.071), O (0.565), C (0.128), and Ga (0.451) sensitivity factors which

were optimized from the calculated values provided by the instrument manufacturer. While the sample analyzed with AES was not the same one employed for the XPS experiments, it was of similar composition. The sample preparation was similar for both techniques.

2.6 Gas Handling Manifold and Dosing

The gas handling manifold was constructed of ¼ inch stainless steel welded to Swagelok® VCR metal (silver platted SS) face seal fittings. The manifold system has a dedicated turbo molecular pump that can evacuate the lines to a pressure of $< 2*10^{-9}$ Torr during bakeouts and in between gas fillings. Gases are introduced into the UHV chamber via sapphire-sealed variable leak valves. Oxygen gas [33] is introduced into the gas manifold via SS gas canister with no more than 80 psi of gas. A residual gas analyzer (RGA) installed in the UHV chamber is employed to verify the purity of the gases introduced into system prior to the dose experiments. Oxygen dosing pressures were chosen to yield reasonable experimental exposure times, for the given dose. Gas doses throughout this work are given in Langmuir (L) exposure units where $1L = 10^{-6}$ Torr*sec.

2.7 Plutonium Sample and Manipulator

The poly-crystalline metal [34] employed for the XPS experiments presented in this thesis is a high-purity, electro-refined plutonium, stabilized in the δ phase with gallium (~2 atom %). The metal was homogenized for 50 hours at 450^{o} C followed by cooling to room temperature at a rate of 6-8^{o} C/min. An overview of the ICP-MS

elemental analysis, shown in Table 2.7, lists the impurities in the metal and the plutonium isotopical composition. A 7 mm X 7 mm X 12 mm metal sample was polished with decreasing sizes of diamond pastes down to 5 μm prior to mounting on the sample cup (illustrated in Figure 2.12) and introduction into the XPS instrument. Clean metal surfaces were prepared by argon ion sputter (5.0 kV beam energy, ~0.7 mA sample current, 15-30 min.) followed by heat annealing to 400-450^{o} C for 15-30 minutes. This ion sputter/heat-anneal cycles was repeated many times until the Pu 4f XP spectrum

Table 2.7: Elemental composition of the Pu sample utilized for the experiments presented in this work. Table 2.7a lists the amount of gallium, added to stabilize the δ-phase of Pu, and the main impurities. Table 2.7b lists the isotopic composition of plutonium [34].

a)

Element	ppm (at/at)
Ga	20414
^{241}Am	86.4
^{237}Np	38.9
U	58.8
Al	151
Ca	107
Si	170
Fe	118
Ni	20
W	16.5
C	161

b)

Pu isotopes	% (at/at)
^{238}Pu	0.12
^{239}Pu	93.956
^{240}Pu	5.897
^{241}Pu	0.095
^{242}Pu	0.041

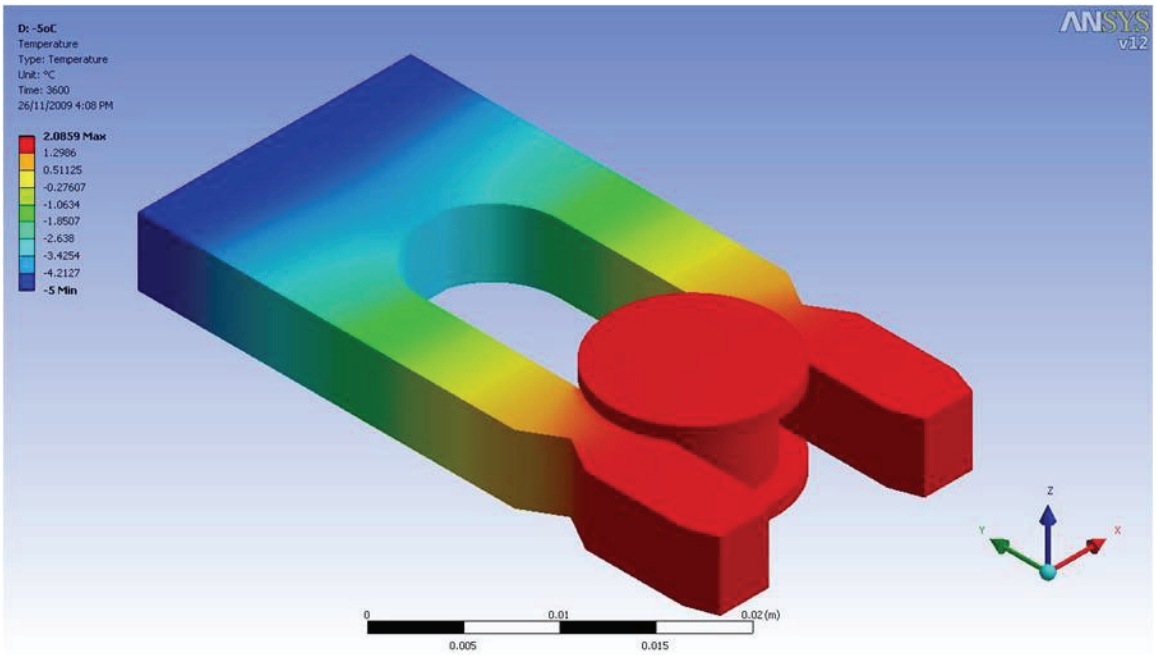

Figure 2.20: CAD drawing illustrating the results of a finite element simulation of the temperature gradient difference across the sample manipulator and sample holder with Pu sample. Dark blue indicated a temperature of -5^{o} C; red indicates +2^{o}C. The range of the gradient across the manipulator increases as the temperature at the left decreases.

indicated a metallic surface (binding energy of 422.2 eV) and the O 1s and C 1s regions were minimized. Carbide contaminated metal surfaces were prepared by argon ion sputter only.

Once the sample holder is introduced into the XPS system, it is attached to a liquid nitrogen cooled sample manipulator capable of cooling to less than -160^{o} C. The temperature is measured by a type K thermocouple fastened to an end of the manipulator than comes in contact with the sample holder. Hence, the temperature measured is not the temperature of the actual sample but of the manipulator/sample holder. At ambient

temperature, it is reasonable to accept the temperature of the sample to be the same as that of the manipulator. While cooling the manipulator with liquid nitrogen, this assumption is not likely valid. Indeed, actual measurements in an instrument with a similar setup indicated that the measured temperature of the sample manipulator and a sample mounted onto the manipulator is -120° and -40° C respectively, i.e., a temperature difference of 80° C [35]. This significant difference between thermocouple reading and

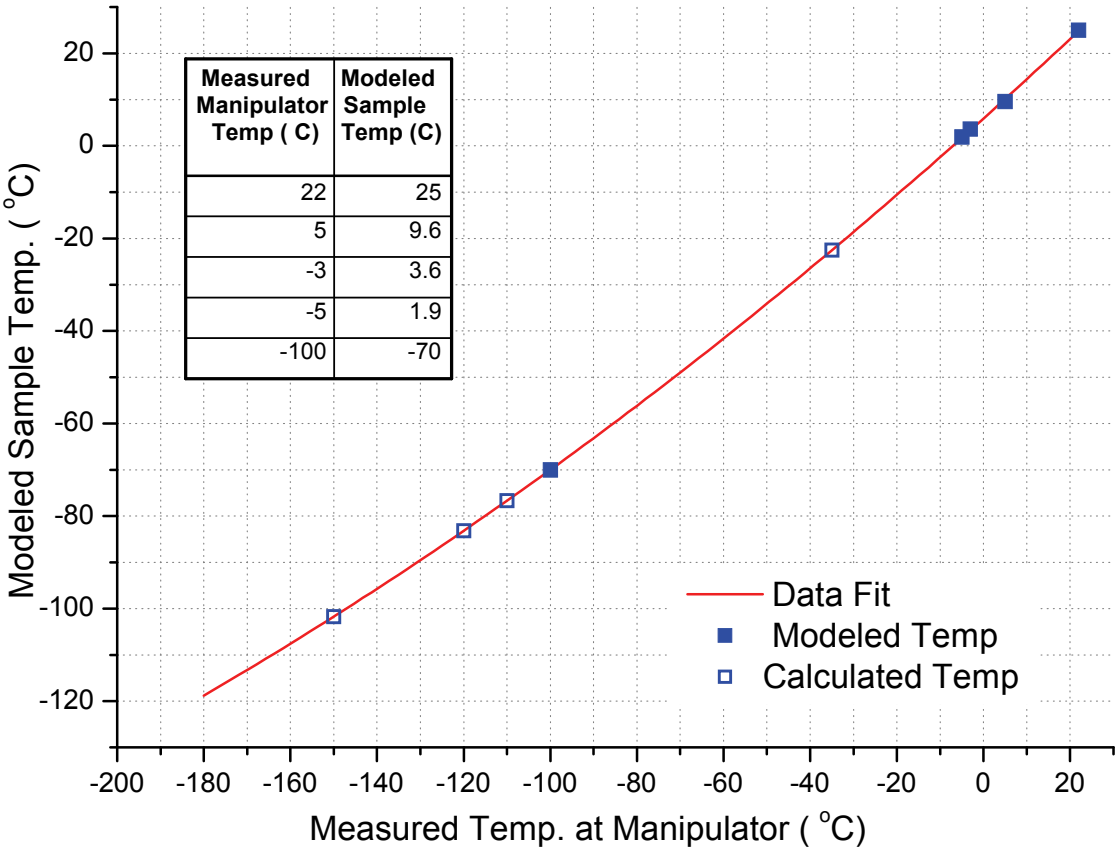

Figure 2.21: Relationship between the measured temperatures at the manipulator and the sample temperatures obtained from the ANSYS simulation. The five simulated temperature gradients (solid blue squares) are listed in the inset table. The open blue squares are manipulator temperature readings that where calculated from the linear regression fit of the five modeled temperatures.

actual sample temperature is largely ignored by most people. In an effort to obtain a more precise reading of the temperature of the actual sample in this experimental set-up, a CAD drawing of the manipulator and the sample holder and the hemispherical emittance of plutonium metal reported by Seery [36] were used in conjunction with the finite element analysis program ANSYS [37] to model the temperature difference between the Pu sample and the sample manipulator thermocouple reading. An additional factor accounted for is the heat generated as part of the radioactive decay process of plutonium. The heat output of the sample in this study was calculated [38] to be 4 mW/g based on the measured isotope concentrations listed in Table 2.7b. Figure 2.20 shows the results from a simulation of the temperature gradient across the sample manipulator. In this particular case, the -5^{o} C temperature would be the temperature reading of the thermocouple; the analysis shows that the sample temperature is $+2^{o}$ C. As part of this investigation, five temperature gradients were simulated.

Regressional analysis of this data set was performed. The result is plotted in Figure 2.21. The lowest temperature modeled was -100^{o} C. The results indicate that this thermocouple reading is equivalent to a sample temperature of -70^{o} C. The temperatures given throughout this work will be the temperatures calculated from the fit of modeled temperatures presented in Figure 2.21. Several oxidation experiments presented as part of this thesis were performed at lower measured temperatures than the lowest modeled manipulator temperature. For instance, utilizing the plotted fit in Figure 2.21, a measured manipulator temperature of -150^{o} C is equivalent to a sample temperature -102^{o} C.

Regardless of the value obtained from the fit, these temperatures will be stated as "less than -70^{o} C" to stay within the temperature range that were actually modeled.

2.8 XPS Data Analysis

All data analysis presented in this thesis was performed with CasaXPS® [39]. The separation of Pu 4f XP spectra into their individual components can be difficult and subject to variation in the fitted values due to factors such as start and end of the background region, full width-half max (FWHM) of each component peak, and Gaussian/Lorentzian character of the component peaks, among other factors. Small changes in these parameters can lead to variation in the determined values of Pu^{3+}/Pu^{4+} as well as the O/Pu concentration ratios. Great care has been taken to systematically analyze all of the data presented here with the same model (i.e. same peak shapes, FWHM, etc.) and boundary conditions.

The background intensity in XP spectra arises from the inelastic scattering of photoelectrons within the surface region. In order to achieve accurate quantification of the data, the background intensity in the XP spectra must be removed. The two types of backgrounds typically employ for XPS modeling are linear and non-linear. The linear background simply removes the background by approximating a straight line before and after the peak resulting in the removal of all the area beneath the photoelectron peak. While simple and efficient for symmetrical peaks with small background intensities, it is not an accurate reflection of the physics that govern the background intensity in an XPS spectrum. It is particularly ill-suited for large backgrounds and asymmetrical

photoelectron peaks, two characteristics that the 4f photoelectron signals of plutonium possess. The second type of background modeling is the non-linear. Numerous non-linear backgrounds have been developed [3], including Tougaard, Shirley, cubic spline, and many 'blended' combinations. The varied selection of non-linear background to choose from is an indication of the subjective manner with which surface scientists apply them. Among these, the Shirley background [40] is among the most commonly used models as it is realistic enough to allow for reproducible quantification of photoelectron signals. It is the model chosen for quantification in this work.

The basic feature of the Shirley [40] algorithm is the iterative determination of the background beneath the peak areas A_1, and A_2 to compute the background intensity $S(E)$ at energy E,

$$S(E) = I_2 + \kappa \frac{A_2(E)}{(A_1(E) + A_2(E))}$$

where κ is the step in the background and is equal to $(I_1 - I_2)$. Since $A_1(E)$ and $A_2(E)$ are not known without knowing the background intensity $S(E)$, The calculation of Shirley background from spectral data is an iterative process. Once the calculated value for $S(E)$ converges, its area is subtracted from the spectrum and the peak areas $A_1(E)$ and $A_2(E)$ are determined.

Core photoelectrons appear in XP spectra in a variety of line shapes. The particular shape is a combination of the physics involve in the process and the instrument's resolution. Ideally, a convolution of a Gaussian and Lorentzian function can

be employed to model the line shape of an observed peak in a spectrum. The Gaussian component describes the measurement process (x-ray line shape, instrument response) and the Lorentzian component models the lifetime broadening of the transition due to the uncertainty principle [41]. In reality, spectral signals are complex shapes that may have theoretical justified asymmetry or be a function of the instrument's inability to resolve the line shape accurately. Additionally, the uncertainty of the background shape modeling may also be a consideration. Thus, many synthetic line-shape functions are available to fit XP spectra. It is up to data analyst to choose an appropriate line-shape and to apply it as objectively as possible to the entire data set when attempting to draw conclusions from XPS data.

After extensive evaluation of the plutonium 4f core photoelectron line shape, a modified Lorentzian asymmetric function [41] was selected to fit the signal. The Lorentzian line shape with FWHM *F* and energy *E* (in kinetic energy) is given by

$$L(x) = \frac{1}{1 + 4\left(\frac{x - E}{F}\right)^2}$$

The line shape is obtained from

$$LA(\alpha, \beta) = \begin{cases} [L(x)]^{\alpha} & where\ \ x \leq E \\ [L(x)]^{\beta} & where\ x \geq E \end{cases}$$

where the parameters α and β

$$\alpha = 3 - \frac{3 - a}{1 + 4\left(\frac{x - E}{w}\right)^2} \qquad \beta = 3 - \frac{3 - b}{1 + 4\left(\frac{x - E}{w}\right)^2}$$

determine the spread of the tail for the Lorentzian curve at either side resulting in a steeper edge of the line shape. The modified Lorentzian line shape utilized for fitting the Pu 4f XPS signal in this work has the form *LF* (α, β, *w*, *m*). The function is identical to the *LA* (α, β) presented above. The *w* damping parameter forces the tail to reduce toward the limit of integration. The *m* parameter defines the width of the Gaussian component of the function. The asymptotic form of the *LF* line shape is equivalent to the theoretical Doniach-Sunjic (D-S) asymmetric line shape. Thus, this line shape is a practical solution to the infinite nature of the D-S line shape.

Plutonium metal has a broad spectral feature at 284.2 eV corresponding to the $5p_{1/2}$ photoelectron [11, 42] and very little adventitious carbon due to the sputter cleaning process, making use of the C 1s as an energy reference difficult. Thus, binding energies for all data reported here were referenced to the Pu $4f_{7/2}$ transition for Pu^{3+} at 424.4 eV. After referencing, binding energies for the remaining transitions of interest are as follows: Pu $4f_{7/2}$ for the Pu^{4+} species at 426.0 eV and metal at 422.2 eV, O 1s at 530.2 eV for the sesquioxide oxygen, 529.8 eV for the dioxide oxygen, and 532.2 eV for a possible surface hydroxyl species or some other oxygen-containing species. These binding energies are consistent with values previously reported [11, 42-45].

A significant amount of effort was invested to consistently analyze, as a whole, the data presented in this work in order to quantitatively and qualitatively compare the results and reach valid conclusions regarding the stoichiometries of the prepared oxide films. The plutonium oxide film stoichiometry was determined by: 1) Using only the

intensity of the oxide oxygen species at ~ 530 eV. 2) Subtracting any metallic plutonium contribution from the Pu 4f envelope so that only the oxidized plutonium Pu^{ox} (Pu^{3+} and Pu^{4+}) species are used. Accurate fitting of the Pu 4f spectral features is necessary for quantification of the data. As has been illustrated elsewhere, it is difficult to do this accurately [46]. The next figures, will present XPS Pu 4f regions of a variety of plutonium surfaces and the contributions assigned (Pu^0, Pu^{3+}, and Pu^{4+}) to each spectrum. The Shirley background model and the modified asymmetric Lorentzian line shape "*LF*"

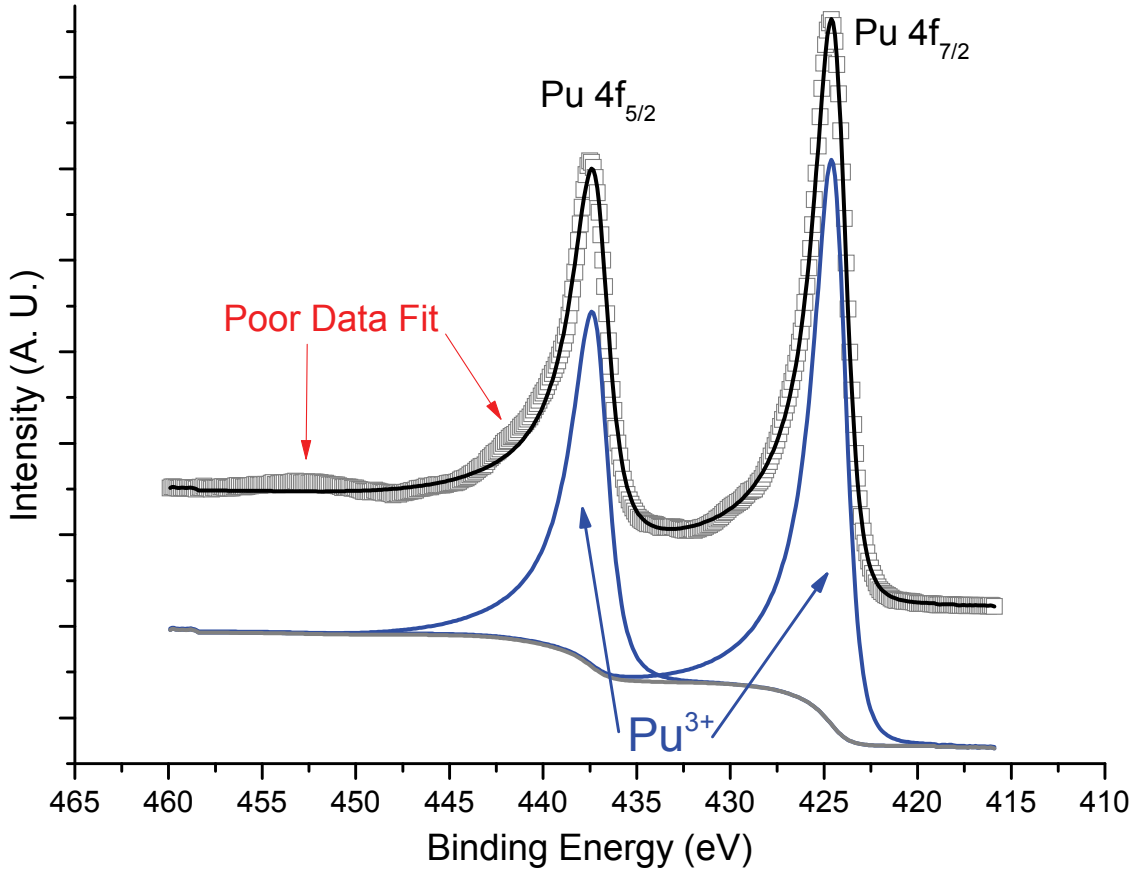

Figure 2.22: Plot of the plutonium 4f XP spectrum (grey squares) of a Pu_2O_3 surface showing two synthetic peaks (blue traces) and the Shirley background (gray trace) used to fit the data set. With only two synthetic peaks employed, there are two regions within the Pu 4f envelope where the fit to the data is poor (red arrows).

found in the CasaXPS® software [41] was employed to fit all the data discussed here.

Figure 2.22 shows the XP spectrum of the Pu 4f photoelectron for a Pu_2O_3 surface as gray squares. The black trace over the experimental data points corresponds to the sum of the background and the two asymmetrical Lorentzian synthetic peaks used to fit the data (424.4 and 437.2 eV). The Pu $4f_{7/2}$ peaks exhibits excellent fit with a single *LF* synthetic component. In the case of the Pu $4f_{5/2}$ which is also fitted with a single *LF* synthetic component, the fit is adequate for most of the peak but there is a region at approximately 440 eV where the fit is poor. Despite considerable efforts invested varying the *LF* synthetic peak parameters (α, β, w, m discussed previously) in an attempt to find the optimal combination, the area cannot be properly fitted without degrading the overall fit of the peak. Additionally, there is a region at approximately 453 eV where the fit is poor. Figure 2.23 shows the same data set as in Figure 2.22 with a different fit. The Pu $4f_{7/2}$ and $4f_{5/2}$ are fitted with a pair of *LF* synthetic peaks and an additional pair of 'satellite' peaks has been added at 440.2 eV and 453.0eV. It is unclear whether these previously unreported low intensity features are due to satellites, such as the 'shake-up', or some other process. The energy difference between the two synthetic peaks is 12.8 eV, the same energy difference as the spin orbit splitting of the $4f_{7/2}$ and $4f_{5/2}$ peaks. The 12.8 eV energy difference of the two synthetic peaks is the right amount to result in a satisfactory fit for the entire Pu 4f envelope. It is possible that the added intensity at 440.7 eV may be due to greater asymmetry of the $4f_{5/2}$ when compared to the $4f_{7/2}$. This explanation, however, leaves the intensity at 453.0 eV as an unexplained phenomenon.

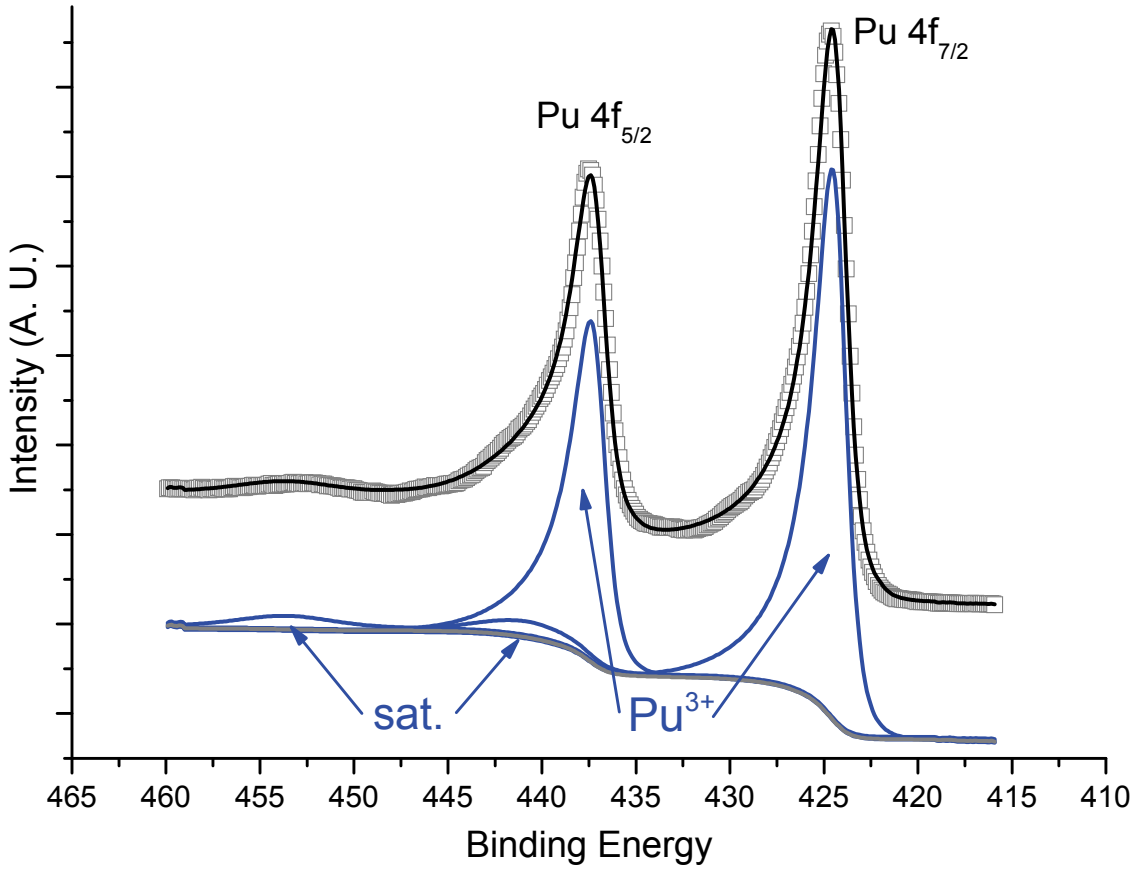

Figure 2.23: Plot of the plutonium 4f XP spectrum (grey squares) of a Pu_2O_3 surface showing two main synthetic peaks, two satellite synthetic peaks (blue traces centered at 440.2 and 453.0 eV) and the Shirley background (gray trace) used to fit the data set. The addition of the two satellites affords a better overall fit than with just two components, as in Figure 2.22.

The intensity of all four synthetic peaks was taken into account during determination of the relative atomic concentration of the Pu^{3+} species.

Figure 2.24 shows an XP spectrum of a surface with a Pu^{4+} film on top of a Pu^{3+} oxide film. The knowledge of the Pu^{3+} spectral envelope, discussed previously, allows for reasonably accurate determination of the representative XP spectra and relative atomic

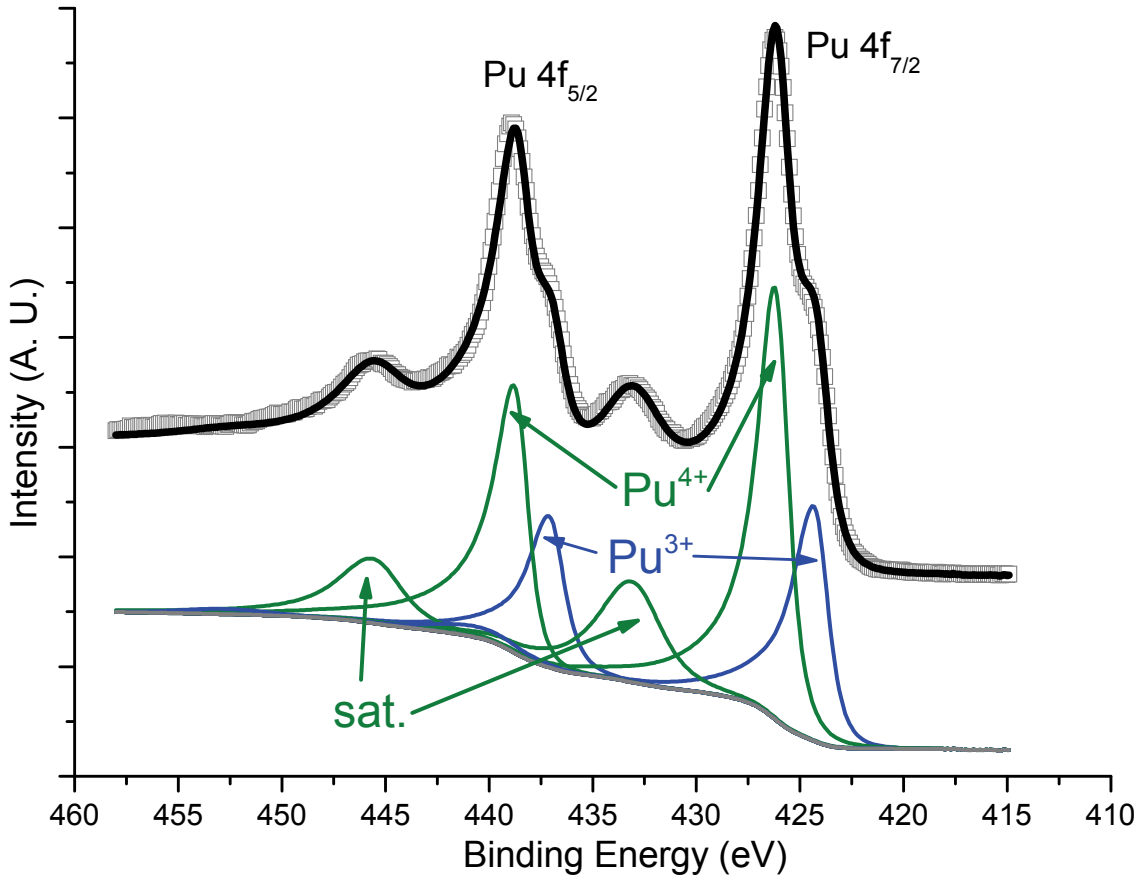

Figure 2.24: Plot of the plutonium 4f XP spectrum (grey squares) of a PuO_2/Pu_2O_3 (Pu^{4+}/Pu^{3+}) surface showing the data fit (black trace) as well as the synthetic peaks for the Pu^{3+} species (blue traces : 424.4 eV, 437.2 eV,440.2 eV, and 453.0 eV) , the Pu^{4+} species (green traces: 426.0 eV, 433.0 eV, 438.6 eV, and 445.5 eV), and the Shirley background (gray trace) used to fit the data set.

concentration of the Pu^{4+} species. The resulting fit of the Pu^{4+}, with two main synthetic peaks and a pair of satellites agrees with what has been previously observed [47].

Figure 2.25 shows the XP spectrum representative of the cleanest plutonium surface prepared during the course of the work presented in this thesis. Nevertheless, two features (blue trace) attributed to Pu^{3+} can be clearly observed. There is controversy

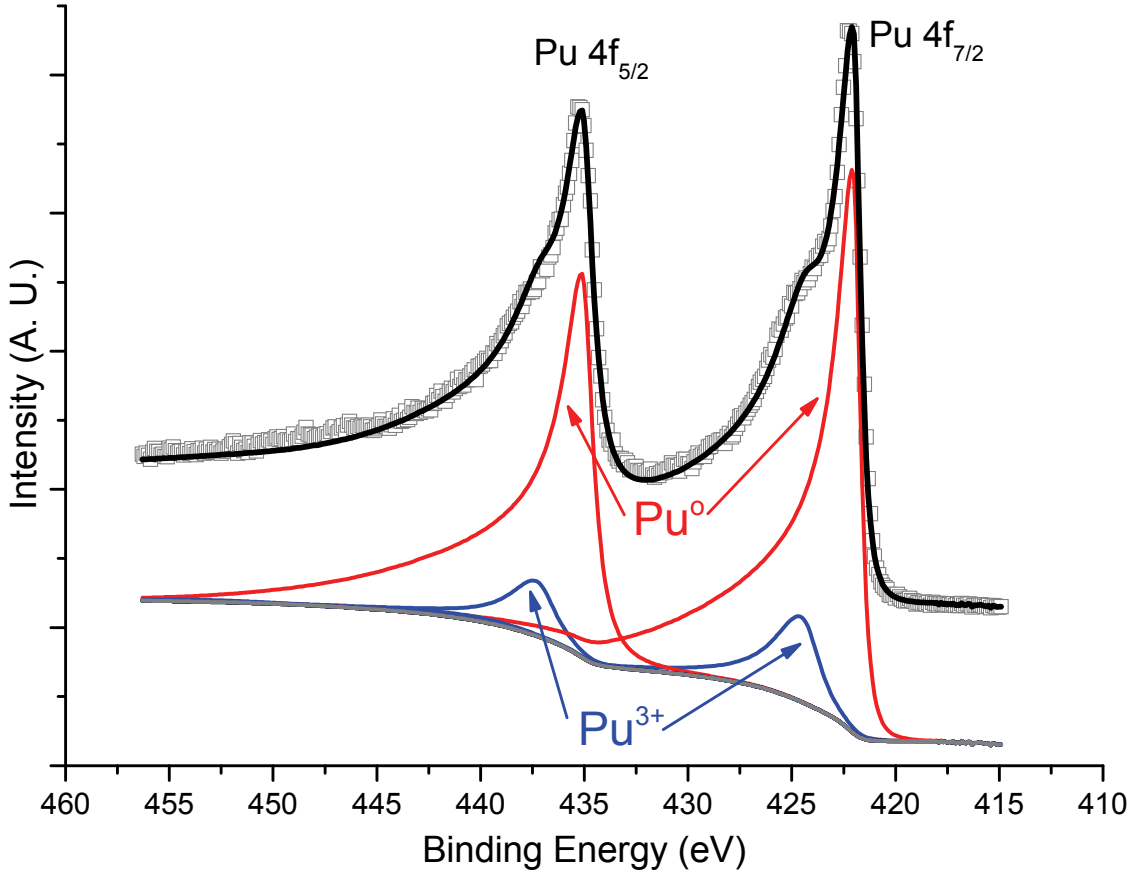

Figure 2.25: Plot of the plutonium 4f XP spectrum (grey squares) of a Pu metal with a small amount of Pu^{3+} on the surface showing the data fit (black trace) as well as the synthetic peaks for the Pu^{3+} species (blue traces), the Pu metal species (red traces: 422.2 eV, and 435.1 eV), and the Shirley background (gray trace) used to fit the data set.

regarding the nature of this high binding energy shoulders on the main 4f photoelectron doublet; they have been attributed to 'poorly screen' 4f photoelectrons from Pu metal [47]. It has been observed in the course of this work, however, that the feature in question is directly related to the amount of oxygen, and thus Pu^{3+}, on the surface of the metal. The source of the oxygen is likely due to the presence of small amounts of oxide in the bulk or reaction of the surface with residual gas in the UHV chamber.

2.9 Plutonium Sensitivity Factor Determination

Accurate relative sensitivity factors (RSF) for transitions of interest are required for quantification of surface species with XPS. Relative sensitivity factors take into account variables such as the photoelectron cross-section and analyzer transmission efficiency (i.e., transmission function). The RSF's for a given instrument are typically provided by the instrument manufacturer. For the quantification of XP spectra in this work, a value of 0.78 was used for the O 1s data and 0.278 for the C 1s data (both relative to a F 1s value of 1), as provided by the instrument manufacturer [21]. However, no RSF was provided for plutonium, as it is a hazardous and radioactive material with strict access and handling requirements.

There are several reports of the Pu 4f RSF in previous studies. One such study used calculated photoelectron cross-sections and a known sensitivity factor (U 4f) to determine the RSF for Pu 4f and other transuranics [46]. A value of 17.87 was reported for the Pu 4f region (10.21 for the Pu $4f_{7/2}$) relative to a F 1s value of 1. Another study in which data from oxidized plutonium was used to experimentally determine the Pu 4f RSF reported a value of 92.1 relative to a C 1s value of 1 [48]. These values, when referenced to the same transition, are different by approximately 25% [48]. This would lead to a corresponding relative concentration variation of 25% on Pu surfaces depending on the RSF used. In order to be more confident in the oxygen to plutonium relative atomic concentration ratios reported in this work, a RSF for the Pu 4f transition has been determined as part of this work.

The RSF for plutonium used throughout this thesis was estimated by comparison of calculated photoelectron cross-sections [49] to RSF's for other 4f transitions provided with the instrument from the manufacturer. This resulted in a value of 20.62 for the Pu 4f transition relative to a F 1s value of 1.00. Using the RSF for the C 1s transition provided with the instrument used here (0.278), a value of 74.18 for the Pu 4f transition is obtained when setting the C 1s value at 1. The Pu 4f RSF obtained here is between the two values previously reported [46, 48]. Further confidence can be gained in the RSF by comparing quantification results from data with known stoichiometries.

For determination of relative atomic concentrations from XP spectra, a plutonium relative sensitivity factor (RSF) of 22.68 (relative to a F 1s value of 1) was used. This value was adjusted from the calculated 20.62 (discussed before) in order to most accurately represent the stoichiometry of plutonium dioxide (assuming; for PuO_2, O/Pu = 2.00) in all of the relevant data collected in our laboratory with this instrument. It is possible that this determination of the RSF, and therefore the reported atomic concentrations, may not be absolutely correct. However, all comparisons of relative concentrations (stoichiometries) remain valid, as even if the RSF is incorrect, all O/Pu ratios must be scaled equally.

References

[1] McNaught, A. D. and Wilkinson, A., Compendium of Chemical Terminology, *The Gold Book,* 2nd Edition, (Blackwell Science, 1997).

[2] Koopmans, T., *Physica*, **1** (1933) 104.

[3] Briggs, D. and Seah, M. P., Practical Surface Analysis, Volume 1: Auger and X-ray Photoelectron Spectroscopy, 2nd Edition (John Wiley & Sons, New York: 1990), p. 114.

[4] Tougaard, S. and Sigmund, P., *Phys. Rev. B*, **25** (1982) 4452.

[5] Tougaard, S., *Surf. Interface Anal.*, **11** (1988) 453.

[6] Briggs, D. and Seah, M. P., Practical Surface Analysis, Volume 1: Auger and X-ray Photoelectron Spectroscopy, 2nd Edition (John Wiley & Sons, New York: 1990), p.106.

[7] Burroughs, P., Hamnett, A., Orchard, A. F., Thomton, G., *J. Chem. Soc. Dalton Trans.*, **17** (1976) 1686.

[8] Fitton, G. , X-Ray fluorescence spectrometry, in Gill, R. (ed.), Modern Analytical Geochemistry: An Introduction to Quantitative Chemical Analysis for Earth, Environmental and Material Scientists, (Addison Wesley, Longman, UK: 1997).

[9] Auger, P., *Cr. Hebd. Acad. Sci.*, **177** (1923) 169.

[10] Auger, P., *Cr. Hebd. Acad. Sci.*, **180** (1925) 65.

[11] Baptist, R., Courteix, D., Chayrouse, J., Heintz, L., *J. Phys. F:Met. Phys.*, **12** (1982) 2103.

[12] Muilenburg, G. E., Handbook of X-ray Photoelectron Spectroscopy, (Perkin-Elmer, Eden Prairie, MN:1979)

[13] Semak, B. S., van der Marel, C., Tougaard, S., *Surf. Interface Anal.*, **33** (2002) 238.

[14] Kover, L., Tougaard, S., Toth, J., Daroczi, L., Szabo, I., Langer, G., Menyhard, M., *Surf. Interface Anal.*, **31** (2001) 271.

[15] Chaparro, A. M., Maffiotte, C., Herrero, J., Gutierrez, M. T., *Surf. Interface Anal.*, **30** (2000) 522.

[16] Butcher, K. S. A, Tansley, T. L., Li, X., *Surf. Interface Anal*., **25** (1997) 99.

[17] Arranz, A., Palacio, C., *Surf. Interface Anal.*, **29** (2000) 392.

[18] Larson, D. T., Adams, R. O., *Surface Science*, **47** (1975) 413.

[19] Auger spectrum courtesy of Dr. D. P. Moore.

[20] Swagelok Corporation, www.swagelok.com.

[21] Operator's Manual 39-306, Kratos Analytical, Wharfside, Trafford Wharf Road, Manchester, M17 1GP, U. K.

[22] Haschke, J. M., *Diffusion and Intermetallic Formation in the Pu-Fe System*, Memorandum NMT-5:98-001, Los Alamos National Laboratory, OCT 1997.

[23] Pahl, R. G., Lahm, C. E., Hayes, S. L., *J. Nucl. Mater.*, **204** (1993) 141.

[24] Chavarria, R., Koman, D., *Actinide Research Quarterly*, **1st/2nd Quarter** (2008) 14.

[25] Tantalum rod, 99.95%, 16 mm diameter. Part # 156-249-29; Goodfellow Corporation, 305 High Tech Drive, Oakdale, PA 15071, USA.

[26] Wick, O. J., Plutonium Handbook- A Guide to the Technology, Vol. I & II, (American Nuclear Society: 1980), p. 121.

[27] Mills, I., Cvitas, T., Homann, K., Kallay, N., Kuchitsu, K.,Eds., Quantities, Units, and Symbols in Physical Chemistry 2nd Edition, (Blackwell Science: 1997).

[28] Gas Drying Unit (stock No. 26840); W. A. Hammond DRIERITE Co. LTD., Xenia, OH 45385.

[29] BOC Edwards Item No. D029-00-390; BOC Edwards, Manor Royal, Crawley, West Sussex, RH10 2LW, U.K.

[30] BOC Edwards Item No. D386-61-000; BOC Edwards, Manor Royal, Crawley, West Sussex, RH10 2LW, U.K.

[31] Varian Vacuum Technologies, Lexington, MA 02421.

[32] Sar-El, H. Z., *Nucl. Intrum. Methods.*, **42** (1966) 71.

[33] O_2 gas, 99.99% ; Scotty Specialty Gases, Air Liquide America Specialty Gases, 6141 Easton Road, Plumsteadville, PA 18949.

[34] Plutonium metal sample and the purity analysis provided by Dr. F. J. Freibert.

[35] Dr. P. Roussel, private communication.

[36] Seery, W. N.*, J. Nucl. Mater.*, **25** (1968) 64.

[37] ANSYS, Inc., Southpointe, 275 Technology Dr., Canonsburg, PA 15317 USA.

[38] Wick, O. J., Plutonium Handbook- A Guide to the Technology, Vol. I & II, (American Nuclear Society:1980), p. 8.

[39] Fairley N., CasaXPS®, Casa Software LTD., Bay House, 5 Grosvenor Terrace, Teignmouth, Devon, TQ14 8NE, UK.

[40] Shirley, D. A., *Phys. Rev. B*, **5** (1972) 4709.

[41] Fairley, N. and Carrick, A., The Casa Cookbook: Recipes for XPS Data Processing, (Acolyte Science, Manchester, England:2005).

[42] Tull, S., *Ph.D.* Thesis, University of Wales, Cadiff, U. K., 2003.

[43] Terry, J., Schulze, R. K., Farr, J. D., Zocco, T., Heinzelman, K., Rotenberg, E., Shuh, D. K., van der Laan, G., Arena, D. A., and Tobin, J. G., *Surf. Sci. Lett*., **499** (2002) L141.

[44] Veal, B. W., Lam, D. J., Diamond, H., Hoekstra, H. R., *Phys Rev. B*, **15** (1977) 2929.

[45] Farr, J. D., Schulze, R. K., Neu, M. P., *J. Nucl. Mater.*, **328** (2004) 124.

[46] Gouder, T. and Havela, L., *Mikrochim. Acta*, **138** (2002) 207.

[47] Courteix, D., Chayrouse, J., Heintz, L., Baptist, R., *Solid State Comm.*, **39** (1981) 209.

[48] Morrall, P., Roussel, P., Jolly, L., Brevet, A., and Delaunay, F., *J. Nucl. Mater.*, **385** (2009) 15.

[49] Scofield, J. H., *J. Electron Spectrosc.*, **8** (1976) 129.

Chapter 3: Early Stages of Plutonium Oxidation

While the oxidation states, stoichiometries and crystallographic structure of the plutonium oxides (PuO_2 & Pu_2O_3) in the bulk powder form have been studied and elucidated [1-4], the body of knowledge regarding the nature of oxide films on the metal surface is not as extensive. Using the results from these bulk oxides investigations as justification, many studies on Pu oxidation and the Pu-oxide thin film system assumed that the oxide is composed of plutonium sesquioxide as the stable oxide at the oxide-metal interface on a plutonium metal surface [5-8]. However, there are practically no published data investigating the earliest stages of plutonium oxidation, or how factors such as temperature, pressure, and time may affect the oxide formed on a Pu metal surface. If we are to expand our knowledge of the corrosion of plutonium, the earliest stages of this process must be understood.

In this chapter, the effects of temperature, pressure, dose and time on very thin plutonium oxide films on clean metal will be investigated in order to determine how the oxide film composition is affected. The results show that extrapolation of behavior in bulk oxides to thin films is not as straightforward as historically assumed for plutonium. A new oxide, Pu_2O_{3-y}, will be proposed at the metal-oxide interface.

3.1 Oxygen Exposures of Clean Plutonium Metal

In order to investigate the initial stage of the oxidation of plutonium metal, XPS was employed to construct oxygen uptake curves by determining the atomic

concentrations of plutonium and oxygen on the surface of a metal sample as a function of oxygen gas exposure. The Pu 4f XP spectra obtained after each oxygen dose were fitted to separate the Pu metal component (422.0 eV) from the oxidized Pu component (424.4 eV), which in these small oxygen exposures experiments is the Pu^{3+} species. The O 1s XP spectra were fitted to separate the oxide signal (530.0eV) from possible surface hydroxyl species (532.0 eV). The experimental details, including assumptions for the data analysis, sensitivity factors, and data fitting parameters, were described in detail in the experimental section. For these particular experiments presented below, a clean plutonium metal surface was prepared by repeated cycles of argon ion sputtering and annealing (450^{o} C) until the carbon 1s and oxygen 1s signals were below the limits of detection for the instrumental conditions employed here.

The results for the sequential oxygen exposure of a clean plutonium metal surface at two different pressures, 10^{-7} and 10^{-8} Torr, are shown in Figure 3.1. For the exposures performed at 10^{-7} Torr in 10 *L* increments (*L* = Langmuir = 1×10^{-6} Torr·s), nearly 100% of the Pu 4f signal corresponds to Pu^{3+} at exposures greater than 30 *L*. The 10^{-8} Torr exposure data (2 *L* increments) show that a small amount (~20%) of plutonium metal is still observed at exposures of 30 *L*. The corresponding $O:Pu^{ox}$ stoichiometric values, while similar for the two experiments, differ significantly from the value typically assumed for plutonium sesquioxide (O:Pu =1.5), as illustrated in Figure 3.1a. The average oxygen to oxidized plutonium atomic ratio for the 10^{-8} Torr incremental exposure is ~1.1, regardless of total cumulative oxygen dose. Incremental exposures at 10^{-7} Torr of

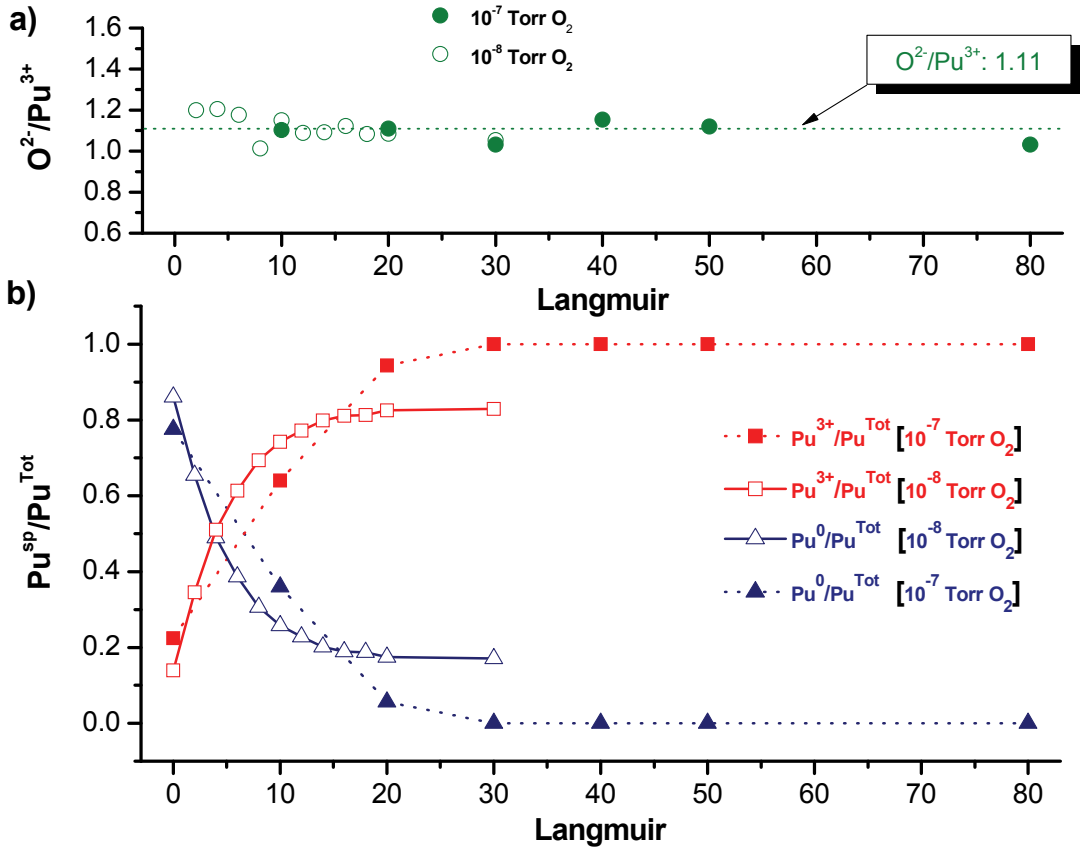

Figure 3.1: Sequential oxygen exposure at 26° C. Results from XPS analysis of a clean plutonium metal surface exposed to O_2 at $1x10^{-8}$ Torr (open symbols) and $1x10^{-7}$ Torr (solid symbols). The oxygen to oxidized plutonium (O^{2-}/Pu^{3+}) concentration ratios are shown in **a)** and the relative intensity ratios of metal (Pu^{o}/Pu^{Tot}) and trivalent plutonium (Pu^{3+}/Pu^{Tot}) in **b)**.

oxygen (up to 80 *L*) also show an O^{2-}:Pu^{ox} ratio of ~1.1. This value remains constant from very thin oxide films at the lowest two exposures of 10 and 20 *L*, where the oxidized plutonium accounts for ~65% and ~90% of the Pu 4f signal respectively, to the 80 *L* data point where the Pu 4f signal is due entirely to oxidized plutonium. The C 1s region for both experiments was monitored to ensure the absence of carbon, especially oxy-carbide species, throughout the duration of the experiments to ensure that no surface carbon contamination was occurring. Figure 3.1b indicates that the initial stage of oxidation is

faster at 10^{-8} Torr, as shown by the higher initial slope in the growth of the Pu^{3+} species. However, when the pressure difference of the two experiments is considered (factor of 10), the oxidation of plutonium at 10^{-8} Torr occurs much more slowly than at 10^{-7} Torr. Using the time elapsed for the Pu 4f XPS signal to be 50% Pu metal and 50% Pu^{3+} as a point of reference, the 10^{-8} Torr exposures (220 seconds) is approximately thirteen times slower than the 10^{-7} Torr exposure (17 seconds).

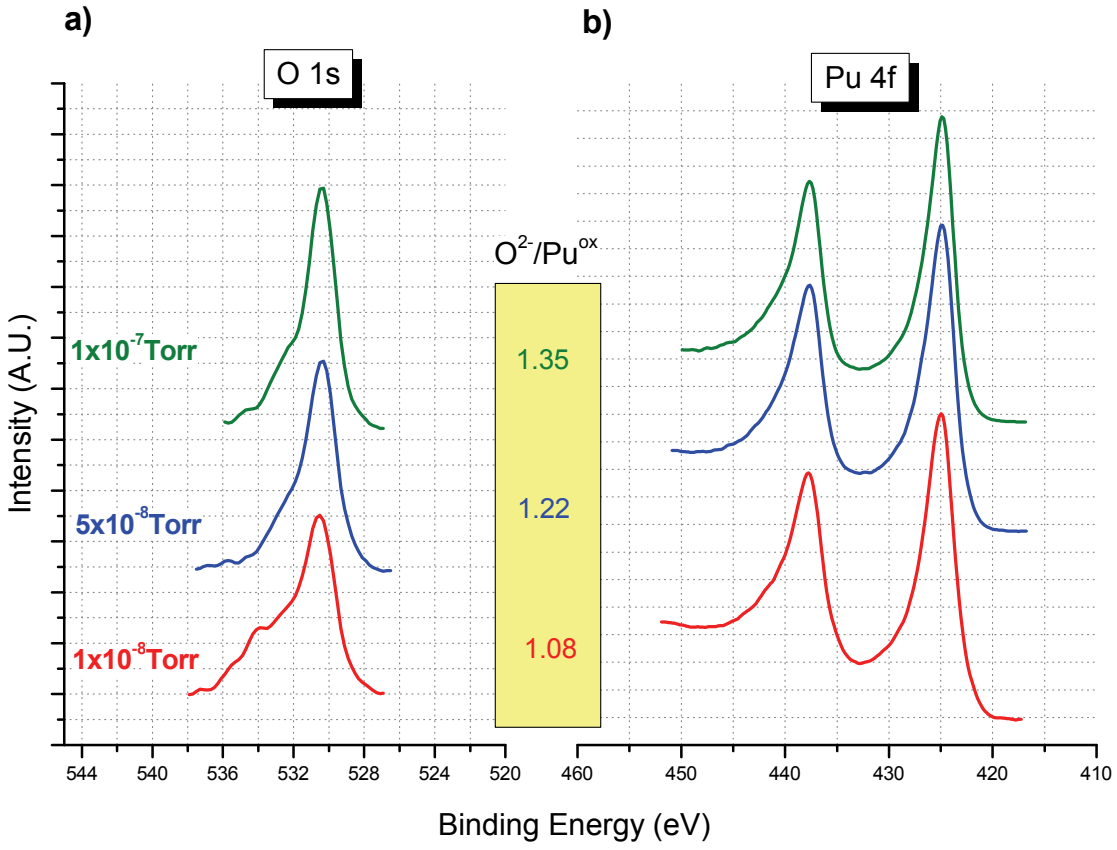

Figure 3.2: 30 *L* oxygen exposure at different pressures. XP spectra from the **a)** O 1s and **b)** Pu 4f regions for three plutonium oxide films grown by exposure to 30 *L* of O_2 at $1x10^{-7}$ Torr (green), $5x10^{-8}$ Torr (blue), and $1x10^{-8}$ Torr (red). All spectra are normalized to the Pu 4f area.

Figure 3.2 shows XPS data for the O 1s and Pu 4f spectral ranges, which contain information about the chemical environment of the elements in the thin oxidized film. The spectra shown are from another set of experiments in which clean plutonium metal surfaces were exposed to a single dose of 30 *L* of oxygen at 1×10^{-8}, 5×10^{-8}, and 1×10^{-7} Torr**.** These include the same exposure pressures as were used for the studies presented in Figure 3.1. The oxygen exposures in Figure 3.2 were performed in a single step, as opposed to multiple steps used in Figure 3.1. The 30 *L* exposure at 1×10^{-8} Torr of oxygen produced an oxide film with an O/Pu^{ox} ratio of 1.08, close to the average value of 1.11 obtained for the films prepared in Figure 3.1. However, unlike Figure 3.1, this single-step 30 *L* exposure resulted in oxidation of nearly all (~95%) of the plutonium observed in the near-surface region. For a single-step 30 *L* exposure at 1×10^{-7} Torr of oxygen, a O^{2-}/Pu^{ox} value of 1.35 was observed, as opposed to an average value of 1.11 for the sequential 30 *L* exposure. The Pu 4f region also shows the absence of metallic Pu, indicating that the analyzed surface is composed entirely of oxide. The exposure at 5×10^{-8} Torr resulted in

Table 3.1: Change in stoichiometry, with time, of a single-step 30 *L* oxygen exposure at varying pressures.

Exposure Pressure (Torr)	Stoichiometry (O^{2-}/Pu^{3+})	
	Initial Analysis	After 12 hrs. in UHV
10^{-8}	1.08	1.08
$5*10^{-8}$	1.22	1.20
10^{-7}	1.35	1.20

an intermediate value for the O/Pu^{ox} of 1.22. These films were re-analyzed after sitting in UHV for 12 hours. The resulting O^{2-}/Pu^{3-} stoichiometries were 1.08 for the 1×10^{-8} Torr exposure and 1.20 for both the 5×10^{-8} and 1×10^{-7} Torr exposures, as shown in Table 3.1, indicating continued oxygen diffusion into the near-surface region. All of these O/Pu values are significantly lower than the value that is expected for plutonium sesquioxide, Pu_2O_3 (Pu^{3+}; O/Pu = 1.5).

Temperature during oxygen exposure also influences the stoichiometry of plutonium oxide films. Auto-reduction occurs in vacuum at room temperature due to the diffusion of oxygen from PuO_2 through the sesquioxide film and subsequent reaction with Pu metal at the interface [9, 10] and can complicate the interpretation of XPS data collected from PuO_2 thin films. Low temperature stabilizes the PuO_2/Pu_2O_3 film on the metal surface by decreasing oxygen diffusion to a point where the film does not undergo auto-reduction. This allows for data collection from a film in which the composition (O/Pu concentration ratio and relative intensities of plutonium species) within the oxide film does not change with time. The XP spectra shown in Figure 3.3, demonstrate how temperature affects the auto-reduction of plutonium. The stable oxide film formed at less than -70^{o} C (blue spectra) does not undergo the auto-reduction reaction within the time in which XPS data were collected. In fact, thin PuO_2 films prepared during the course of this investigation have been observed to remain unchanged for several hours, so long as the temperature is maintained low enough to inhibit oxygen diffusion in the thin film. As the film is warmed, the auto-reduction reaction begins converting Pu^{4+} to Pu^{3+} at approximately -20^{o} C. Once the reaction is completed (red spectra), the oxide film is

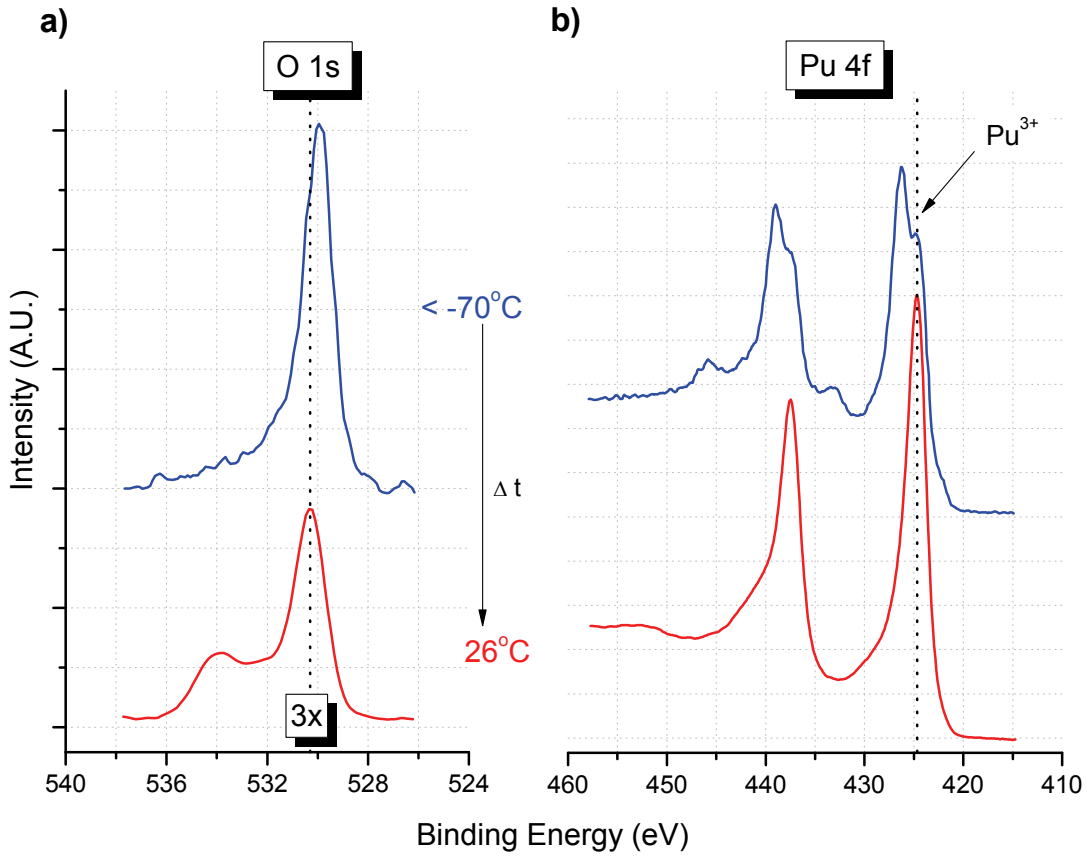

Figure 3.3: Plutonium oxide film formed at low temperature (< -70° C, blue spectra). As the temperature increases, Pu^{4+} is converted to Pu^{3+}. With time, equilibrium is reached (red spectra) at room temperature and the oxide film is 100% Pu^{3+}. The peak at ~534 eV in the O 1s spectrum of the film at 26° C is due to surface contaminants that accumulated on the surface of the oxide film as it warmed.

composed entirely of Pu^{3+}, as interpreted from the Pu 4f XP spectrum with signal at a binding energy of 424.4 eV. When the sample reaches a temperature of 26° C and the Pu 4f region indicates 100% Pu^{3+}, a peak at 534.0 eV appears in the O 1s XP spectra. This signal is likely an adsorbed surface-contaminant from residual gases in the system.

Figure 3.4 illustrates the effects of low, as well as high, temperature on the oxidation of plutonium. The exposure of Pu metal to 30 *L* of O_2 at different temperatures

results in oxide films of varying composition. An oxide film of Pu^{4+} & Pu^{3+} with an O/Pu stoichiometry of 1.8 forms at temperatures less than -70° C (blue spectra), representing results in oxide films of varying composition. An oxide film of Pu^{4+} & Pu^{3+} with an O/Pu stoichiometry of 1.8 forms at temperatures less than -100° C (blue spectra), representing an overlayer of PuO_2 with Pu_2O_3 beneath. At 75° C (red spectra), the same oxygen dose results in an oxide film composed 100% of Pu^{3+} and O/Pu ratio of 1.37. At 26° C (green spectra), the plutonium is mainly Pu^{3+} with a very small amount of metal observed,

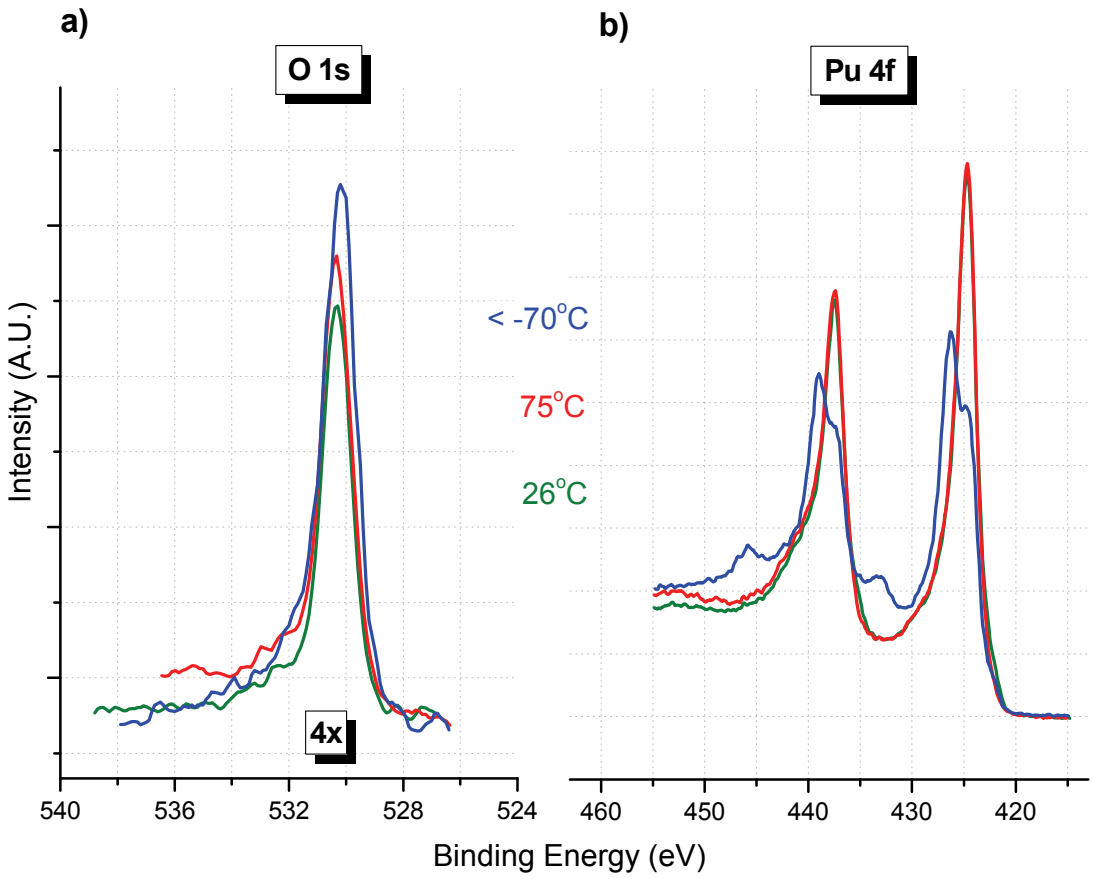

Figure 3.4: 30 *L* oxygen exposure at different temperatures. XP spectra from the **a)** O 1s and **b)** Pu 4f regions for three plutonium oxide films grown by exposure to 30 *L* of O_2 at < -70° C (blue), 75° C (red), and 26°C (green). All spectra are normalized to the Pu 4f area.

indicating a very thin oxide film. While the Pu 4f spectrum is identical to that of the film grown at 75°C, the O/Pu is only 1.3.

Figure 3.5 shows the XP spectra of a plutonium metal surface exposed to 30 *L* of O_2 (at 10^{-7} Torr) at two different temperatures. The red trace shows the XP spectra from an oxide film grown at 75° C with 30 *L* of O_2. The O/Pu^{ox} ratio is 1.37 and the corresponding Pu 4f region shows 100% Pu^{3+}. The black trace (as indicated in the figure) illustrates the O 1s and the Pu 4f XPS regions of an oxide film grown at < -70° C. The sample holder was cooled to -150° C, however, since plutonium produces heat due to radioactive decay, the temperature of the sample is not directly known, but has been modeled, as part of this thesis, to be < -70° C (a detailed description of the modeling can be found in the experimental chapter). The oxide film prepared at sub-ambient temperatures (< -70° C) was composed of a Pu^{4+}/Pu^{3+} ratio of approximately 1 with a small amount of Pu metal (6%) and an oxygen to oxidized plutonium ratio (O^{2-}/ Pu^{ox}) of 1.71. Also shown as the blue trace in Figure 3.4, is the resulting spectra from allowing the film obtained by a 30 *L* exposure at < -70 ° C (black trace, discussed above) to warm to room temperature and undergo auto-reduction. The Pu 4f spectrum now consists entirely of the Pu^{3+} species with no metal or Pu^{4+} observed. The corresponding O 1s spectrum yields an O/Pu concentration ratio for this film of 1.20. As seen in Figure 3.5, the Pu 4f spectrum for the film grown at 75° C (red) and for the sub-ambient film warmed to room temperature (blue) are identical, resembling what is expected for Pu_2O_3, yet the corresponding O 1s spectra show that they have different oxygen to plutonium stoichiometries.

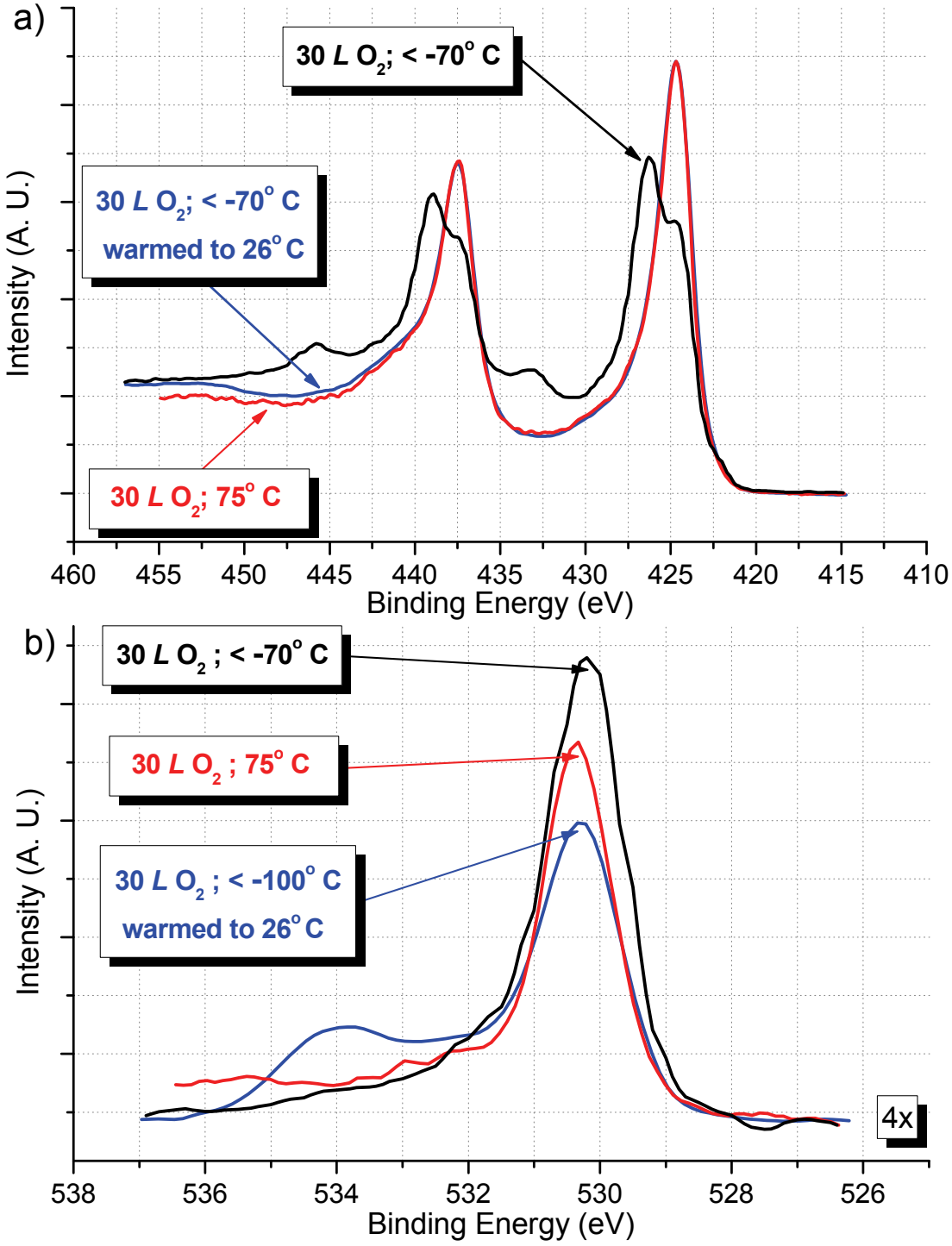

Figure 3.5: XP spectra from **a)** Pu 4f and **b)** O 1s regions for two plutonium oxide films grown by exposure to 30 *L* of O_2 at < -70° C (black trace) and at 75° C (red trace).Also shown in blue is the data obtained after allowing the cooled sample to warm to room temperature. All spectra are normalized to the Pu 4f area.

The existence of an oxide of plutonium lower in stoichiometry than the sesquioxide (Pu_2O_3) has previously been reported [11]. XRD studies of plutonium oxides on metal indicated the conversion of Pu_2O_3 upon heating (>250^o C) to a rocksalt structure historically interpreted as the monoxide (PuO). Subsequent investigations employing XPS concluded that the proposed conversion of Pu_2O_3 to PuO upon heating was likely due to the formation of plutonium oxycarbide ($PuO_{1-x}C_x$, x~ 0.3) [12]. The thin oxide films studied here were grown on clean plutonium surfaces at a variety of temperatures, all of which are significantly below the temperatures required for the formation of the oxycarbide. Analysis of the carbon 1s region of the XP spectrum shows no evidence of carbide (~282 eV) before or after oxygen exposure. In addition, the O/Pu for these thin films is significantly greater than what would be expected for $PuO_{1-x}C_x$.

3.2 Carbide within the Oxide Film

Figure 3.6 offers a comparison of the representative XP spectra for plutonium oxycarbide and two plutonium (Pu^{3+}) oxide thin films prepared from clean Pu metal surfaces as part of this investigation. The black spectra in Figure 3.6 were obtained after Ar^+-ion sputtering to remove surface carbon contamination of a Pu metal sample that had an oxy-carbide surface layer. While the exact nature of this film is not known, it clearly exhibits the presence of a carbide-type carbon at 282.6 eV. Quantification of the O 1s and C 1s data for this oxy-carbide film yield concentration ratios of O/Pu = 1.23 and C/Pu = 0.23. The absence of significant carbide peaks in the C 1s region for the higher stoichiometry sesquioxide film (O/Pu = 1.37, blue spectra) as well as the lower

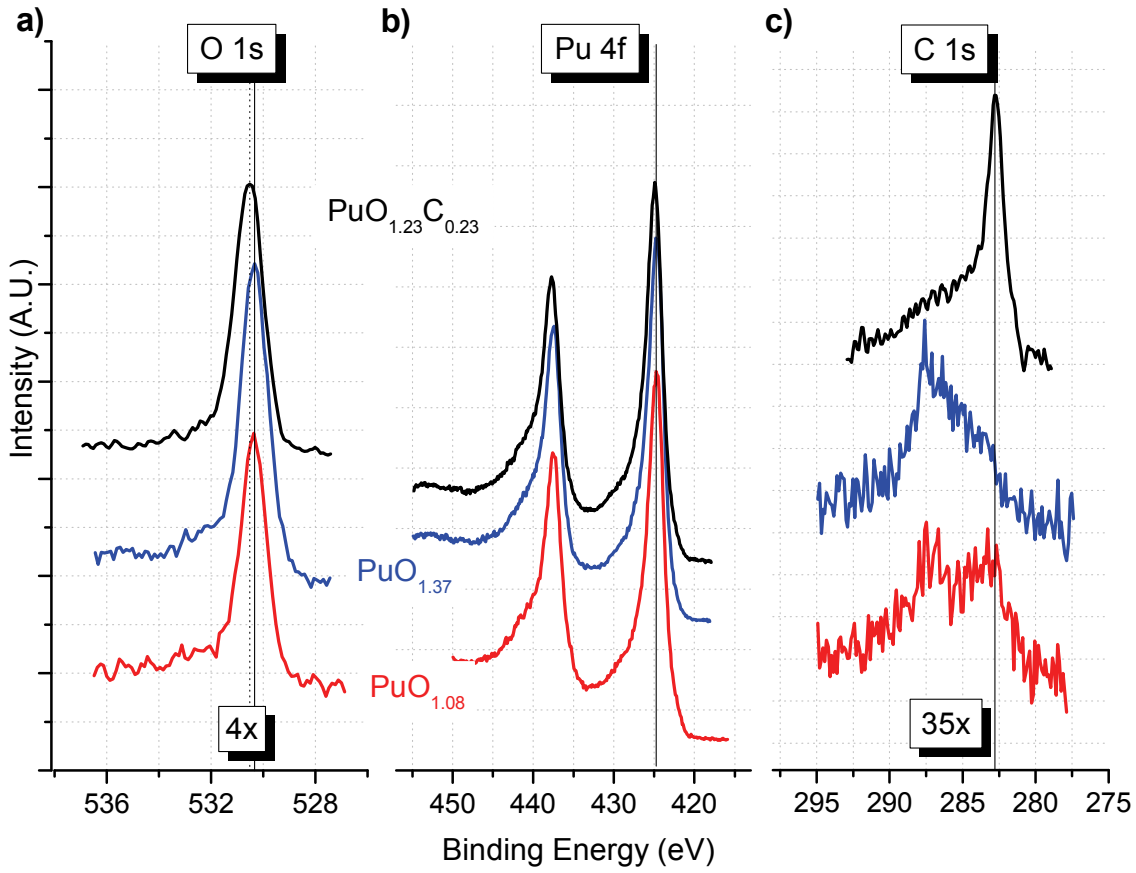

Figure 3.6: XP spectra from the **a)** O 1s, **b)** Pu 4f, and **c)** C 1s regions for a plutonium oxy-carbide film (black), and two different stoichiometry Pu_2O_{3-y} films.

stoichiometry film (O/Pu^{ox} = 1.08, red spectra) indicate that these films are relatively pure oxides. Thus, the presence of oxy-carbide as the reason for the low stoichiometry of these films (O/Pu < 1.5) can be ruled out. It needs to be noted however, that the C 1s XP spectra illustrated in Figure 3.6 overlaps in energy with the broad Pu $5p_{1/2}$ feature centered at ~284.2 eV [6], making detection of small amounts of carbon species difficult. Based on the low sensitivity for XPS detection of carbon and its spectral overlap, the limit of detection is estimated to be C/Pu ~ 0.1 atomic ratio in the oxide films.

3.3 Discussion

Another element has also been shown to exhibit uncommon and thermodynamically unstable bulk oxide phases at the surface of the metal. Unlike plutonium with its two stable bulk oxides (PuO_2 & Pu_2O_3), neptunium has only one stable bulk oxide (NpO_2, Np^{4+}). However, under a reducing environment (i.e., UHV) the sesquioxide of neptunium (Np_2O_3, Np^{3+}) has been shown to form at the surface of the metal exposed to oxygen gas as a very thin oxide film between the neptunium metal and thin oxide films that are nominally NpO_2 [13]. The set of plutonium data presented in this chapter clearly indicates that plutonium sesquioxide, under reducing environments, exhibit a wide range of stoichiometries. The ~100% Pu^{3+} spectrum in Figure 3.4 (red) shows the highest O/Pu atomic ratio (~1.4) observed for oxide-films, as measured by XPS, not containing significant quantities of the Pu^{4+} species. This value is not unreasonable, given the ability of films that are nominally Pu_2O_3 in oxygen content to support a range of sub-stoichiometric oxygen concentrations under UHV conditions, as shown here. Even if the relative sensitivity factor (RSF) used for quantification in this work is not correct, resulting in a low O/Pu value, all O/Pu ratios observed must be scaled accordingly. If it is assumed that the plutonium oxide film in Figure 3.2 (green trace) must represent stoichiometric Pu_2O_3 (i.e., O/Pu = 1.5), the corresponding adjustment of the Pu 4f RSF would still give low O/Pu ratios ranging from ~1.1-1.4 for all the oxide films presented of 100% Pu^{3+} in . This adjustment to the Pu 4f RSF would also give a concentration ratio for the film containing ~50% Pu^{4+} shown in Figure 3.4 and 3.5, of approximately 1.85 -higher than expected stoichiometry based on the Pu^{4+}/Pu^{3+} ratio.

Although the films shown here exhibit a large range of O/Pu stoichiometries, analysis of the Pu 4f region shows virtually identical spectra for the entire oxygen content range. This indicates that, while the formal oxidation state of the plutonium cations in Pu_2O_3 must be changing from predominantly 3+ to favor 2+, the electronic structure (as observed with XPS) is not changing significantly. In the absence of data to help elucidate differences in the crystallographic structure of the sub-stoichiometric plutonium oxide films, and the similarity of the Pu 4f XP spectra, they are tentatively described as Pu_2O_{3-y}, y~ 0.2-1 ($PuO_{1.4}$ – $PuO_{1.0}$).

An analogous behavior of the Pu 4f region has been observed in plutonium hydride [14]. The hydride compound exhibits a Pu 4f XP spectrum that is very similar to what is observed for Pu^{3+}. In fact, the plutonium cation in the hydride is considered to be trivalent (Pu^{3+}) with a ground state of $5f^5$ [15]. However, the hydride chemical formula is written as PuH_2. This oddity is normally explained as plutonium bonding to the hydrogens with two electrons while the third electron is donated to the conduction band. Given plutonium's 5f electrons ability to move into the conduction band, it is reasonable to expect the oxides of plutonium to exhibit varying stoichiometries as the extra electron not being used in bonding moves to the conduction band.

3.4 Conclusion

The present data indicates that a sub-stoichiometric plutonium oxide (Pu_2O_{3-y}) exists under reducing environments (i.e., UHV). Based on the high reactivity of plutonium towards oxygen, it is not unreasonable to expect this sub-stoichiometric

behavior to occur near the oxide-metal interface in plutonium oxide thin films. The level of contaminants, as tabulated in the experimental section of this thesis, of the plutonium employed for these experiments is extremely low for Pu which may allow for a greater degree of diffusion of oxygen into the sample. While shown to be stable in the bulk phase, films of plutonium sesquioxide that are nominally Pu_2O_3 in composition on clean plutonium metal show a significant level of stoichiometric instability under reducing conditions, perhaps similar to what has been shown for plutonium dioxide (PuO_2) films on plutonium metal.

References

[1] Gardner, E. R., Markin, T. L., and Street, R. S., *J. Inorg. Nuc. Chem.*, **27** (1965) 541.

[2] Schnizlein, J. G., and Fischer, D. F., *J. Electrochem. Soc.*, **114 (1)** (1967) 23.

[3] Raynor, J. B., and Sackman, J. F., *J. Nucl. Mater.*, **23** (1967) 302.

[4] Colmenares, C. A., *Prog. Solid St. Chem.*, **9** (1975) 139.

[5] Larson, D. T., *J. Vac. Sci. Technol.*, **17** (1980) 55.

[6] Baptist, R., Courteix, D., Chayrouse, J., and Heintz, L., *J. Phys. F:Met. Phys.*, **12** (1982) 2103.

[7] Stakebake, J. L., Larson, D. T., and Haschke, J. M., *J. Alloys Comp.*, **202** (1993) 251.

[8] Tull, S., 2003 *Ph.D.* Thesis, University of Wales, Cadiff, U.K.

[9] Morrall, P., Tull, S., Glascott, J., and Roussel, P., *J. Alloy. Compd.*, **444-445** (2007) 352.

[10] Haschke, J. M., Allen, J. C., and Martz, J., *J. Alloys Compd.*, **271** (1998) 211.

[11] Terada, K., Meisel, R. L., Dringman, M. R., *J. Nucl. Mater.*, **30** (1969) 340.

[12] Larson, D. T. and Haschke, J. M., *Inorg. Chem.*, **20** (1981) 1145.

[13] Naegele, J. R., *J. Nucl. Mater.*, **166** (1989) 59.

[14] Larson, D. T. and Motyl, K. M., *J. Electr. Spectr. Rel. Phenom.*, **50** (1990) 67.

[15] Willis, J. O., Ward, J. W., Smith, J. L., Kosiewicz, S. T., Haschke, J. M., and Hodges III, A. E., *Physica B*, **130** (1985) 527.

Chapter 4: AR Reaction of Plutonium Dioxide Films

The oxidation of plutonium metal has received considerable attention [1-3] due to its importance in the safe handling and storage of nuclear materials. Plutonium metal will spontaneously ignite at 475^{o} C, due to the highly exothermic nature of its reaction with oxygen [4]

$$Pu\ (s) + O_2\ (g) \rightarrow PuO_2\ (s) \quad \Delta H^o = -1056\ kJ/mol$$

Small metal particles, such as the metal shavings created from the machining and processing of the metal, ignite at 150^{o} C [5]. Because of the danger associated with its unpredictable nature, the pyrophoricity of plutonium is a pressing concern when establishing guidelines for different storage environments. Elucidation of the oxidation kinetics of plutonium metal is crucial for understanding the pyrophoricity of plutonium. In an attempt to investigate the process, Martz and co-workers have proposed a two step mechanism [6] to qualitatively explain pyrophoricity in which at higher temperatures: (1) the auto-reduction reaction (AR) of plutonium dioxide (PuO_2) to plutonium sesquioxide (Pu_2O_3 or $PuO_{1.5}$)

$$\tfrac{1}{2}\ Pu\ (s) + 3/2\ PuO_2\ (s) \rightarrow Pu_2O_3\ (s) \quad \Delta H^o = -73.5\ kJ/mol$$

depletes the PuO_2 layer to the point where (2) the reoxidation of Pu_2O_3 with air to PuO_2 occurs

$$\tfrac{1}{2}\ Pu_2O_3\ (s) + 1/4O_2\ (g) \rightarrow PuO_2\ (s) \quad \Delta H^o = -226\ kJ/mol$$

The heat generated from these two reactions further heats the sample which only speeds up the cycle, eventually resulting in pyrophoricity. While this mechanism qualitatively predicts the ignition temperature of plutonium, it is based on empirical data from thermogravimetric studies of bulk plutonium metal at high temperatures. Most of the assertions pertaining to the AR of PuO_2, both in an atmosphere of O_2 and in vacuum, are extrapolated from the bulk studies of Pu oxidation. While the AR of PuO_2 films to Pu_2O_3 has been noted in heated metal samples [7], cursorily mentioned at room temperature and at -196^o C [8], and utilized as a tool to ascertain the oxygen diffusion coefficient through the Pu oxide [9], there has not been any published reports detailing the conditions and parameters necessary for the AR of plutonium dioxide to occur. The following investigation of the AR of PuO_2 is aimed at understanding the factors affecting this peculiar attribute of Pu oxidation, as well as an attempt to qualify the validity of the published conjectures regarding it.

4.1 Current Understanding of the PuO_2 AR Reaction

Figure 4.1 illustrates a model of plutonium metal surface oxidation and subsequent AR reaction to Pu_2O_3 after removal of oxygen from the headspace, based on the current knowledge available in the literature [7, 9-11]. Upon exposure to oxygen, a Pu metal surface quickly oxidizes to Pu^{3+} which is then further oxidized to Pu^{4+}. With time, the oxide film is typically described as consisting of a thin Pu_2O_3 film between Pu metal and a thick PuO_2 film. [1]. Once PuO_2 is exposed to a reducing atmosphere, such as UHV, it quickly reduces to Pu_2O_3 as the oxygen diffuses through the Pu_2O_3 layer to react

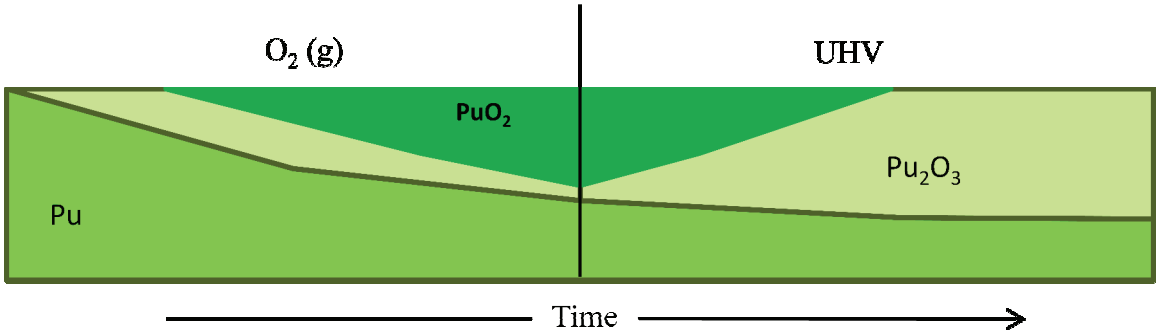

Figure 4.1: Notional diagram of the oxidation of Pu metal and subsequent AR reaction of plutonium dioxide. PuO_2 and Pu_2O_3 layers form on the metal surface when exposed to O_2. When the oxygen is removed, PuO_2 is converted to Pu_2O_3.

with Pu metal at the metal-oxide interface. As was the case for the proposed mechanism regarding the pyrophoricity of Pu, the experimental data supporting this model, however, was for the most part extrapolated from gravimetric measurements at elevated temperatures, where the sample weight gains occur sufficiently rapid to be measured in a reasonable amount of time [12].

4.2 In-situ XPS of Pu Metal Oxidation at Room Temperature

Because the oxidation and AR of PuO_2 are dynamic processes, it would be advantageous to observe the evolution of the oxidation state of plutonium from metal to Pu^{3+} and Pu^{4+} oxidation and back to Pu^{3+} (the AR reaction), as a function of oxygen/UHV exposure. To that end, a clean plutonium surface was exposed to oxygen while being monitored by XPS. While the oxygen pressures that can be probed in-situ with XPS without permanently disabling the instrument used in the present study are relatively low, e.g., 10^{-8} and $5*10^{-8}$ Torr, valuable information can be obtained regarding the initial

stages of Pu oxidation. Figure 4.2 illustrates the in-situ analysis of a Pu metal surface as it is exposed to 10^{-8} Torr O_2. The Pu 4f XP spectrum was fitted with the components, as described previously in chapter 2 of this thesis. Upon oxygen exposure, the Pu metal (green trace) is converted to Pu^{3+} (red trace). At the end of the exposure (30.5 *L*), the Pu 4f signal is composed of 85% Pu^{3+} and 15% Pu metal, which corresponds to an oxide

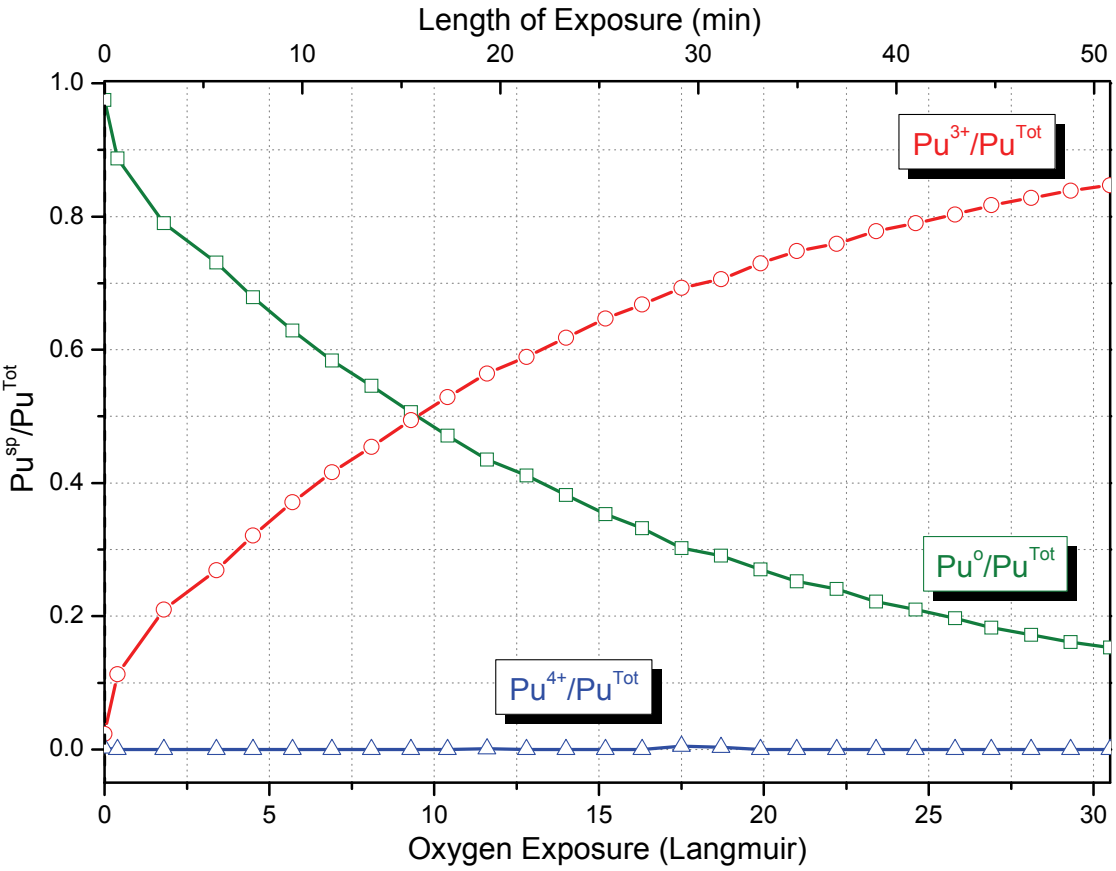

Figure 4.2: In-situ XPS analysis of a Pu metal surface exposed to 10^{-8} Torr O_2 for ~51 min (30.5 *L*) at 27° C. The XPS Pu 4f peaks were fitted to extract the Pu metal (green), Pu^{3+} (red), and Pu^{4+} (blue) species from the signal envelope. The data is plotted as a ratio of the Pu species (Pu^{sp}) to the total Pu 4f signal area (Pu^{Tot}). The lower abscissa is plotted in units of Langmuir (10^{-6} Torr*sec); the top is in minutes of oxygen exposure. A Pu 4f spectrum was acquired every ~2 minutes. No discernable amount of Pu^{4+} was observed. Oxygen exposure began at the end of the acquisition of the first XP spectrum (time and exposure = 0)

film thickness of approximately 43 Å [13]. Towards the end of the 30.5 *L* exposure the rate of growth of the Pu^{3+} has decreased and the presence of Pu^{4+} is not detected. It cannot be ruled out from this experiment, however, whether a Pu^{4+} oxide film would form with longer exposures to oxygen.

Figure 4.3 illustrates a second in-situ XPS experiment in which the Pu metal

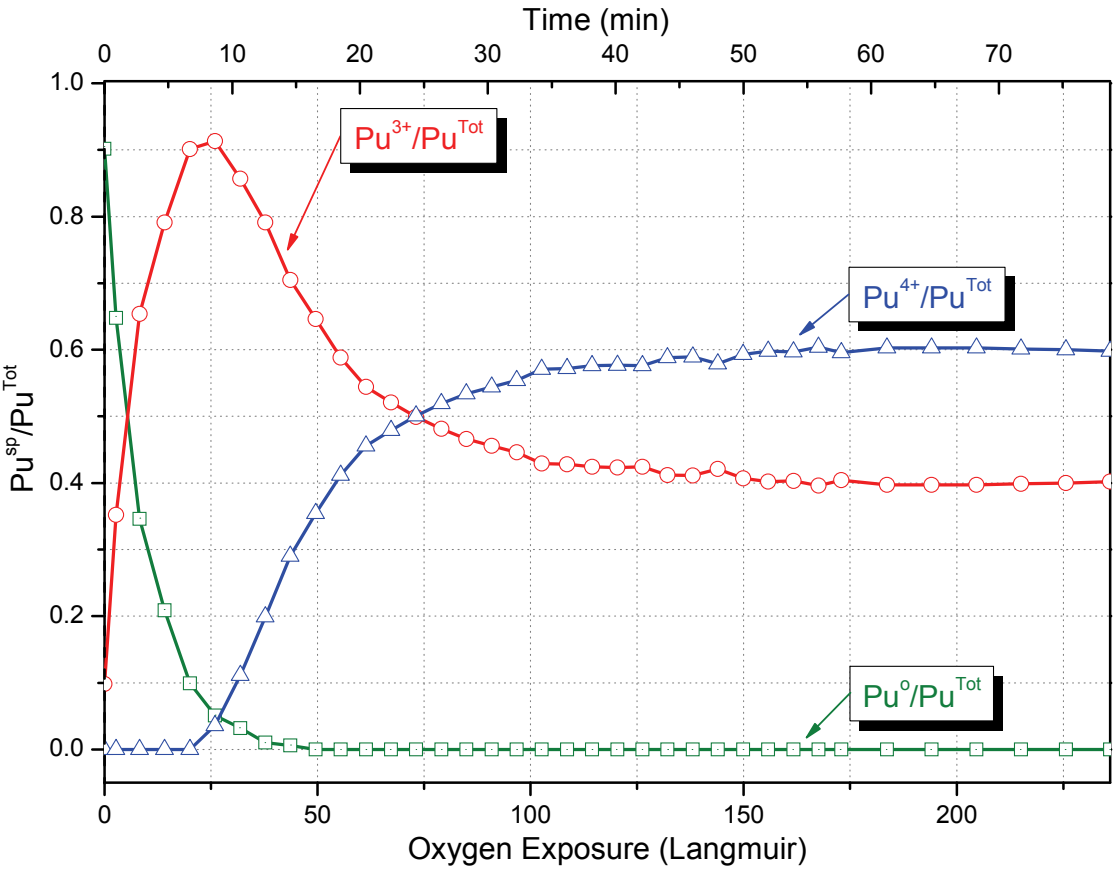

Figure 4.3: In-situ XPS analysis of a Pu metal surface exposed to $5*10^{-8}$ Torr O_2 for ~79 min (236 *L*) at 28° C. The XPS Pu 4f peaks were fitted to extract the Pu metal (green), Pu^{3+} (red), and Pu^{4+} (blue) species from the signal envelope. The data is plotted as a ratio of the Pu species (Pu^{sp}) to the total Pu 4f signal area (Pu^{Tot}). The lower abscissa is plotted in units of Langmuir (10^{-6} Torr*sec); the top is in minutes of oxygen exposure. A Pu 4f spectrum was acquired every ~2 minutes. Oxygen exposure began at the end of the acquisition of the first XP spectrum (time and exposure = 0).

surface is exposed to $5*10^{-8}$ Torr of O_2. At this pressure, the evolution and composition of the oxide film is dramatically different to the oxygen exposure presented in Figure 4.2. Upon exposure to oxygen, the metal surface quickly oxidizes to Pu^{3+}, reaching a maximum at 25 *L*. At this point PuO_2 (Pu^{4+}) begins growing, as the Pu^{3+} signal decreases. The Pu^{4+} intensity reaches a maximum after 150 *L* of O_2 and remains constant until the exposure ends at 236 *L*. Figure 4.4 shows a representative XP Pu 4f spectrum acquired

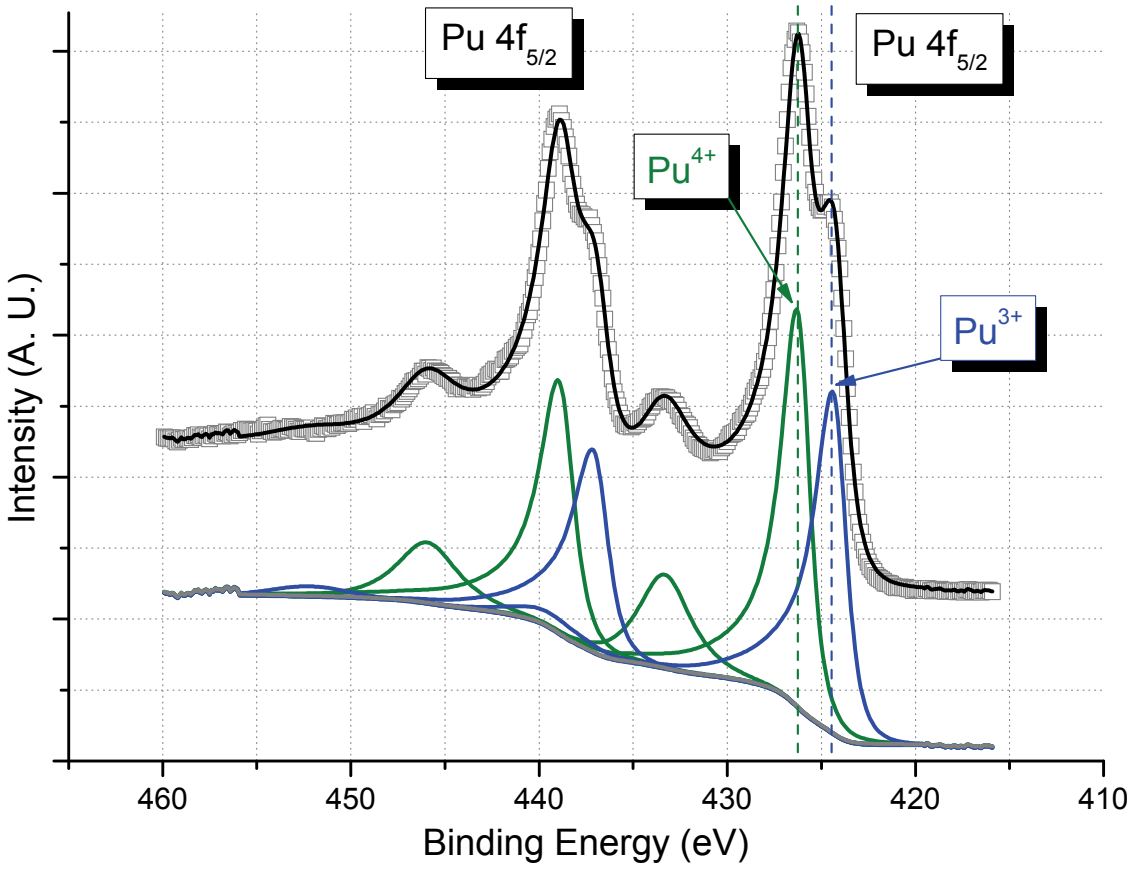

Figure 4.4: Typical XP Pu 4f spectrum (grey squares) of the Pu oxide film acquired during the final stage of the oxygen exposure (> 150 *L*) presented in Figure 4.3. The spectrum shown is the average of the last four spectra acquired (205-236 *L*). The data fit (black trace) is the sum of the Shirley background (gray trace), the Pu^{4+} (green traces) and the Pu^{3+} (blue traces) synthetic peaks.

during this exposure interval. The Pu 4f signal is 60% Pu^{4+} and 40% Pu^{3+} indicating a 15 Å thick PuO_2 film [13]. At the binding energies being monitored during this experiment, approximately 425 eV (electron kinetic energy of 1062 eV), the probing depth of XPS is 54 Å. Thus, only the uppermost 39 Å of the sesquioxide can be probed. Even though the PuO_2 film has clearly stopped growing during the oxygen exposure presented in Figure 4.3, the sesquioxide beneath the PuO_2 most likely continues to grow as oxygen diffuses to the metal-oxide interface.

Acquisition of the O 1s as well as the Pu 4f XP spectral regions allows for the determination of the stoichiometry (O^{2-}/Pu^{Tot}) of an oxide film. Figure 4.5 shows the stoichiometry of the Pu oxide film grown during the in-situ experiment presented in Figure 4.3 as well as the subsequent AR of PuO_2. Near the end of the $5*10^{-8}$ Torr O_2 exposure, the stoichiometry was determined to be 1.81. This number agrees well with the expected stoichiometry (1.80) obtained from the Pu 4f component ratio of Pu^{4+}:Pu^{3+} (0.60/0.40), assuming O/Pu = 2 for Pu^{4+} and O/Pu = 1.5 for Pu^{3+}. Once the $5*10^{-8}$ Torr O_2 atmosphere above the plutonium sample is removed, shown in the second part of Figure 4.5, the 15 Å film of PuO_2 immediately begins thinning as oxygen diffuses to the metal-oxide interface. The oxide film is close to 100% Pu^{3+} after 600 min with O^{2-}/Pu^{Tot} = 1.43. The swift auto reduction of the PuO_2 film after the oxygen exposure is completed indicates that while the PuO_2 film remained at a constant thickness during the exposure, oxygen is diffusing to the metal-oxide interface where the Pu_2O_3 continues to grow during the exposure.

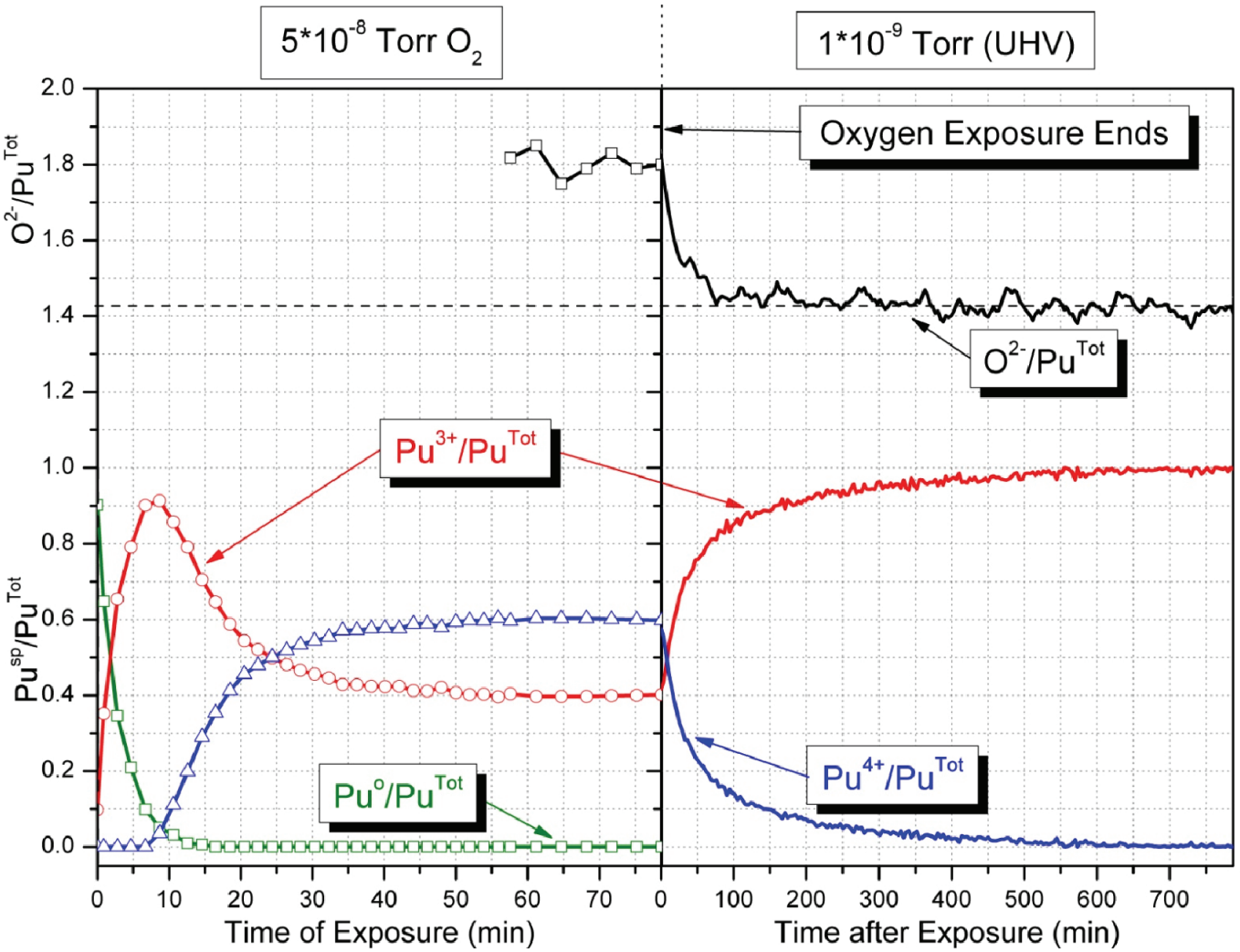

Figure 4.5: In-situ XPS analysis of a Pu metal surface during a 236 *L* O_2 exposure ($5*10^{-8}$ Torr/78.7 min) at 28° C and subsequent AR of PuO_2. Immediately after closing the oxygen gas leak valve, the instrument pressure drops to ~$1*10^{-9}$ Torr, and the AR of PuO_2 ensues.

4.3 Effect of Temperature on the AR of PuO_2

At room temperature, the AR of PuO_2 consumes the dioxide film in a matter of hours. The same process only takes a few minutes at 70° C [14]. It stands to reason that at

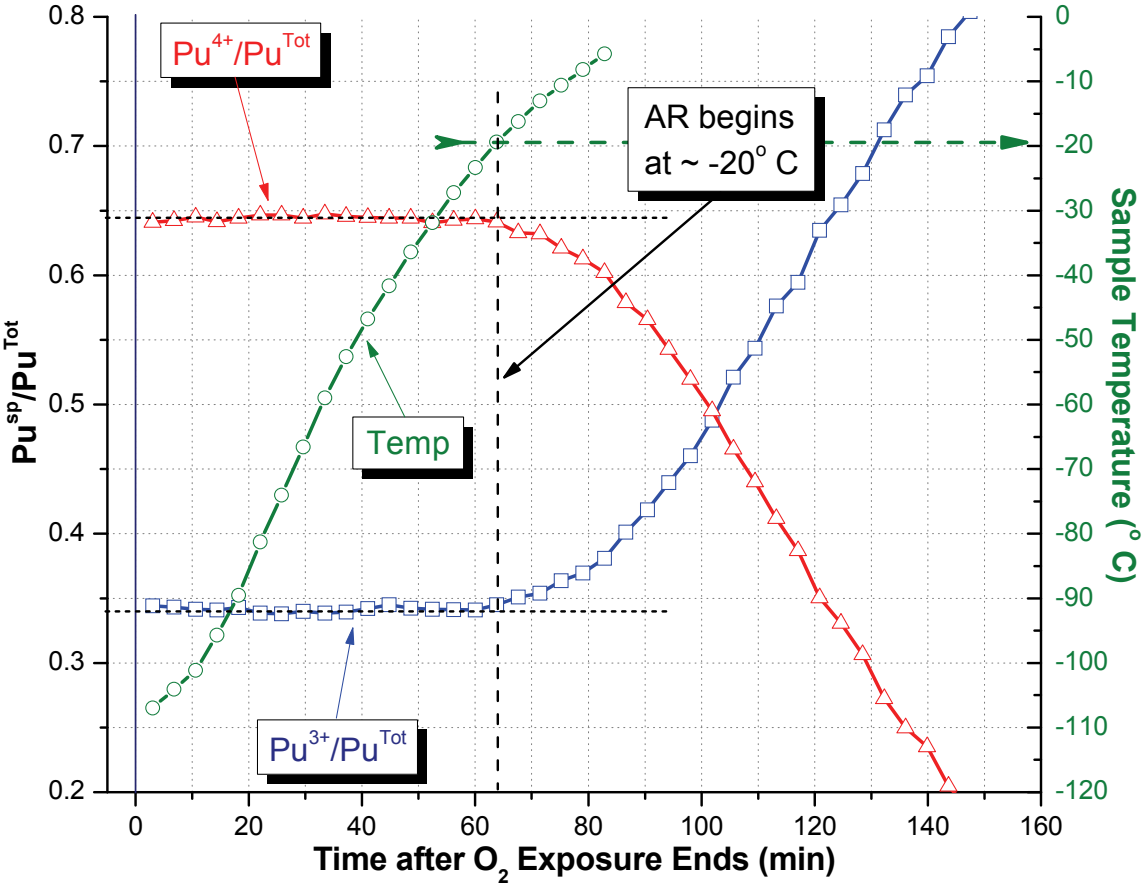

Figure 4.6: XPS Pu 4f region analysis as a function of temperature and time of an oxide film, grown by exposing a Pu metal surface at a temperature of < -70° C to 590 *L* O_2. The XPS Pu 4f indicates the film to be ~65% Pu^{4+} (red trace, open triangles) and ~35% Pu^{3+} (blue trace, open squares). The left ordinate corresponds to the Pu species (Pu^{sp}) to total Pu 4f signal (Pu^{Tot}) area ratio; the right ordinate corresponds to the sample temperature (green trace, open circles). The Pu species' ratio start changing 64 minutes after the exposure ended indicating the beginning of the AR, at a temperature of approximately -20° C (horizontal green arrow). [1]

[1] Temperatures lower than -70° C, such as those in Figure 4.6, are stated simply as < -70° C throughout this thesis. See experimental section for details.

lower temperatures, the AR may slow down enough to render a PuO_2 film on metal substrate stable, at least within the timescales of an XPS experiment. Figure 4.6 shows the behavior of an oxide film grown on a Pu metal surface at a temperature of < -70° C. As the sample temperature slowly increases, the Pu species concentration ratio (Pu^{4+}, Pu^{3+}/Pu^{Tot}) remains constant, indicating a stable oxide film. 64 min after the end of the O_2 exposure (vertical dashed line), the AR begins when the temperature reaches

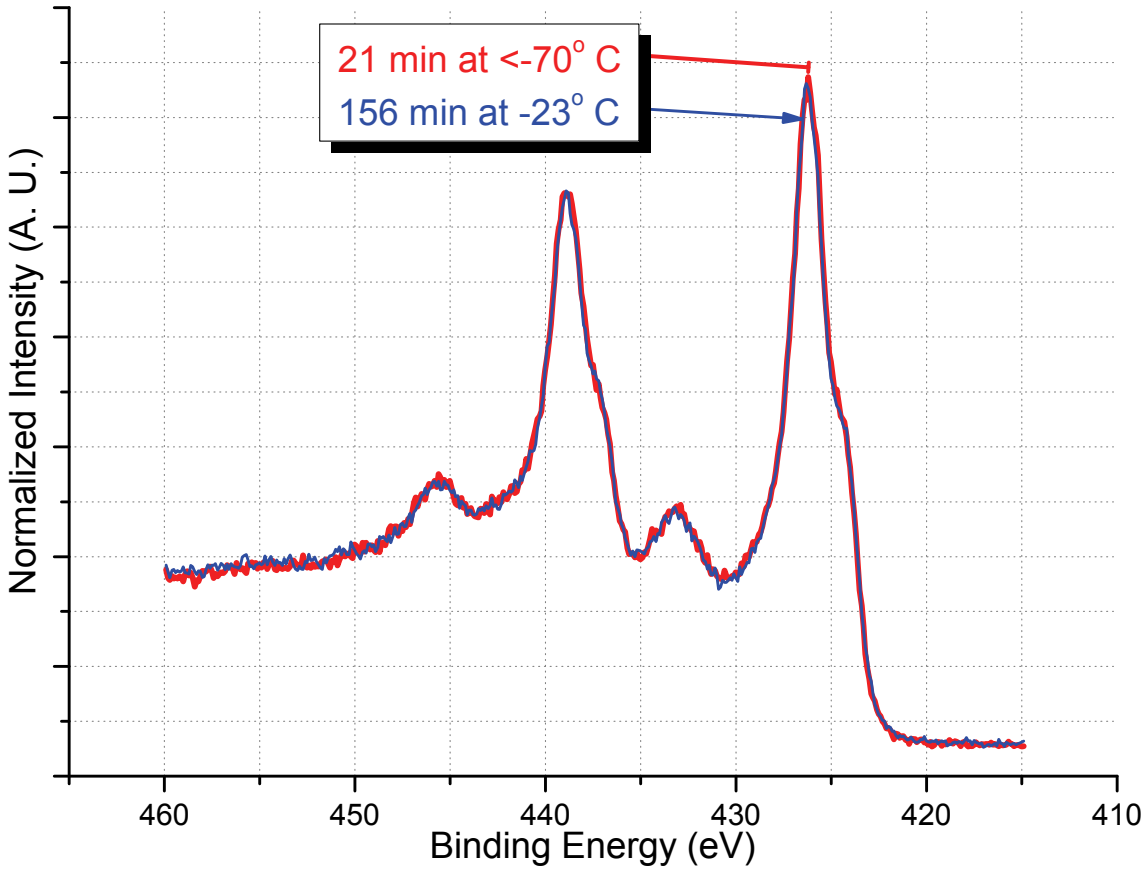

Figure 4.7: XPS Pu 4f spectra of an oxide film grown by 249 *L* O_2 exposure while cooling the metal sample. The first spectrum (red trace) was acquired 21 min after the end of the exposure at a temperature of < -70° C. The oxide film was continually analyzed while the temperature slowly increased. 156 min after exposure (blue trace), the temperature had reached -23° C; the film composition remained stable.

approximately -20^{o} C.

During this particular experiment, the PuO_2 remained stable for 64 minutes. Temperature rather than time, however, is the critical factor in PuO_2 film stability. As long as the sample temperature remains below -20^{o} C, the AR is not observed. Figure 4.7 shows two XP spectra of a different experiment where a Pu oxide film was grown by exposing Pu metal to 249 *L* O_2 while cooling from 26^{o} C to < -70^{o} C. The initial Pu 4f spectrum acquired (red trace) at < -70^{o} C shows an oxide film composed of ~70% Pu^{4+} and ~30% Pu^{3+}. This is equivalent to a ~ 20 Å thick PuO_2 film atop the sesquioxide [13]. XPS analysis continued while the sample temperature slowly increased, in order to determine the stability of the film. After 156 min, the temperature had reached -23^{o} C; the Pu 4f spectrum (blue trace) remained unchanged, indicating a stable oxide film. Shortly afterwards, while the temperature increased further, the film composition began changing as the PuO_2 decreased in thickness.

4.4 Effect of Temperature on the Growth of Pu Oxide Films

It has been established that the AR of PuO_2 ceases at temperatures below -20^{o} C. This implies that below this temperature, classical diffusion of oxygen through the oxide film does not occur. Oxidation of Pu metal, however, does occur at low temperatures. Figure 4.8 shows a 380 *L* O_2 exposure of a Pu metal surface at a temperature of < -70^{o} C (green trace). This film, grown at a low temperature, has a composition of 63% Pu^{4+}, 34 % Pu^{3+} and a very small signal (< 2%) of what could be interpreted as metal. These

numbers correspond to a PuO_2 film of ~17 Å thick [13]. A second oxygen exposure of 249 *L* O_2 is shown in Figure 4.8 (red trace). In this case, the exposure began at 28° C and continued while the sample was cooled to < -70° C. The composition of this film was determined to be 69.8 % Pu^{4+} and 30.2 % Pu^{3+} which is equivalent to an approximately 19 Å thick PuO_2. Dosing the sample while cooling produced the thicker film (~19 Å vs. ~17 Å) even though the oxygen dose was smaller (249 *L* vs. 380 *L*). This is not surprising

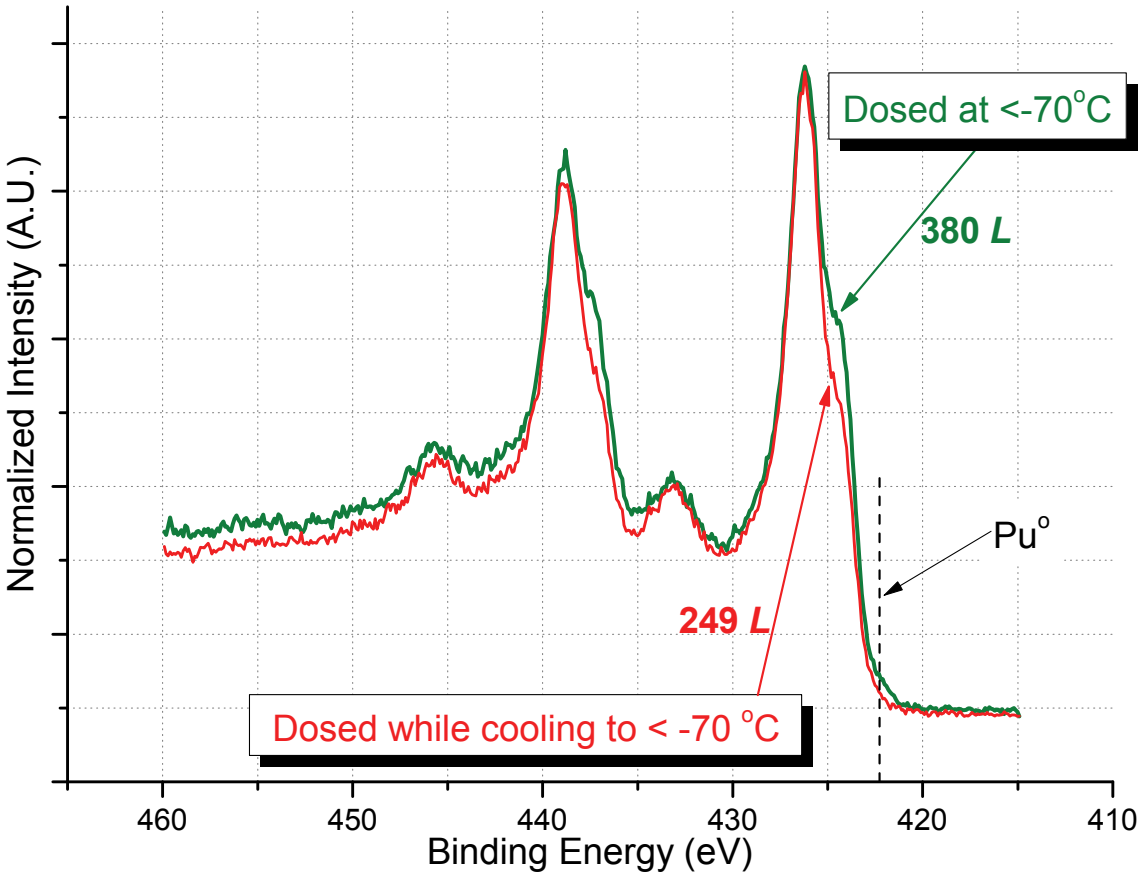

Figure 4.8: XP Pu 4f spectra of oxide films prepared under different temperature conditions. A pressure of $1*10^{-7}$ Torr was employed for both films. The green trace denotes an oxide film formed by a 380 *L* O_2 exposure to a Pu metal sample at a temperature of < -70° C. The red trace represents a film formed by exposing Pu metal to 249 *L* at 28° C and continuing the exposure while the sample cooled to < -70° C. The dashed vertical line at 422.2 eV indicates the binding energy of the Pu metal $4f_{7/2}$ signal.

since the exposure that began at 28^{o} C allows for thicker films as oxygen readily diffuses through the oxide –until the temperature reaches ~ -20^{o} C. At this point, oxygen diffusion ceases. As long as the temperature is maintained below -20^{o} C, the oxide film remains stable facilitating XPS analysis of PuO_2 film composition.

The question remains: How can oxidation of Pu occur, as evidenced by the experiment shown in Figure 4.8 at a temperature where it has been established, diffusion of oxygen does not occur? A possible explanation for this phenomenon is that there is more than one type of diffusion mechanism. Classical diffusion, as described by Wagner's parabolic law [15, 16], is driven by the chemical potential gradient established across the oxide by the oxygen anions on the oxide-gas interface and the metal cations at the metal-oxide interface. Since the chemical potential of any process is temperature dependent, Wagner Law's diffusion is temperature dependent. Not all diffusion mechanisms, however, depend on temperature. The Mott-Cabrera (M-C) model [17] of diffusion describes the growth behavior of thin films that do not follow a parabolic rate growth; the kinetic growth behavior follows an inverse-logarithmic growth expression. In this case, diffusion of oxygen is driven by the electrostatic gradient established across the oxide. The rate limiting step for this process is the tunneling of electrons across the oxide. Consequently, this type of diffusion is temperature independent, below a critical temperature. The probability of electron tunneling through a barrier decreases exponentially and practically drops to zero at ~20 Å. Thus, the M-C model normally applies to thin, protective oxides such as those formed on tantalum and aluminum metal. The PuO_2 films presented in Figure 4.8 reached a thickness of only 18 Å. Indeed, all the

PuO_2 oxides presented here exhibit thicknesses no greater than 20 Å. This seems to indicate that whether at room temperatures (in-situ experiments) or at temperatures below -20^o C, the growth of PuO_2 films on metal may be governed by factors other than chemical potential gradients (Wagner's law).

4.5 Thick PuO_2 films

As was mentioned, the oxide films prepared during this investigation consist of very thin PuO_2 films (< 20 Å). The low exposure pressures employed could be the reason for the inability to produce thicker PuO_2 films. XPS analysis, due to the reasons discussed previously, is not conducive for "high" pressure (> 5*10^{-8} Torr) experiments. However, the knowledge of the cessation of diffusion at temperatures below -20^o C can be used to grow oxide films that can be analyzed by XPS, as was shown in Figure 4.8 (red trace). Figure 4.9 illustrates three oxide films grown under different conditions. The green spectrum is representative of the film grown in the room temperature in-situ experiment presented in Figure 4.3. The other two oxide films were grown by exposing the Pu metal sample to oxygen while cooling in order to effectively "freeze" the film as it is during room temperature oxidation and thus permit XPS analysis. The thicknesses for the three films are presented in Table 4.1. The 249 *L* O_2 exposure at 10^{-7} Torr (blue trace) produced a ~19 Å PuO_2 film while the larger dose of 20,000 *L* O_2 at 10^{-5} Torr (red trace) yielded a PuO_2 film of ~20 Å. However, visual inspection of the XP Pu 4f spectra (blue and red trace) corresponding to these two oxygen exposures (249 *L* and 20,000 *L,* respectively)

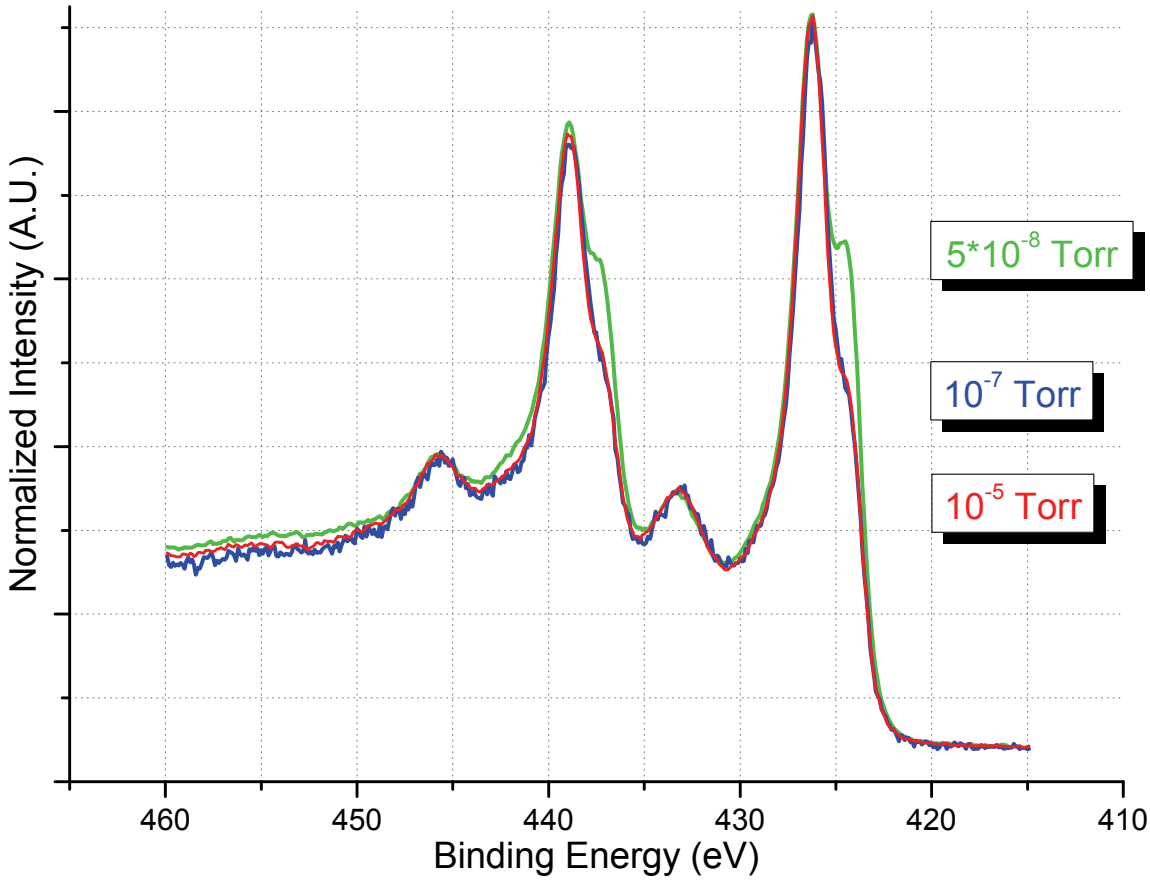

Figure 4.9: Comparison of XPS Pu 4f spectra of three oxide films grown under different conditions. The green spectrum represents the room temperature in-situ experiment at $5*10^{-8}$ Torr (236 *L*), the blue spectrum corresponds to a film grown at 10^{-7} Torr (249 *L*) while cooling. The red spectrum is of a film grown at 10^{-5} Torr (20,000 *L*) while cooling the sample to < -70° C. The process of cooling the metal sample while exposing it oxygen effectively stops the diffusion of oxygen through the oxide film "freezing" the film and allowing for XPS analysis after the exposure ends.

Table 4.1: Overview of thicknesses calculated from the XPS spectra presented in Figure 4.9.

Pressure (Torr)	**Exposure (Langmuir)**	**Pu^{3+}/Pu^{Tot}**	**Pu^{4+}/Pu^{Tot}**	**PuO_2 Thickness (Å)**
$5*10^{-8}$	236	40.8 %	59.2 %	14.9
10^{-7}	249	32.3%	67.6 %	18.9
10^{-5}	20,000	30.8 %	69.2%	19.8

makes it evident that these two films are essential identical in thickness with very little difference in the relative intensities of the Pu species. These PuO_2 films are representative of the thickest dioxides prepared during the course of the experiments presented in this work.

A larger oxygen exposure experiment was performed in the preliminary stages of this investigation. A Pu metal surface was exposed to 10^{-4} Torr O_2 for 90 min at 27° C (540,000 *L*). A significant amount of time (~15 min) elapsed between the end of the exposure and the start of the XPS analysis while the instrument's operating pressure was reached. XPS analysis showed an oxide film composed primarily of Pu^{3+} as the AR had consumed most of the PuO_2 indicating that the film grown was not much thicker than the oxide films presented here.

4.6 Nature of the Pu Oxide System

There are three possible Pu oxide models that may be considered: 1) a mixed valence (Pu^{3+}/Pu^{4+}) oxide film on top of the sesquioxide, 2) PuO_2 and Pu_2O_3 islands (according to the XPS analysis the composition would be 60-70% PuO_2 and 40-30 % Pu_2O_3), and 3) a thin PuO_2 film on a Pu_2O_3. The oxygen-plutonium phase diagram has been extensively studied [18, 19]. There is no evidence that a mixed valence Pu oxide exists. The in-situ experiment presented in Figure 4.5 shows a kinetic growth process were Pu_2O_3 acts as an intermediate for the formation of PuO_2:

$$Pu^0 \rightarrow Pu_2O_3 \rightarrow PuO_2$$

PuO_2 forms only after the metal, within the probing depth of the technique, has been oxidized to Pu^{3+}. An island growth mechanism would be expected to show simultaneous growth of both Pu_2O_3 and PuO_2:

$$Pu^0 \rightarrow Pu_2O_3 + PuO_2$$

Additionally, the ratio of Pu^{3+}:Pu^{4+} would be expected to exhibit greater variation for an

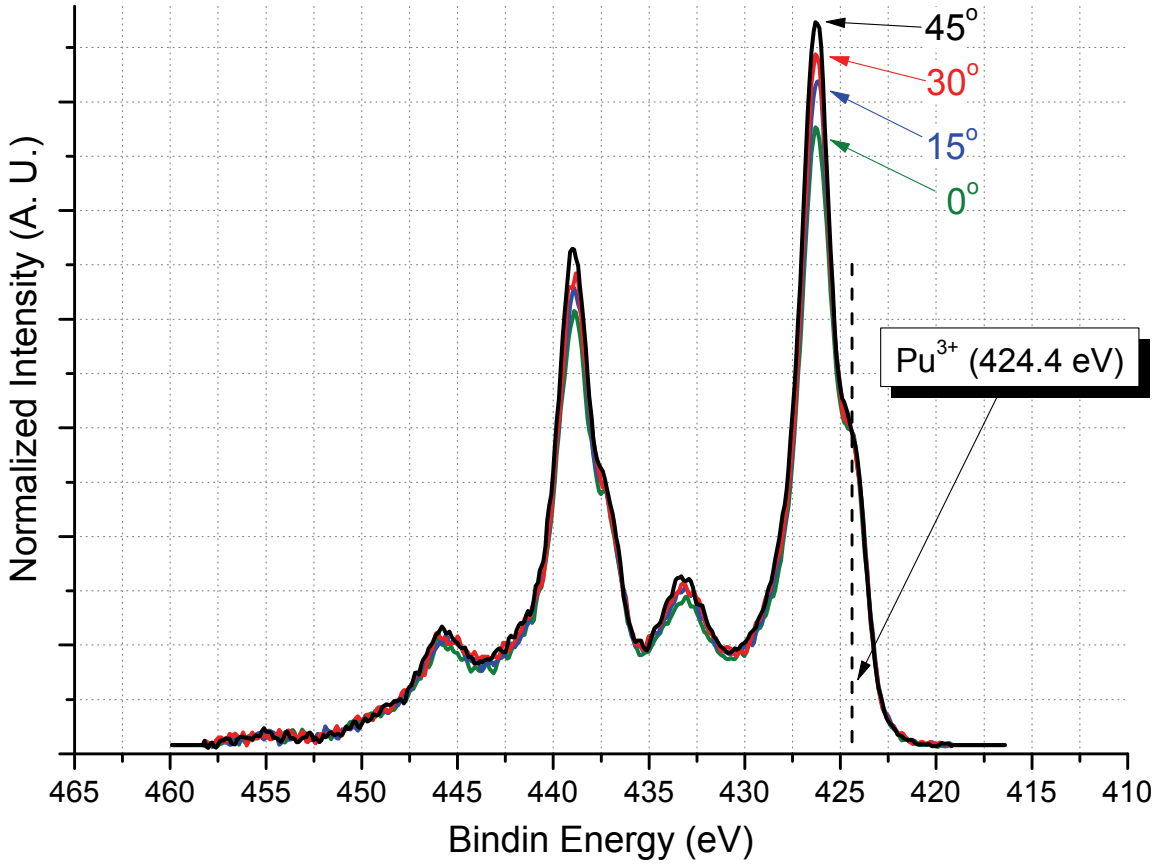

Figure 4.10: Angle dependent XPS experiment of a Pu oxide film maintained at < -70° C. The spectra have been normalized to the Pu^{3+} signal at a binding energy of 424.4 eV. The angle listed is between the sample surface and the electron analyzer. (0° represents the sample surface normal to the analyzer). The intensity of the Pu^{4+} (426.0 eV) increases (relative to Pu^{3+}) with increasing angle indicating that the PuO_2 film is on the Pu^{3+} oxide film. The Shirley background has been subtracted from these spectra for clarity.

island oxide system [20]. The oxides prepared for this investigation exhibit little variation of Pu^{3+}:Pu^{4+} for large ranges of temperature, pressure and exposure (time) preparation conditions.

Results from an angle dependent XPS (AD-XPS) experiment performed on Pu oxide films are presented in Figure 4.10. At large angles of analysis, the signal from the outer-most layer is enhanced at the expense of the signal from the layer beneath as the probing depth of the technique decreases. The data shows that with increasing angle, the signal corresponding to the Pu^{4+} increases, relative to the signal from Pu^{3+}. Thus, the only model consistent with the data presented here and previous studies is a PuO_2 thin film at the oxide-gas interface.

4.7 Conclusions

The AR has been shown to cease converting PuO_2 to Pu_2O_3 at temperatures below

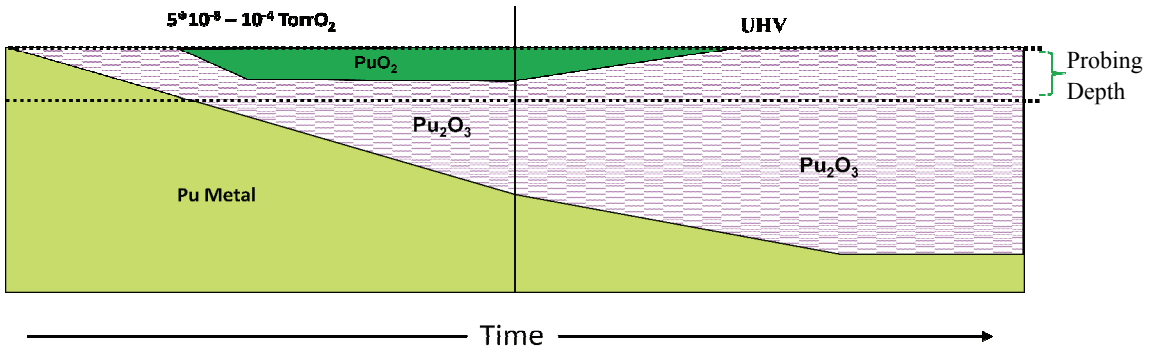

Figure 4.11: Notional diagram of the AR reaction of plutonium dioxide incorporating the results from this investigation. Upon oxygen exposure, a thin PuO_2 layer (< 20 Å) forms at the oxide-gas interface. A thicker Pu_2O_3 layer form on the metal-oxide interface. When the oxygen is removed, PuO_2 is converted to Pu_2O_3 by the AR of PuO_2.

-20^{o} C. This finding contradicts previously published reports [8] which state that the AR was observed at 77 K (-196^{o} C!). The report did not describe how the temperature was measured. It is likely that the sample temperature was reported as that of LN_2 without actual temperature measurement.

At the beginning of this chapter, Figure 4.1 was presented to illustrate the state of knowledge of plutonium oxidation. Figure 4.11 incorporates the results presented in this chapter regarding the oxidation behavior and oxide composition. The most noticeable difference between the two diagrams is that the PuO_2 film formed is unexpectedly thinner than previously thought. The plutonium oxide film system consists of a thin PuO_2 on a thicker Pu_2O_3 film. Within the oxygen pressures investigated (up to 10^{-4} Torr), the PuO_2 film thickness observed do not exceed ~20 Å, similar to the thickness expected for Mott-Cabrera oxide growth, where electron transport is the rate limiting step. XPS analysis of Pu oxide films grown during O_2 exposure and cooled below -20^{o} C before the exposure ends, permits the determination of the stoichiometry of oxide without the effects of the AR of PuO_2. The newly found knowledge of the behavior of PuO_2 films AR, will facilitate the study of thin Pu oxide film composition and stoichiometry.

References

[1] Haschke, J. M., Allen, T. H., Morales, L. A., *Los Alamos Science*, **26** (2000) 252.

[2] Haire, R. G., Haschke, J. M., *MRS Bulletin*, Sep 2001, 689.

[3] Colmenares, C. A., *Prog. Solid State Chem.*, **15** (1984) 257.

[4] Morss, L. R., in The Chemistry of the Actinide Elements, Vol. 2, Katz, J. J., Seaborg, G. T., Morss, L. R., eds., 2nd edition, (Chapman and Hall, New York:1986) chap. 17.

[5] Stakebake, J. L., Rocky Flats Report, RFP-4517, 1992.

[6] Martz, J. C., Haschke, J. M., Stakebake, J. L., *J. Nucl. Mater.*, **210** (1994) 130.

[7] Larson, D. T., *J. Vac. Sci. Technol.*, **17** (1980) 55.

[8] Almeida, T., Cox, L. E., Ward, J. W., and Naegele, J. R., *Surface Science*, **287-288** (1993) 141.

[9] Morrall, P., Tull, S., Glascott, J., Roussel, P., *J. Alloy. Compd.*, **444-445** (2007) 352.

[10] Veal, B. W., Lam, D. J., Diamond, H., Hoekstra, H. R., *Phys Rev. B*, **15** (1977) 2929.

[11] Seibert, A., Gouder, T., Huber, F., *Radiochim. Acta*, **97** (2009) 247.

[12] Stakebake, J. L., Larson, D. T., Haschke, J. M., *J. Alloys Comp.*, **202** (1993) 251.

[13] *ARCtick Angle Resolved XPS Spreadsheet*, National Physical Laboratory, Ver. 1.0, March 1999.

[14] Dr. P. Roussel, *A. W. E.*, private communication.

[15] Wagner, C., *Z. Phys. Chem.*, **21**(1933) 25.

[16] Wagner, C., *Z. Phys. Chem.*, **32B** (1936) 447.

[17] Cabrera, N., Mott, N. F., *Rep.Prog. Phys*., **12** (1948) 163.

[18] Chikalla, T. D., McNeilly, C. E., and Skavdahl, R. E., *J. Nucl. Mater.*, **12** (1964) 131.

[19] Boivineau, J. C., *J. Nucl. Mater.*, **60** (1976) 31.

[20] Hauffe, K., Oxidation of Metals, (Plenum Press, New York:1965).

Chapter 5: Composition of Oxide Films on Pu Metal Surfaces

As was pointed out in the introduction, plutonium metal readily oxidizes in air to form a layered oxide system composed of plutonium dioxide (PuO_2) at the air-oxide interface and a plutonium sesquioxide (Pu_2O_3) at the oxide–metal interface [1-4]. Figure 5.1 illustrates how, at room temperature and in an inert environment such as an ultra high vacuum (UHV) system, PuO_2 undergoes a spontaneous, thermodynamically driven auto-reduction (AR) reaction where Pu_2O_3 grows at the expense of the dioxide [5, 6].

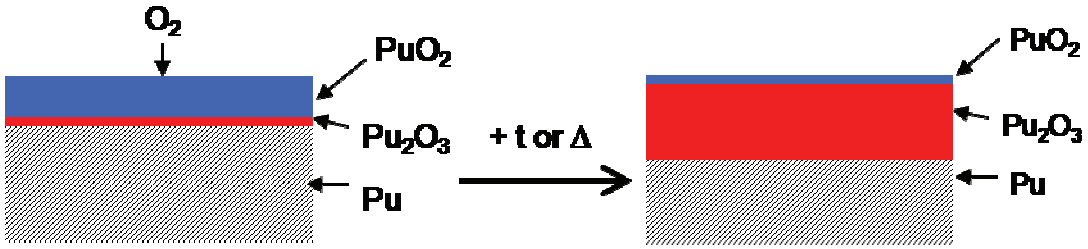

Figure 5.1: Change in the plutonium oxide on the metal surface when exposed to reducing environment (UHV).

Given enough time in this environment, the dioxide will be completely converted to the sesquioxide, as shown in Figure 5.2. The potential usefulness of the AR reaction as a tool to study the oxidation of plutonium has been previously demonstrated [7]. By analyzing the rate of dioxide to sesquioxide conversion, a coefficient of diffusion for oxygen through the sesquioxide was estimated. This previous study relied on the detection of the Pu^{3+} (Pu_2O_3) and Pu^{4+} (PuO_2) cations, as observed with x-ray photoelectron spectroscopy (XPS).

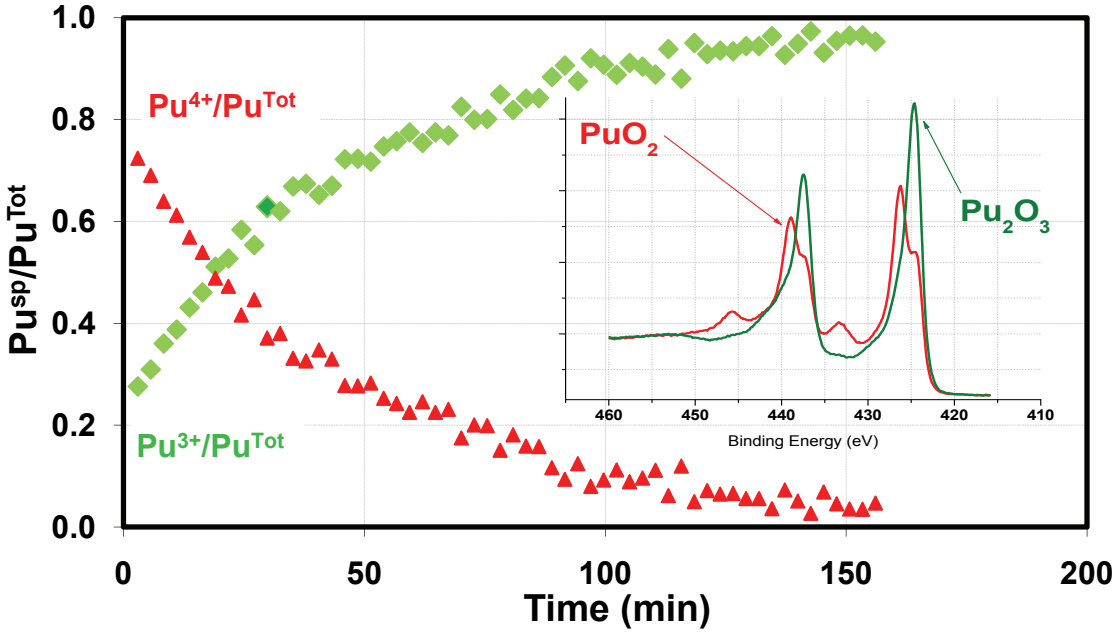

Figure 5.2: Typical behavior of the auto-reduction reaction of PuO_2. Pu^{4+} (red triangles) decreases with time as the Pu^{3+} (green diamonds) increases. The inset shows the initial XP spectrum (red) with a mix of Pu^{4+} & Pu^{3+} as well as the XP spectrum (green line) from the end of the plot, around 150 minutes. The red spectrum was acquired immediately after oxygen exposure of a clean Pu metal surface. The green spectrum was acquires after the AR had run its course, converting Pu^{4+} to Pu^{3+}

There is no information on the nature of the oxide and how its stoichiometry is affected by the auto-reduction of PuO_2. Generally, it is assumed that the only stable oxides of plutonium at room temperature are the dioxide and sesquioxide, even for thin oxide films on metal substrates. As was demonstrated in the previous chapter, very thin plutonium sesquioxide films under reducing environments support considerable sub-stoichiometry (Pu_2O_{3-y}; y= 0 to 1). It is unclear what role, if any, Pu_2O_{3-y} plays in the oxidation/AR of plutonium. To that end, the AR of plutonium oxide films, both from a dioxide to sesquioxide conversion, as well as an O/Pu stoichiometry perspective will be discussed in this chapter.

5.1 AR of Plutonium Dioxide on Clean Surfaces

Figure 5.3 shows the change with time, under UHV (<5*10^{-9} Torr), of a plutonium oxide film prepared by exposing a clean plutonium metal surface to a 540 *L* dose of oxygen. There is a small time delay of approximately 3 minutes between the removal of the oxygen from the chamber and powering on the Al Kα x-ray source before data acquisition begins. At the beginning of the acquisition, plutonium dioxide is

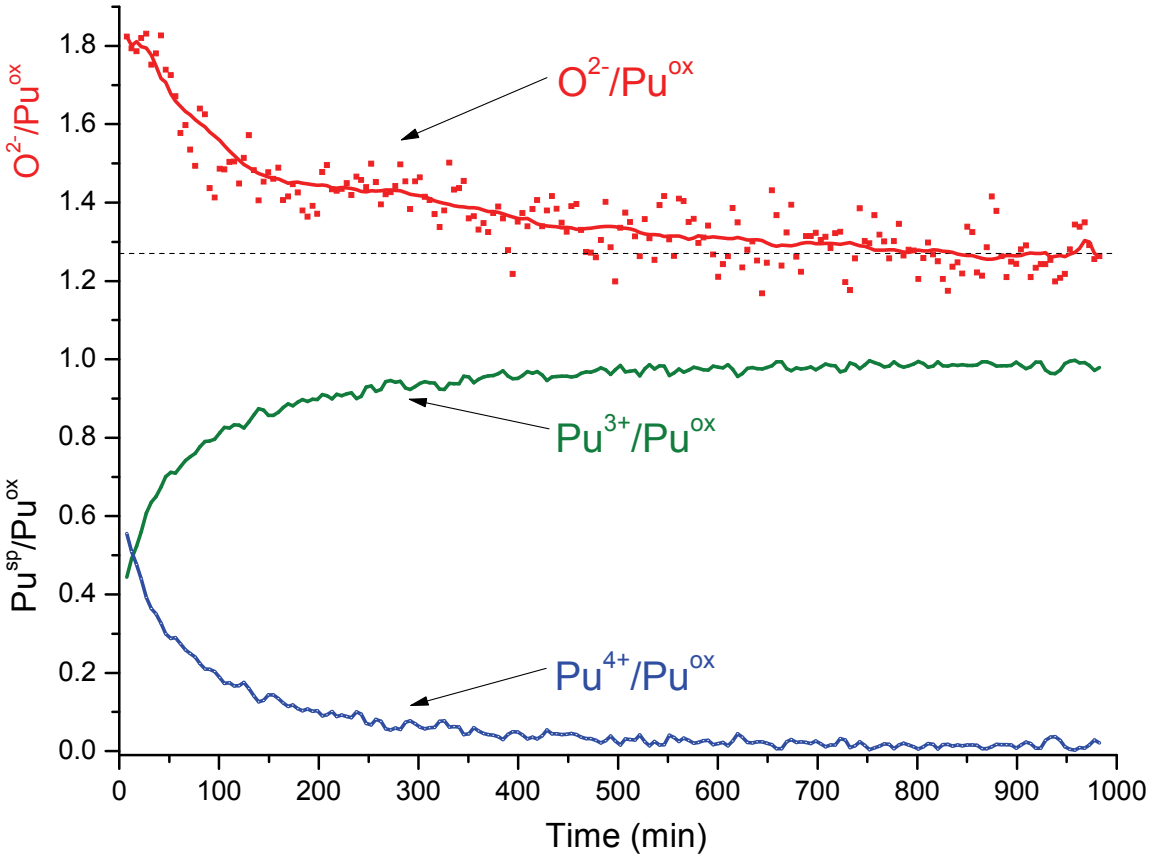

Figure 5.3: Auto-reduction (AR) reaction of plutonium dioxide film on clean plutonium metal. Data acquisition began four minutes after 540 *L* oxygen exposure. As the AR reaction proceeds, the Pu^{4+}(blue):Pu^{3+}(green) ratio changes from 0.55:0.45 to 100% Pu^{3+}. The O^{2-}/Pu^{ox} stoichiometry (red) decreases from 1.8 to 1.27 (dashed line), less than what is expected for plutonium sesquioxide (Pu_2O_3; O^{2-}/Pu^{ox} = 1.5). The red line represents a 10-point Savitzky-Golay fit to the O^{2-}/Pu^{ox} data (red squares).

observed auto-reducing. Peak fitting of the Pu 4f XP spectra yields the amount of Pu^{4+} and Pu^{3+} relative to the total amount of oxidized plutonium (Pu^{ox} = Pu^{3+} + Pu^{4+}). Pu^{4+}/Pu^{ox} decreases, with time, as Pu^{3+}/Pu^{ox} increases. Simultaneous acquisition of the oxygen 1s photoelectron spectra allows for monitoring the changes in the stoichiometry of the oxide film throughout the duration of the auto-reduction of PuO_2 (Pu^{4+}) until the end, when only the sesquioxide (Pu^{3+}) is present. Initially, the plutonium oxide film has a composition of approximately 0.55:0.45 Pu^{4+}:Pu^{3+} with an oxygen stoichiometry (O^{2-}/Pu^{ox}) of 1.81, close to the 1.78 expected value calculated from the ratio of plutonium 4+ and 3+ cations for the dioxide and sesquioxide. At the end of the AR reaction, the oxide film is essentially all Pu^{3+} with a stoichiometry (O^{2-}/Pu^{ox}) of 1.27, significantly less than what is expected for a plutonium sesquioxide film (Pu_2O_3; O^{2-}/Pu^{ox} = 1.5).

AR reaction of two thin-film plutonium oxide samples grown from ~30 *L* oxygen doses as observed with XPS and AES are displayed in Figures 5.4 and 5.5, respectively. The AR of a plutonium oxide film formed after a 33 *L* oxygen exposure is shown in Figure 5.4, as observed via AES. Although AES does not allow for differentiating between the oxidation state of the plutonium cation species (4+ vs. 3+), it allows data acquisition before, during, and after the oxygen exposure through a greater range of oxygen dosing pressures than is normally feasible with XPS. As the surface is exposed to oxygen, the stoichiometry (O/Pu) rises sharply, peaking at 1.55. As soon as the 33 *L* oxygen dose is completed and the oxygen is removed from the system, the O/Pu^{ox} rapidly decreases to a final ratio of ~1.13 after 1,000 minutes, again lower than what is expected

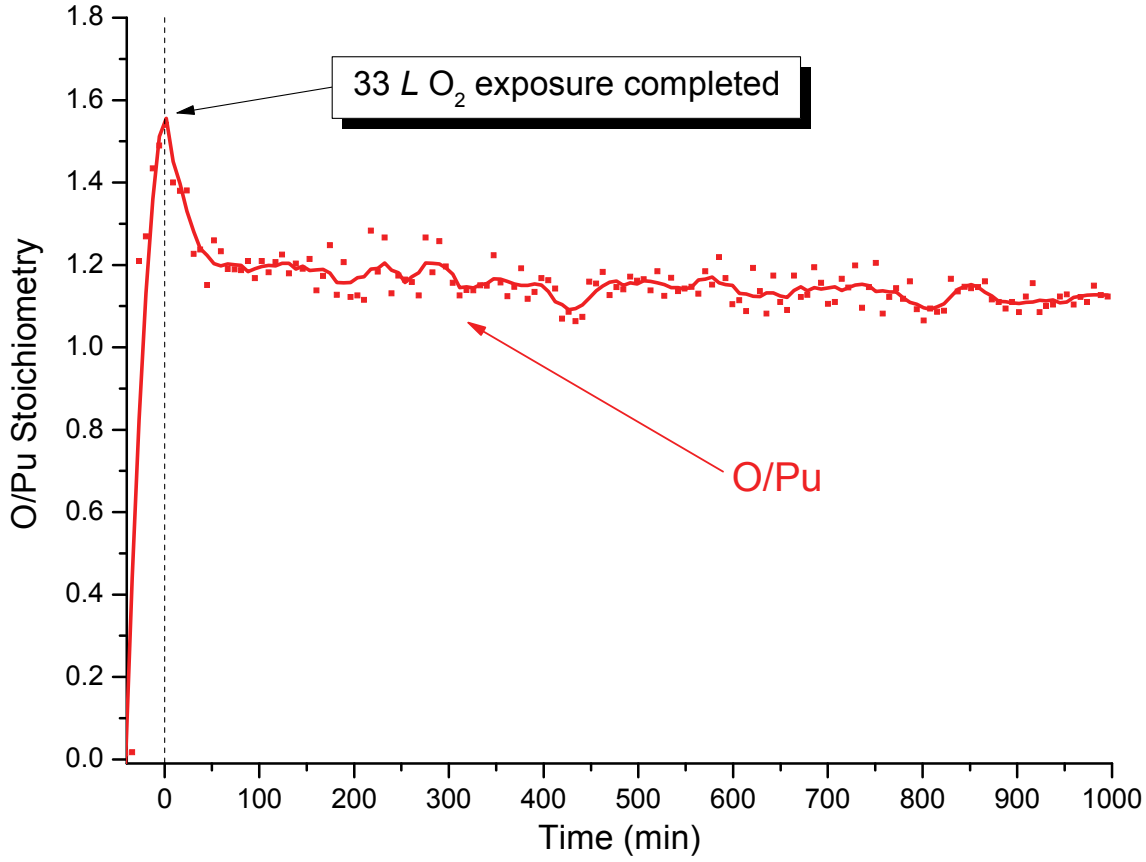

Figure 5.4: AES data plot of AR reaction of a thin oxide film on clean plutonium metal prepared with 33 *L* exposure of oxygen. The red line represents a 10-point Savitzky-Golay fit to the data (red squares).

for Pu_2O_3. A similar oxygen exposure and subsequent AR experiment was performed and monitored with XPS. Figure 5.5 shows a 30 *L* oxygen dose of a plutonium metal surface. Initially, the Pu 4f spectra acquired after the exposure show a small amount (~5%) of Pu^{4+} and ~ 90% of the plutonium species in the 3+ state; the stoichiometry (O^{2-}/Pu^{ox}) of this film is ~1.35. Plutonium metal (Pu^{o}) from the underlying substrate makes up the remaining 5% of the Pu 4f spectra, indicating the thin nature of the oxide film produced from the relatively small oxygen dose. After 600 minutes, all the plutonium is in the 3+

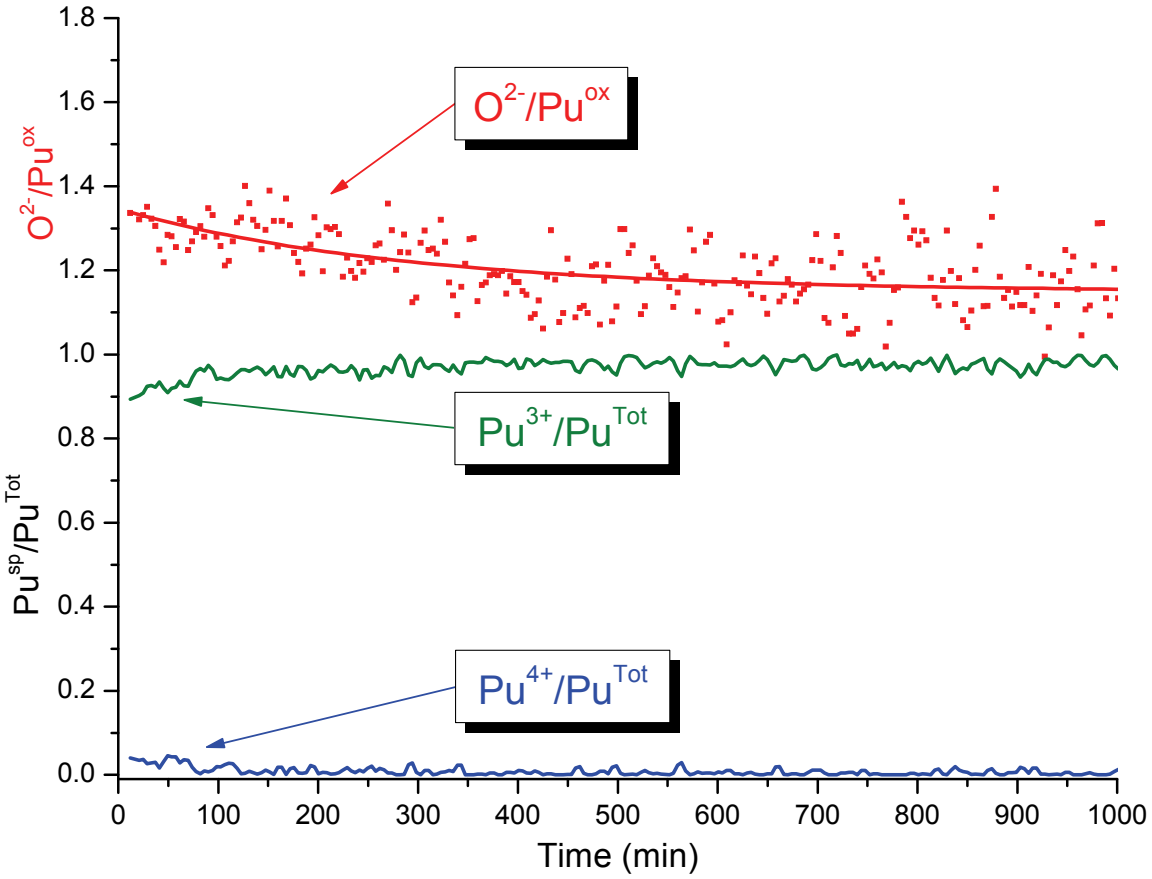

Figure 5.5: XPS data plot of AR reaction of a thin oxide film on clean plutonium metal prepared with 30 *L* exposure of oxygen.

oxidation state and the final stoichiometry (O^{2-}/Pu^{ox}) of this oxide film is ~1.16, very similar to what was observed with AES and shown in Figure 5.4. These two experiments seem to indicate that like PuO_2 films, very thin Pu_2O_3 oxide films are unstable under reducing environments (UHV) and will auto reduce to form oxide films with O/Pu stoichiometries as low as 1.1-1.2.

5.2 AR of PuO_2 on Carbide-Contaminated Surfaces

Due to the strong reactivity of plutonium [8], it is often difficult to prepare clean plutonium surfaces. Impurities of oxygen and carbon, in the form of oxycarbide and/or carbide, are frequently observed. The XP spectra at the top of Figure 5.6 (red trace) are characteristic of the cleanest surfaces prepared for this thesis. Small but detectable amounts of oxide are observed along with a small amount of residual carbide, that when quantified give $Pu(O_{0.02})(C_{0.03})$. The oxide films presented earlier in this chapter in

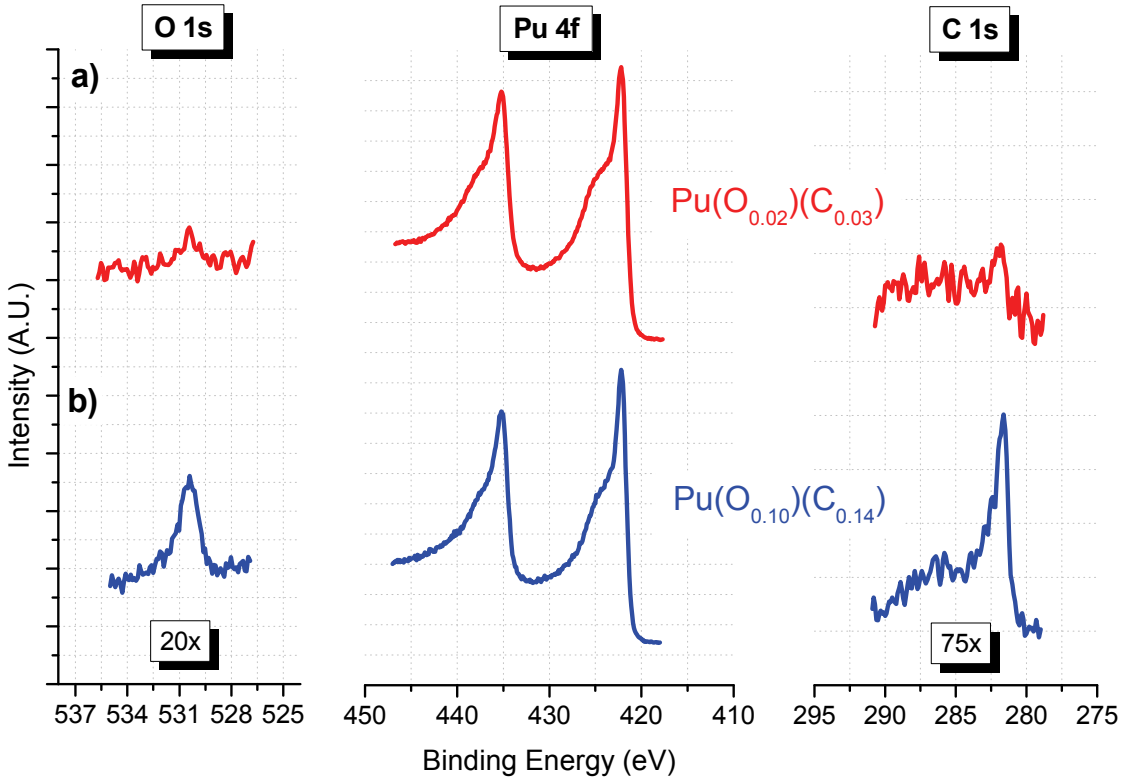

Figure 5.6: Representative XPS spectra for **a)** clean plutonium metal $[Pu(O_{0.02})(C_{0.03})]$ (top in red) and **b)** carbide-contaminated metal $[Pu(O_{0.10})(C_{0.14})]$ (bottom in blue) surfaces: O 1s (left), Pu 4f (center), and C 1s (right) spectra regions. The spectra are normalized to their respective Pu 4f area.

Figures 5.3, 5.4, and 5.5 were grown on surfaces with contamination levels similar to this. The bottom spectra (blue trace) in Figure 5.6 illustrate a more typical carbide-contaminated Pu surface [$Pu(O_{0.10})(C_{0.14})$] with a C 1s binding energy of 281.6 eV, characteristic of carbidic carbon [9]. The oxide films shown in Figures 5.7-5.9 and discussed below were grown on surfaces with these higher oxide/carbide contamination levels, typical of most plutonium samples.

Figure 5.7 illustrates an oxide film grown after exposing a carbide-contaminated Pu surface to a 235 *L* dose of oxygen. Analysis of this surface with XPS began towards

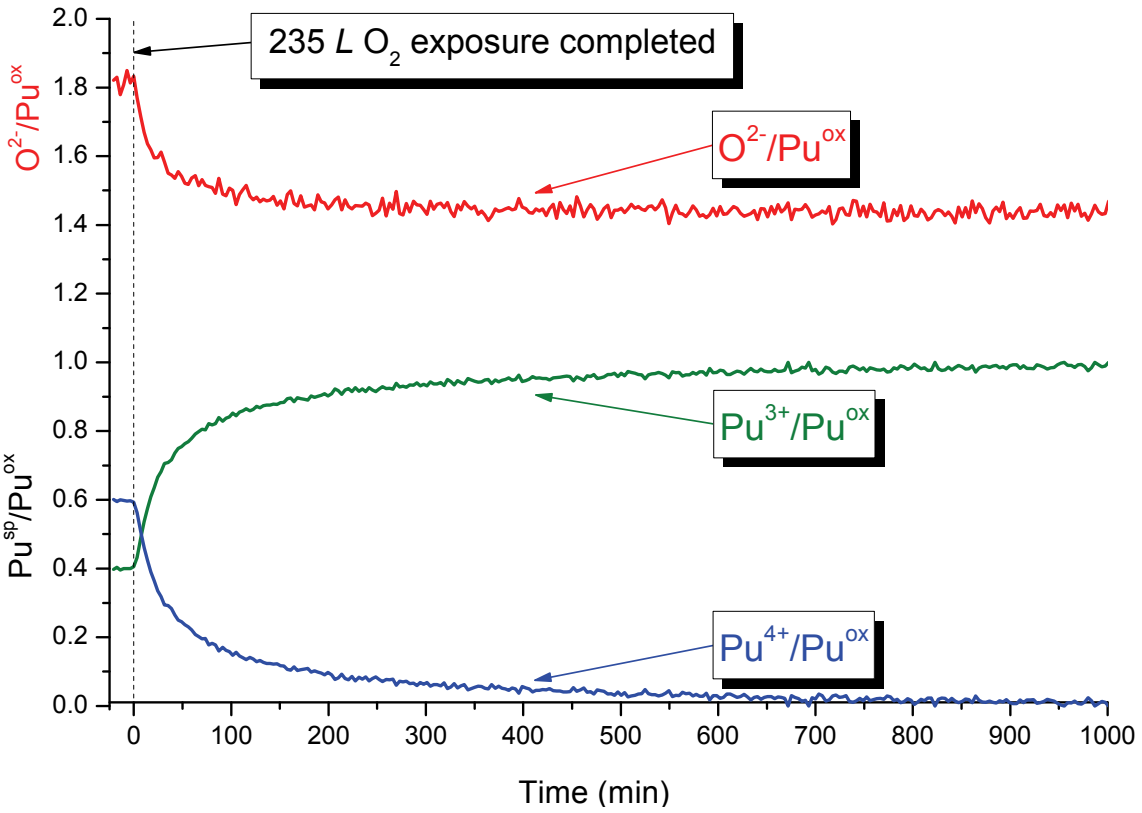

Figure 5.7: Auto-reduction (AR) reaction of plutonium dioxide film grown on carbide-contaminated: 235 *L* exposure at 28° C.

the end of the oxygen dose. The data shows a plutonium oxide film with a composition of approximately 0.60:0.40 Pu^{4+}:Pu^{3+} with an oxygen stoichiometry (O^{2-}/Pu^{ox}) of 1.81. After 600 minutes, the oxide film is essentially all Pu^{3+} with an oxygen stoichiometry (O^{2-}/Pu^{ox}) of 1.45, closer to the value expected for plutonium sesquioxide (Pu_2O_3; O^{2-}/Pu^{ox} = 1.5) and higher than was seen for similar experiments conducted on clean surfaces.

The diffusion needed to maintain the AR reaction of PuO_2 is thought to be driven by the chemical potential gradient across the oxide [6]. At a low enough temperature the conversion of Pu^{4+} to Pu^{3+} ceases as the diffusion of oxygen through the oxide becomes too slow to be measurable within the timescale of the experiment. As part of the work in this investigation, this temperature has been determined to be ~ -20^o C. Thus, cooling a carbide-contaminated Pu surface below -70^o C and exposing it to 590 *L* of oxygen forms a stable PuO_2 film (i.e. a dioxide film that does not undergo AR), as illustrated in the initial stage (first ~60 minutes) of Figure 5.8. During the first 25 minutes of the experimental run, the temperature was maintained below -70^o C to confirm the stability of the oxide film formed at this temperature. Afterwards, the temperature was slowly increased to room temperature over a period of several hours. Initially, and through the first ~160 minutes of the experiment, plutonium metal can still be observed in the Pu 4f XP spectra indicating a thinner film than the one produced from the 235 *L* exposure at room temperature. The initial oxide composition is not appreciably different than that of the room temperature exposure: 0.65:0.35 Pu^{4+}:Pu^{3+} with an oxygen stoichiometry (O^{2-}/Pu^{ox}) of 1.83. As the temperature slowly increases, the AR reaction begins converting

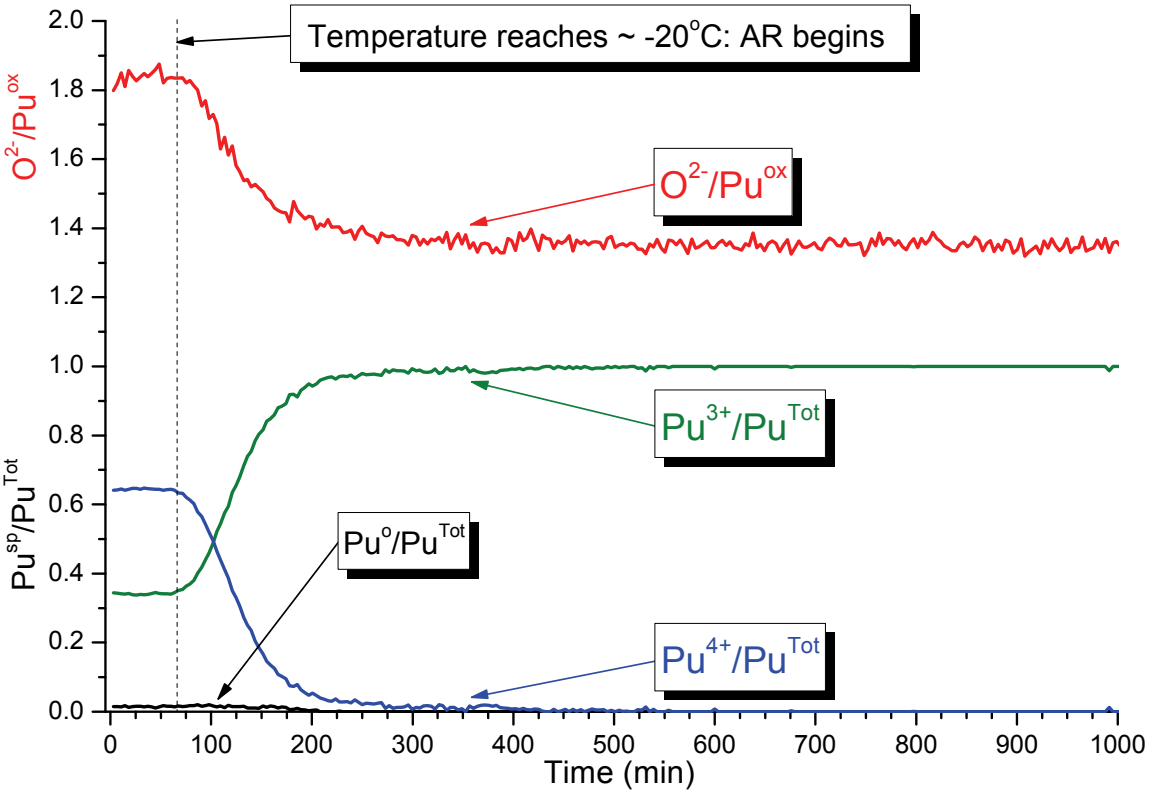

Figure 5.8: Auto-reduction (AR) reactions of plutonium dioxide film grown on carbide-contaminated metal: 590 *L* exposure at < -70° C. Below a temperature of ~ -20° C (dashed line at ~70 minutes) the AR reduction does not occur and the dioxide film is stable.

plutonium from Pu^{4+} to Pu^{3+} at approximately -20° C (dashed line in Figure 5.8, ~70 minutes) with a concomitant decrease in O/Pu stoichiometry. When the reaction has reached completion (> 400 minutes), all the plutonium is in the 3+ oxidation state with a final stoichiometry of O^{2-}/Pu^{ox} = 1.35, lower than the final stoichiometry observed for the undoubtedly thicker oxide film in Figure 5.7. When the experiment was repeated, a second sub-ambient temperature oxygen exposure experiment (1000 *L* at < -70° C) on a clean metal surface yielded comparable results: 0.68:0.32 Pu^{4+}:Pu^{3+} with O^{2-}/Pu^{ox} of 1.84

and a final film composition of 100% Pu^{3+} with O^{2-}/Pu^{ox} of 1.30. The metallic component (~4%) was observed in the Pu 4f XP spectra, indicating a thin oxide film, approximately the same thickness (~50 Å) as the film formed from the 590 *L* exposure on the carbide-contaminated Pu surface. The relatively thin nature of the plutonium oxide films produced at low temperature exposures (< -70° C) on carbide-contaminated and clean surfaces may be the reason for the similar final stoichiometries, 1.35 vs. 1.30, respectively.

The initial Pu 4f and O 1s photoelectron spectra corresponding to the beginning of

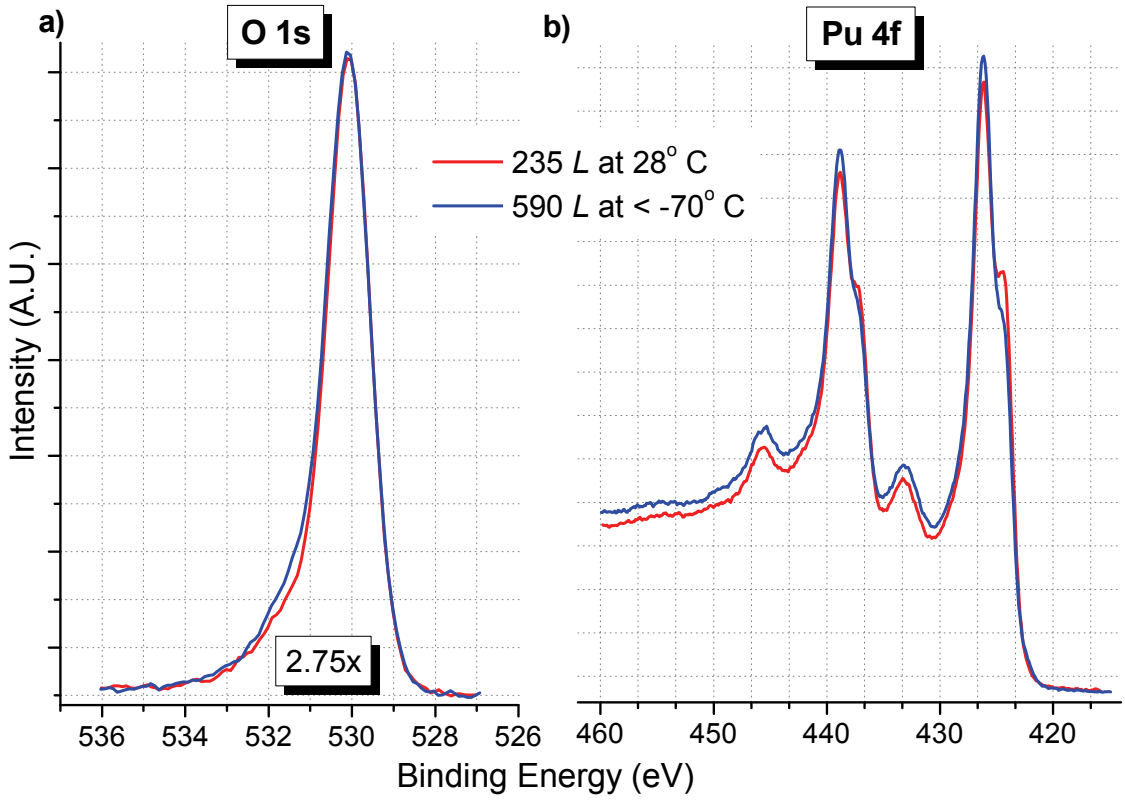

Figure 5.9: Initial (a) O 1s and (b) Pu 4f XP spectra for AR reactions of 235 *L* O_2 exposure at 28° C (red trace) and 590 *L* O_2 exposure at < -70° C (blue trace) shown in Figure 5.7 and 5.8. The spectra are normalized to the Pu 4f area.

the AR reaction experimental runs of the 235 *L* (28° C) and 590 *L* (< -70° C) exposures (Figure 5.7 and 5.8, respectively) are shown in Figure 5.9. The Pu 4f spectrum collected during the end of the room temperature 235 *L* exposure has slightly less Pu^{4+} component than the 590 *L* exposure (60% versus 65%), presumably because the latter occurred at a higher dose and at low temperatures where diffusion/AR reaction does not proceed while the former was at room temperature where the auto-reduction reaction readily occurs converting Pu^{4+} to Pu^{3+}. For both films, the O 1s spectra exhibit a similar oxide peak

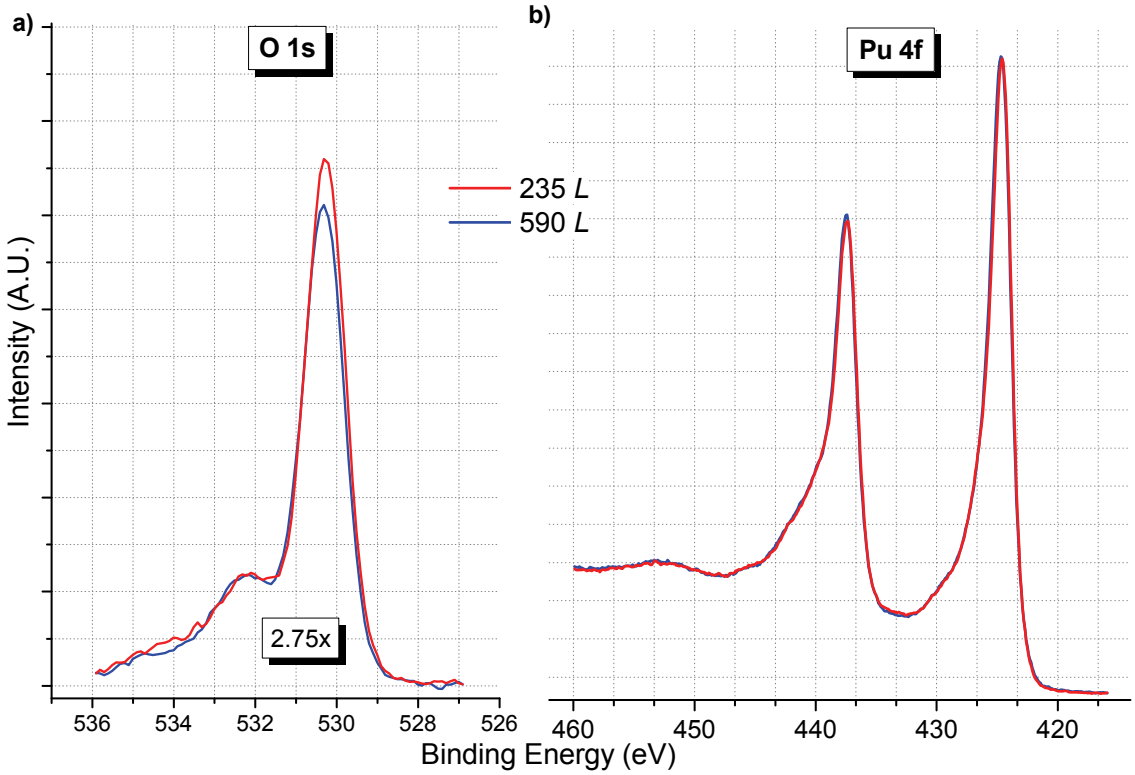

Figure 5.10: The final (a) O 1s and (b) Pu 4f XP spectra for oxide films after the completion of (600 minutes) the AR reactions shown in Figure 5.7 and 5.8: 235 *L* (red trace) and 590 *L* (blue trace). The spectra, acquired at 28° C, are normalized to the Pu 4f area.

shape (529.8 eV) while the low temperature exposure has a slightly more intense shoulder at 532.2 eV, likely due to adsorption of more contaminants at the lower temperature. The corresponding Pu 4f and O 1s spectra for these oxide films at the end of the two AR reactions (~600 min.) are shown in Figure 5.10. While the Pu 4f spectra of the two oxide films are very similar (so much so that it is difficult to differentiate the two in Figure 5.10b), the corresponding O 1s spectra (Figure 5.10a) show identical surface contaminant peaks at 532.2 eV (discussed below) but different intensities for the oxide peak at 530.3 eV, indicating different stoichiometries, as shown in Figure 5.7 and 5.8. The variable oxide oxygen intensity and identical surface contaminant intensity observed here suggests that the peak at 532.2 eV is not the reason for these sub-stoichiometric oxide films.

Figure 5.11 presents a comparison of O 1s, Pu 4f, and C 1s spectra of a carbide-contaminated Pu surface exposed to an oxygen dose of 30 *L* immediately after the exposure and six hours later. The two Pu 4f spectra are very similar, with both showing Pu in the 3+ oxidation state. The spectrum acquired right after the exposures shows an additional amount of intensity at ~433.1 eV between the Pu $4f_{5/2}$ and the $4f_{7/2}$ doublet. The $4f_{7/2}$ satellite for Pu^{4+} is located at this binding energy [10]. Thus, this additional intensity is likely indicative of the presence of a very small amount of Pu^{4+}. The initial oxygen stoichiometry (O^{2-}/Pu^{ox}) for the film is 1.49. After six hours, the stoichiometry decreases to 1.36. Immediately after the oxygen exposure, the O 1s XP spectrum shows a single peak at 530.2 eV corresponding to the oxide oxygen. Analysis of the same film six hours later indicates that a new feature has appeared at 532.2 eV. That this additional

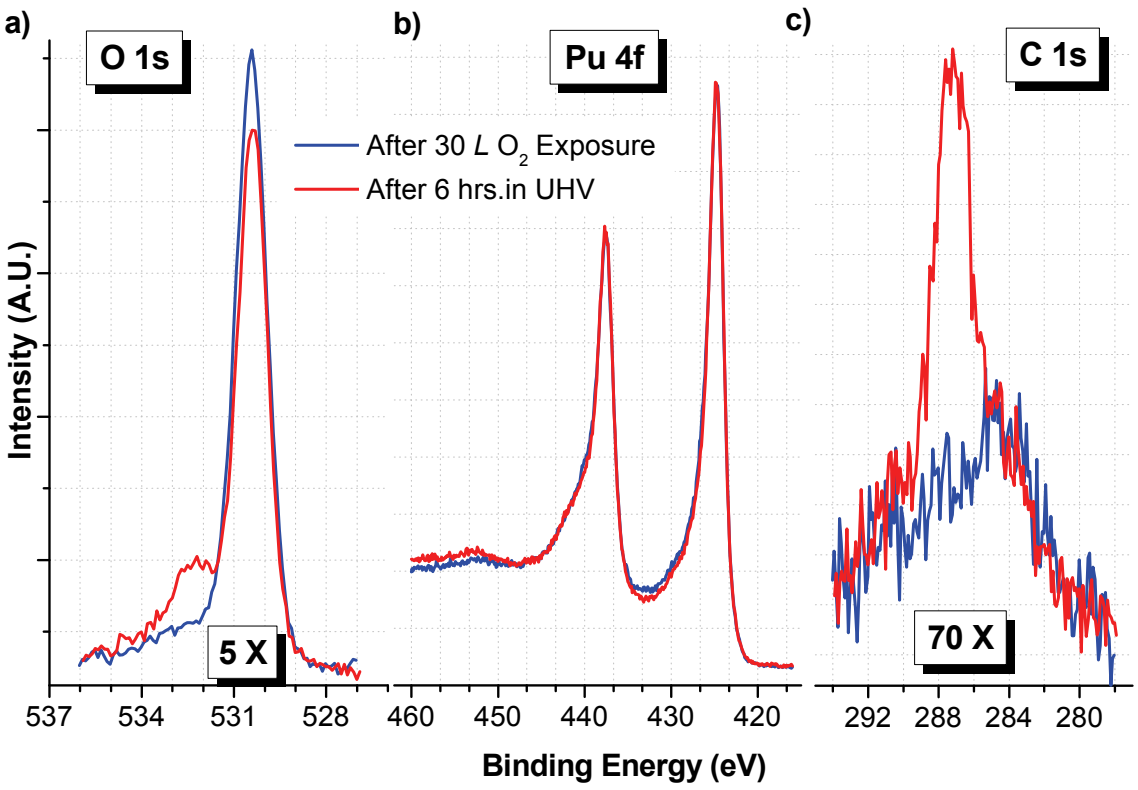

Figure 5.11: (a) O 1s, (b) Pu 4f, and (c) C 1s spectra of a carbide-contaminated Pu surface exposed to 30 *L* of oxygen. The blue trace indicates the spectra acquired five minutes after the dose was completed. The red trace represents the spectra obtained after an additional 6 hrs in UHV. The spectra are normalized to the Pu 4f area.

feature is not the cause of the changing stoichiometry of these oxide films was discussed above. It should be noted that this small peak appearing at 532.2 eV is typically attributed to surface hydroxyls [11]. However, upon examination of the corresponding C 1s XP spectra for this oxide film, it is clear that the peak at 532.2 eV for oxygen appears simultaneously with a carbon peak at 287.1 eV. The high binding energy of this feature may suggest that these peaks are due to adsorption of a carbon-oxygen containing species after exposure to UHV (~$5*10^{-10}$ Torr) for six hours. Residual gas analysis (RGA) shows

the presence of CO (28 a.m.u.) as one of the main contaminants of the vacuum system. Quantification of the oxygen peak at 532.2 eV and the carbon peak at 287.1 eV indicate a C:O ratio of ~1. Both of these peaks have been observed to simultaneously disappear after a light sputtering of the surface.

The presence of carbon within the oxide, as an oxy-carbide, has been shown to result in significant sub-stoichiometry of plutonium oxide films [12]. XPS and AES data for carbon acquired during these experiments show that the sub-stoichiometric plutonium sesquioxide films prepared for this work do not contain carbide impurities within the depth being analyzed, similar to the data of the sub-stoichiometric films presented in the previous chapter. The carbide contamination initially observed on the plutonium metal surfaces (C 1s region shown on Figure 5.6b, blue trace) quickly becomes undetectable upon exposure to oxygen (blue trace in Figure 5.11c), as probed by XPS and AES, indicating that the carbide likely remains at the metal-oxide interface and is not distributed throughout the thickness of these prepared oxide films.

Carbidic impurities on Pu surfaces appear to affect the extent of reduction in the AR reaction for similar oxygen exposures at room temperature. Clean metal surfaces exhibiting very little carbide contamination yield oxide films (Figure 5.3-5.5) of even lower stoichiometries (O/Pu=1.1-1.27), as observed by both AES and XPS, than those observed on metal surfaces with larger amounts of carbide impurities, shown in Figure 5.8. The Pu 4f XP spectra of the oxide films produced by the AR reaction, regardless of

the level of contamination or extent of reduction, show a binding energy of 424.4 eV (characteristic of trivalent Pu) and no discernable difference in peak shape.

The thermodynamic parameters of an oxide film on a metal substrate are clearly different from bulk oxides. Specifically, PuO_2 is a stable oxide in bulk whether in an air [13] or in an inert atmosphere [11]. A PuO_2 film on Pu metal, however, is stable in air but not in an inert atmosphere, e.g., UHV, where rapid reduction from Pu^{4+} to Pu^{3+} occurs at room temperature. Notwithstanding the different thermodynamic stability between a bulk oxide and an oxide film, it can be useful to examine the oxygen-metal phase diagram for insight into the oxidation of the metal. The phase diagram for the plutonium-oxygen system has been extensively studied [13-17]. A diagram presented by Boivineau [16] indicates the existence of a sub-stoichiometric Pu_2O_{3-y} species. Unfortunately, there was little discussion on the nature of this oxide. Courteix published one of the first XPS investigations of plutonium oxides [4] in which binding energy shifts were employed to suggest that plutonium sesquioxide may exist in sub-stoichiometric form. In that study, however, there was no attempt to measure the oxygen- plutonium atomic concentrations of the oxide films. As was shown in the previous chapter of this work, sub-stoichiometric oxide films of plutonium can be grown when the metal is subjected to small oxygen exposures. Sub-stoichiometric oxides of metals have been reported to occur at the very initial stages of oxidation [18]. The auto-reduction of oxide films can occur at elevated temperatures which facilitates the diffusion of oxygen [19]. The work presented here describes a stoichiometric plutonium dioxide auto-reducing not to the expected sesquioxide (Pu_2O_3) but to a sub-stoichiometric sesquioxide (Pu_2O_{3-y}) during exposure to

UHV at room temperature. It is conceivable that the self-irradiation of plutonium by α-particle decay [20] may be the cause of this unusual behavior. However, it cannot be the sole cause as radioactive decay is a process independent of temperature while the auto-reduction of Pu has clearly been shown in this chapter to be temperature dependent.

5.3 Conclusions

The data presented in this chapter clearly show that sub-stoichiometric sesquioxide (Pu_2O_{3-y}) can be obtained from AR of PuO_2 films. While the stoichiometry of the oxide film prepared is less than what is expected for plutonium sesquioxide (O/Pu = 1.5), the character of the plutonium cation appears to remain trivalent. In addition, there is a range of observed stoichiometries from 1.15 to 1.5. These sub-stoichiometric sesquioxide films observed during the oxidation of plutonium metal substrates may be better described as Pu_2O_{3-y} rather than Pu_2O_3 to differentiate them from the plutonium sesquioxides (α and β-Pu_2O_3) observed in bulk oxides as powders [14]. It is clear now that the plutonium oxide film on metal surface system is much more complex than previously thought. The level of sub-stoichiometry depends on initial film thickness and carbide contamination. Based on these results and the high reactivity of plutonium towards oxygen, it is not unreasonable to expect this sub-stoichiometric behavior (Pu_2O_{3-y}) near the oxide-metal interface of oxide films on Pu metal substrates.

References

[1] Butterfield, M. T., Durakiewicz, T., Guziewicz, E., Joyce, J. J., Arko, A. J., Graham, K. S., Moore, D. P., Morales, L. A., *Surface Science*, **571** (2004) 74.

[2] Larson, D. T. and Cash, D. L., *J. Phys. Chem.*, **73** (1969) 2814.

[3] Larson, D. T., *J. Vac. Sci. Technol.*, **17** (1980) 55.

[4] Courteix, D., Chayrouse, J., Heintz, L., Baptist, R., *Solid State Comm.*, **39** (1981) 209.

[5] Haschke, J. M., Allen, T. H., Morales, L. A., *Los Alamos Science*, **6** (2000) 252.

[6] Martz, J., Haschke, J. M., Stakebake, J. L., *J. Nucl. Mater.*, **210** (1994) 130.

[7] Morrall, P., Tull, S., Glascott, J., Roussel, P., *J. Alloy. Compd.*, **444-445** (2007) 352.

[8] Colmenares, C. A., *Prog. Solid State Chem.*, **9** (1975), 139.

[9] Gouder, T., Havela, L., Schick, A. B., Huber, F., Wastin, F., and Rebizant J., *J. Phys.: Condens. Matter*, **19** (2007) 476201.

[10] Baptist, R., Courteix, D., Chayrouse, J., Heintz, L., *J. Phys. F:Met. Phys.*, **12** (1982) 2103.

[11] Farr, J. D., Schulze, R. K., Neu, M. P., *J. Nucl. Mater.*, **328** (2004) 124.

[12] Larson, D. T. and Haschke, J. M., *Inorg. Chem.*, **20** (1981) 1145.

[13] Chikalla, T. D., McNeilly, C. E., and Skavdahl, R. E., *J. Nucl. Mater.*, **12** (1964) 131.

[14] Gardner, E. R., Markin, T. L., and Street, R. S., *J. Inorg. Nucl. Chem.*, **27** (1965) 541.

[15] Wriedt, H. A., *Bull. Alloy Phase Diagr.*, **11** (1990) 184.

[16] Boivineau, J. C., *J. Nucl. Mater.*, **60** (1976) 31.

[17] Predel, B., O-Pu (Oxygen-Plutonium). Madelung, O. (ed.). Springer Materials: *The Landolt-Börnstein Database- Group IV Physical Chemistry. Numerical Data and Functional Relationship in Science and Technology*, **51**.

[18] Kurth, M., Graat, P. C. J., Mittemeijer, E. J., *Thin Solid Films*, **500** (2006) 61.

[19] Roosendaal, S. J., Vredenberg, A. M., Habraken, F. H. P. M., *Phys. Rev. Lett.*, **84** (2000) 3366.

[20] Wick, O. J., Plutonium Handbook- A Guide to the Technology, Vol. I & II, (American Nuclear Society: 1980).

Chapter 6: The Role and Fate of Impurities in Plutonium Oxidation

6.1 Gallium in Plutonium Metal

Impurities can have dramatic effects in the properties of a material. They can be either intentionally included or an inherent consequence of a process. Small amounts of impurities, or 'dopants', added to silicon or germanium produce dramatic changes in their electrical property**.** Iron is susceptible to oxidation, which can compromise the structural integrity of machined components, but forms alloys highly resistant to corrosion with the addition of varying amounts of chromium, molybdenum and nickel [1]. The decay of radioactive materials incorporates impurities in the metal in the form of daughter products, americium and uranium in the case of Pu. Plutonium metal forms six crystalline solid phases, yet the addition of a small percentage of gallium (Ga) renders the face-

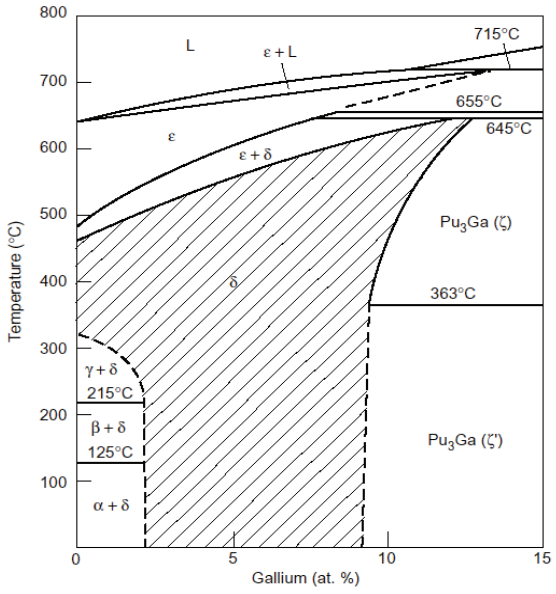

Figure 6.1: Ga-Pu binary phase diagram illustrating the stabilization of the Pu δ–phase with the addition of Ga [2].

centered cubic phase stable over a range of over 500^{o} C, as can be seen in the Ga-Pu phase diagram presented in Figure 6.1.

There have been several studies investigating the effect of gallium in the electronic configuration and structure of δ-Pu [4-7]. Gallium atoms have been confirmed to be in substitution on the plutonium f.c.c. lattice where hybridization occurs between the Ga $4p_{3/2}$ and Pu $5f_{5/2}$ bands. Very little is known, however, regarding the role of gallium during the oxidation of δ-Pu. The low concentration of Ga (~2 at. %) makes it difficult to be observed with XPS. In fact, the strongest Ga XPS signal, the Ga $2p_{3/2}$ transition lies very near the Pu $4p_{3/2}$ signal, as shown in Figure 6.2, complicating the detection. Additionally, the gallium can only be detected with XPS when the Pu 4f peaks are indicative of Pu metal and the C 1s and O 1s regions exhibit very little signal. Table 6.1 lists the binding energies for the $2p_{3/2}$ transition of pure gallium as well as various compounds. While the electron spin orbit splitting (S.O.S) of the Ga-Pu alloy is the same as pure Ga (27.0 eV), the binding energy of the $2p_{3/2}$ is lower for Ga-Pu than pure gallium (1115.3 vs. 1116.5 eV) indicating less tightly bound Ga 2p core electrons for the Pu alloy.

6.2 Gallium in Plutonium Oxide

Figure 6.3 shows the XP spectra of the Ga $2p_{3/2}$, O 1s, and Pu 4f regions of a ~2 at. % Ga-Pu metal surface as it is exposed to small amounts (0 to 4.0 *L*) of O_2 at 10^{-8} Torr. With each exposure of O_2, the O 1s signal increases and the Pu 4f region shows

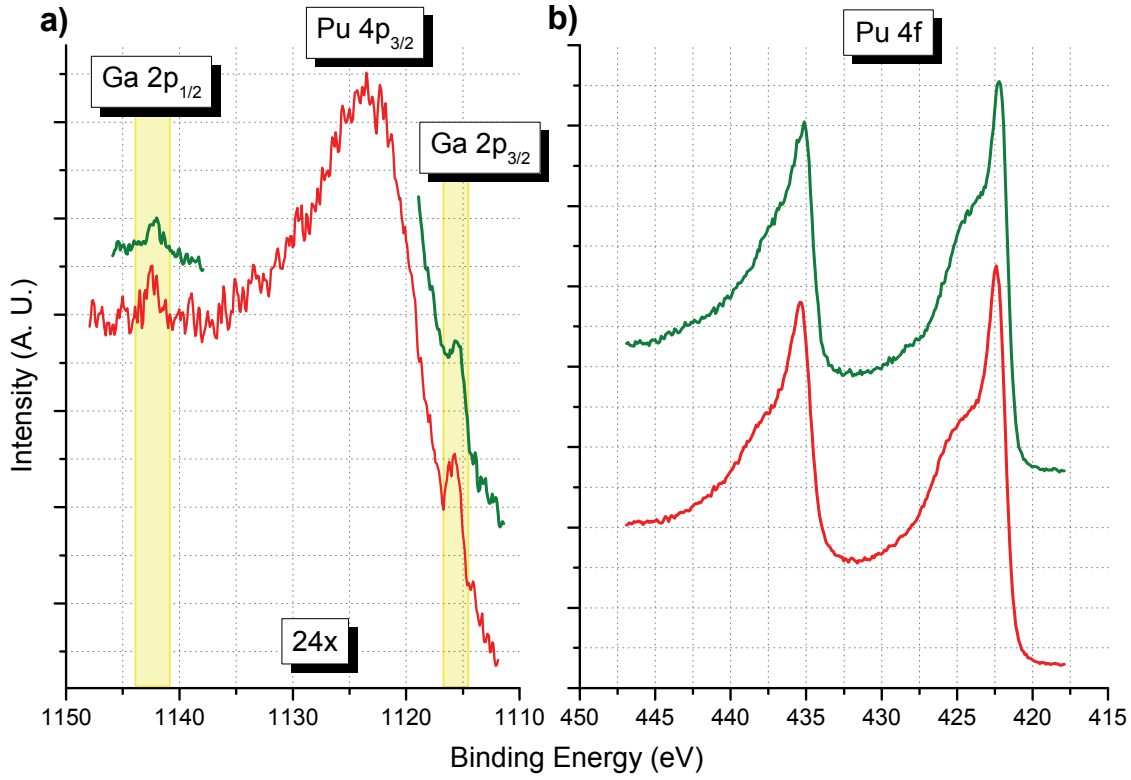

Figure 6.2: XP spectra of the **a)** Ga 2p and **b)** Pu 4f regions for clean ~2 at. % Ga-Pu metal surfaces. The Ga 2p doublet (red traces) occurs near the Pu $4p_{3/2}$ signal making quantification of the Ga $2p_{3/2}$ in the steep background challenging. The green traces shows another clean Pu surface XP spectrum where only the region near the Ga 2p signal was acquired, as a means of minimizing acquisition time.

Table 6.1: Binding energies for the $2p_{3/2}$ transition for various Ga compounds [8].

	Binding Energy for $2p_{3/2}$ Transition (eV)
δ-Pu (2.0 at.% Ga)	1115.3 (S.O.S. = 27.0 eV)
Ga	1116.5 (S.O.S. = 27.0 eV)
GaP	1116.8
GaAs	1117.0
Ga_2O_3	1117.5
GaN	1117.8

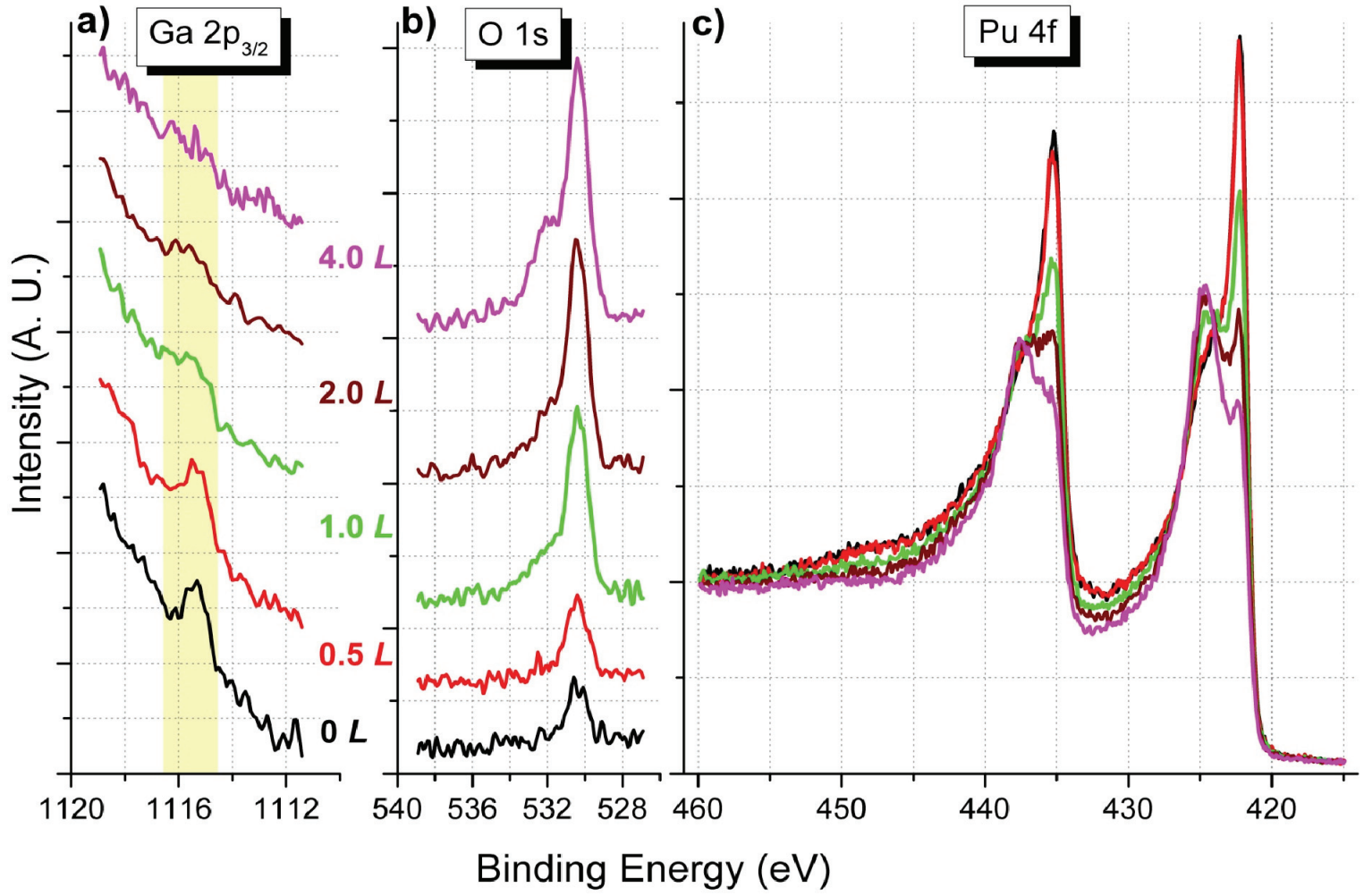

Figure 6.3: XPS Analysis of a clean metal surface exposed to 0-4.0 *L* O_2 at 10^{-8} Torr. The lower traces (black) in the three spectral regions, **a)** Ga $2p_{3/2}$, **b)** O 1s, and **c)** Pu 4f, corresponds to the clean metal surface before O_2 exposure. For the Ga 2p, only the $2p_{3/2}$ signal was examined, to minimize acquisition times in the experiment.

increased intensity at 424.4 eV (Pu^{3+} species) at the expense of the peak intensity at 422.2 eV (Pu^0 species). The Ga $2p_{3/2}$ signal at 1115.3 eV quickly decreases with increasing O_2 exposure. After 4.0 *L* O_2, the Pu 4f signal (magenta, upper traces) is composed of ~ 60% Pu^0 and ~40% Pu^{3+} while the Ga $2p_{3/2}$ peak is barely detectable. It must be noted that because of the difference in electron binding energies of Pu and Ga, the XPS probing depths are significantly different for each element. Utilizing the *TTP-2M* method of calculating electron inelastic mean free path (IMFP), the probing depth for Pu (*B.E.* ~ 424 eV; *K.E.* ~ 1063 eV) and Ga (*B.E.* ~ 1115 eV; *K.E.* ~ 372 eV) is 54 Å and 26 Å, respectively [9]. Close inspection of the Ga $2p_{3/2}$ signal appears to show the emergence of a signal at ~1116 eV with O_2 exposure, particularly at the 1.0 *L* (green trace) and the 2.0 *L* (wine trace) perhaps indicating the oxidation of gallium. However, the lack of a reference binding energy value for Ga^{3+} (in the Ga-Pu alloy system) and the weak Ga $2p_{3/2}$ signal strength are not conducive for allowing a determination of the oxidation state of Ga with a reasonable degree of confidence.

While weak to begin with, the Ga $2p_{3/2}$ signal peak can unmistakably be observed decreasing as an oxide layer grows on the clean Pu metal surface with O_2 exposure. This data can be used to determine what the fate of Ga is during the oxidation of Pu. There are several possibilities: 1) Ga segregates to the surface during oxidation, 2) Ga remains in the Pu oxide film, 3) Ga is enriched at the oxide-metal interface. If the Ga segregates to the surface, the Ga $2p_{3/2}$ peak should increase with O_2 exposure. The results presented in Figure 6.3a show the Ga $2p_{3/2}$ signal is at a maximum when the amount of Pu oxide present is at a minimum. A Pu oxide film with the same concentration of Ga as the metal

(~ 2 at. %), would exhibit a Ga $2p_{3/2}$ signal intensity independent of O_2 exposure, after a small initial signal decrease due to the lower relative atomic concentration of Ga in the oxide than in the Pu metal. The only plausible explanation for the vanishing Ga $2p_{3/2}$ signal is for the Ga atoms to remain at the metal-oxide interface during oxidation of Pu metal. It is also possible that while the oxide-metal interface becomes Ga enriched during oxidation, some Ga remains within the oxide. AES investigations of Ga in Pu oxide films indicate that while significantly depleted of Ga, the oxide does exhibit a weak, but detectable Ga *LMM* Auger signal at a kinetic energy of ~1068 eV [10].

6.3 Carbon Impurities in Plutonium Metal

A second impurity, albeit unintended, commonly found in Pu metal is carbon, typically in the form of an oxy-carbide, $PuO_{0.5}C_{0.5}$ [11, 12]. The carbon is an intrinsic contaminant of the process of plutonium synthesis and manufacturing [13]. In an earlier chapter, small amounts of carbide on the Pu metal surface were shown to influence the level of sub-stoichiometry of the Pu sesquioxide. The sample used for those studies, was a Pu research sample low in contaminants. It would be interesting to also investigate how higher levels of carbon contaminants affect Pu oxidation.

Figure 6.4 shows the XP spectrum of a plutonium sample with a thin film of carbon and oxygen quantified as $PuO_{0.5}C_{0.5}$. While the quantification implies that it is an oxycarbide, there are two peaks in the C 1s region indicating two different carbon species. In bulk phases, there are four stable Pu carbide species: Plutonium sesquicarbide (Pu_2C_3), triplutonium dicarbide (Pu_3C_2), and PuC_{1-x}. Plutonium dicarbide (PuC_2) is only

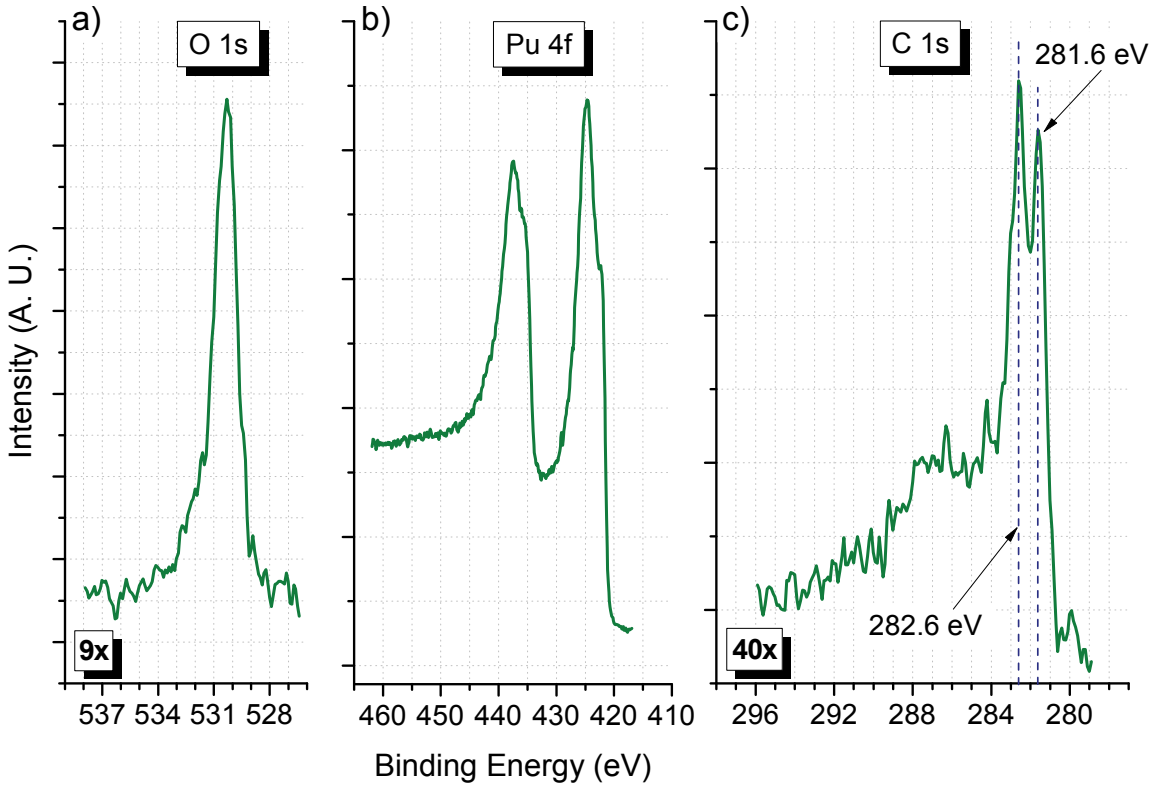

Figure 6.4: XP spectra of the **a)** O 1s **b)** Pu 4f and **c)** C 1s regions for a Pu metal sample with a thin layer of oxy-carbide, $PuO_{0.5}C_{0.4}$. Both of the C 1s signals observed (282.6 eV and 281.6 eV) were included in the quantification. The Pu 4f region shows approximately 50% Pu^0, 50% Pu^{3+}.

stable above 1,660° C [14]. One XPS study investigating the 5f electronic states variability of Pu carbides [15] reported the energy for the C 1s signal of PuC_{1-x} as 282.6 eV. The energy for the Pu oxycarbide has been reported to be a broad peak centered on 281.0 eV. [11]. Figure 6.5 shows the XP spectrum of a Pu surface with small amounts of carbon and oxygen ($PuO_{0.12}C_{0.18}$) contamination. The C 1s region exhibits a peak at 281.6 eV with a small shoulder at 282.6 eV peak. While both of these C 1s features are observed in Figure 6.4 and Figure 6.5 at different intensities, the Pu 4f region presented

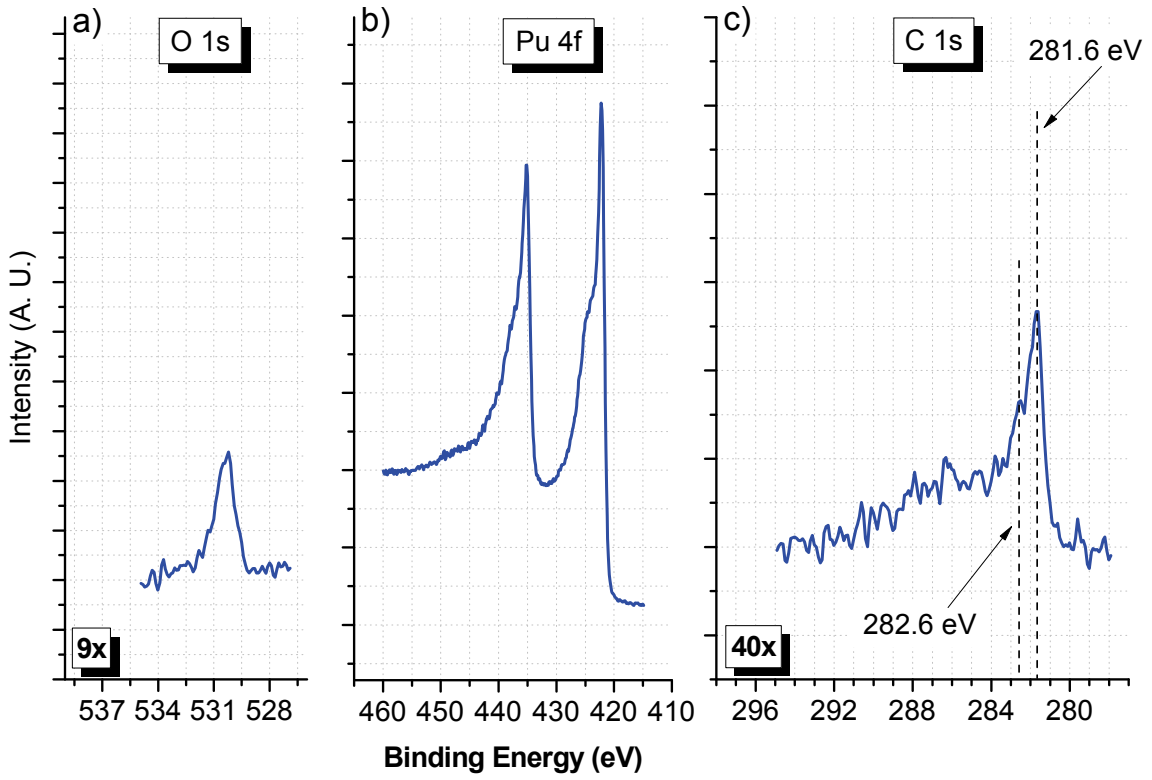

Figure 6.5: XP spectra of the **a)** O 1s **b)** Pu 4f and **c)** C 1s regions for a Pu metal sample with a thin layer of oxygen-carbon contamination, $PuO_{0.12}C_{0.18}$. Both of the C 1s signals observed (282.6 eV and 281.6 eV) were included in the quantification. The Pu 4f region shows approximately 90% Pu^0 with a small amount of oxidized Pu signal.

in Figure 6.4b indicates that the surface has a Pu composition approximately 50% Pu^{3+}; Figure 6.5b shows a surface predominantly metallic with very little Pu^{3+}.

Figure 6.6 illustrates oxidation of a Pu metal surface, of similar composition to the surface presented in Figure 6.5, with 30 *L* of O_2. The initial spectra (red trace) exhibit the two carbide species at 281.6 eV and 282.6 eV. After exposure to oxygen (green trace), these features disappear. The Pu 4f and O 1s regions are indicative of an oxide film with 100% Pu^{3+}. This result has been confirmed with AES experiments. Figure 6.7

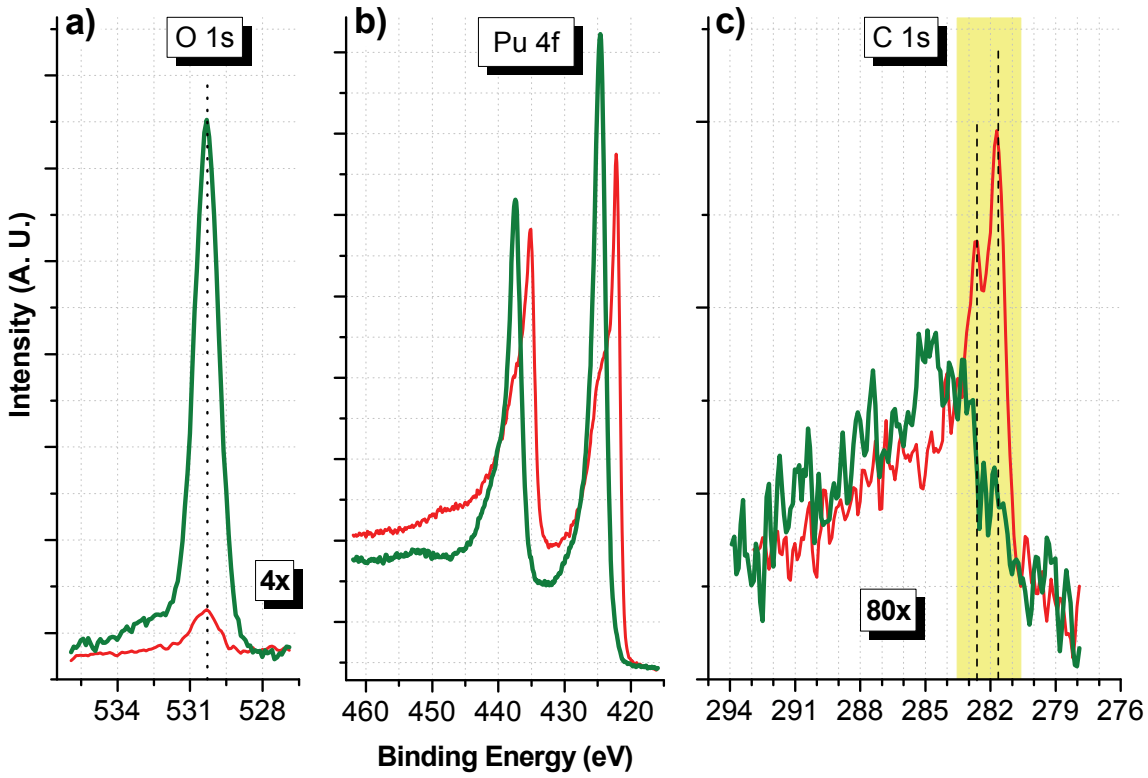

Figure 6.6: XP spectra of the **a)** O 1s **b)** Pu 4f and **c)** C 1s regions for a Pu metal sample with a thin layer of oxygen-carbon contamination, before (red trace) and after (green trace) a 30 *L* O_2 exposure . The Pu 4f region showing approximately 90% Pu^0 initially, becomes 100% Pu^{3+}. Both of the C 1s signals observed (282.6 eV and 281.6 eV) in Figure 6.4 and Figure 6.5, disappear after the O_2 exposure.

presents the AES in-situ oxidation of a clean Pu metal surface ($PuO_{0.01}C_{0.03}$) with 30 *L* O_2. The Pu *NOV* signals exhibits a small kinetic energy shift from 317 eV to 314 eV. The evolution of the O *KLL* signal highlights the growth of the oxide. The C *KLL* indicates there is no carbon accumulation throughout the duration of the O_2 exposure.

Figure 6.8 show the results of an AES in-situ experiment where a thin Pu oxycarbide layer on metal ($PuO_{0.5}C_{0.5}$) was exposed to 30 *L* of O_2. Carbon and oxygen can be detected in the spectra before the beginning of the O_2 exposure (red trace, labeled

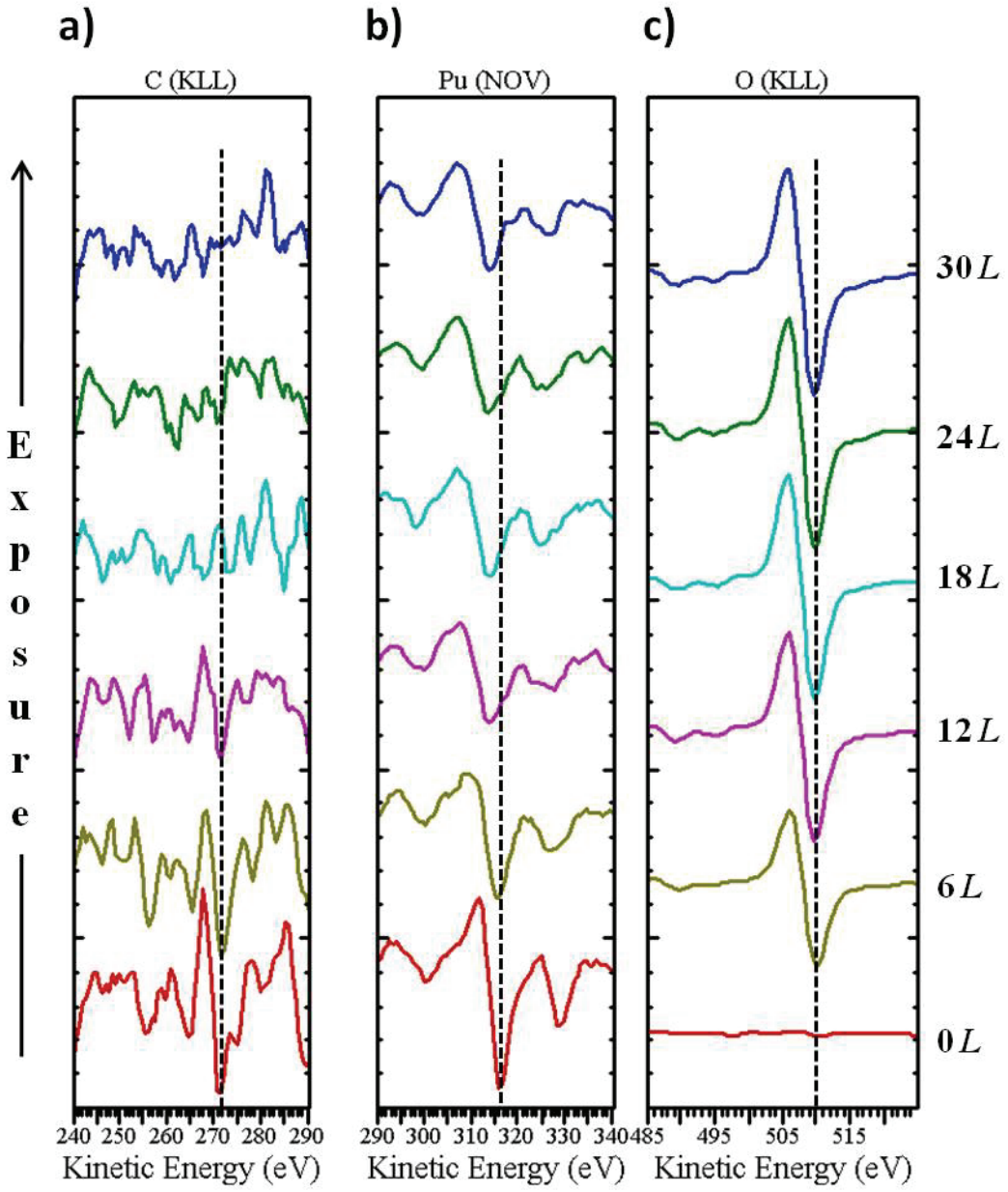

Figure 6.7: Differentiated AE spectra of the **a)** carbon *KLL* **b)** Pu *NOV* and **c)** oxygen *KLL* transitions acquired during an in-situ 30 *L* O_2 exposure of a clean Pu metal surface, $PuO_{0.01}C_{0.03}$. The Pu surface before O_2 exposure is shown at the bottom of the figure (red trace). A set of spectra was collected at intervals of 6 *L*. There is a weak signal for carbon indicative of carbide. The Pu *NOV* exhibits a kinetic energy shift from 317 eV to 314 eV as the Pu metal surface is oxidized.

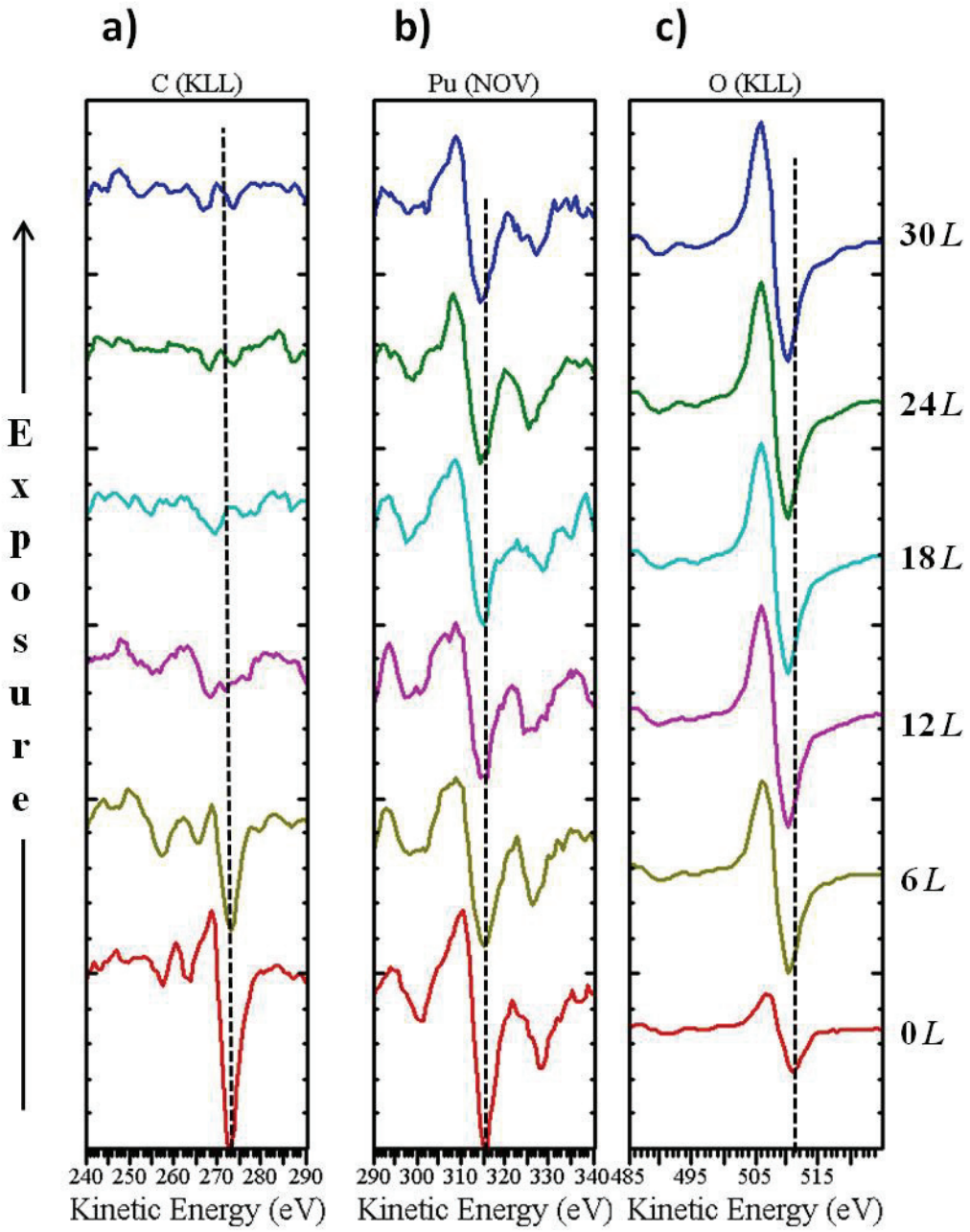

Figure 6.8: Differentiated AE spectra of the **a)** carbon *KLL* **b)** Pu *NOV* and **c)** oxygen *KLL* transitions acquired during an in-situ 30 *L* O_2 exposure of a Pu oxy-carbide film on metal, $PuO_{0.5}C_{0.5}$. The Pu surface before O_2 exposure is shown at the bottom of the figure (red trace). A set of spectra was collected at intervals of 6 *L*. The Pu *NOV* exhibits a kinetic energy shift from 316 eV to 314 eV as the surface is oxidized. The carbon signal decreased in intensity as an oxide film develops on the Pu metal surface.

'0 *L*'). Once the oxidation begins, the O *KLL* signal increases, indicating the growth of an oxide layer, while the C *KLL* signal decreases. At the end of the O_2 exposure (top blue trace), the Pu *NOV* and the O *KLL* indicate a Pu oxide film. The C *KLL* signal has diminished considerably. The XPS and AES results indicate that the plutonium oxide grows above the oxycarbide layer, which stays near the oxide-metal interface.

If the oxycarbide layer remains at the oxide-metal interface, it is reasonable to

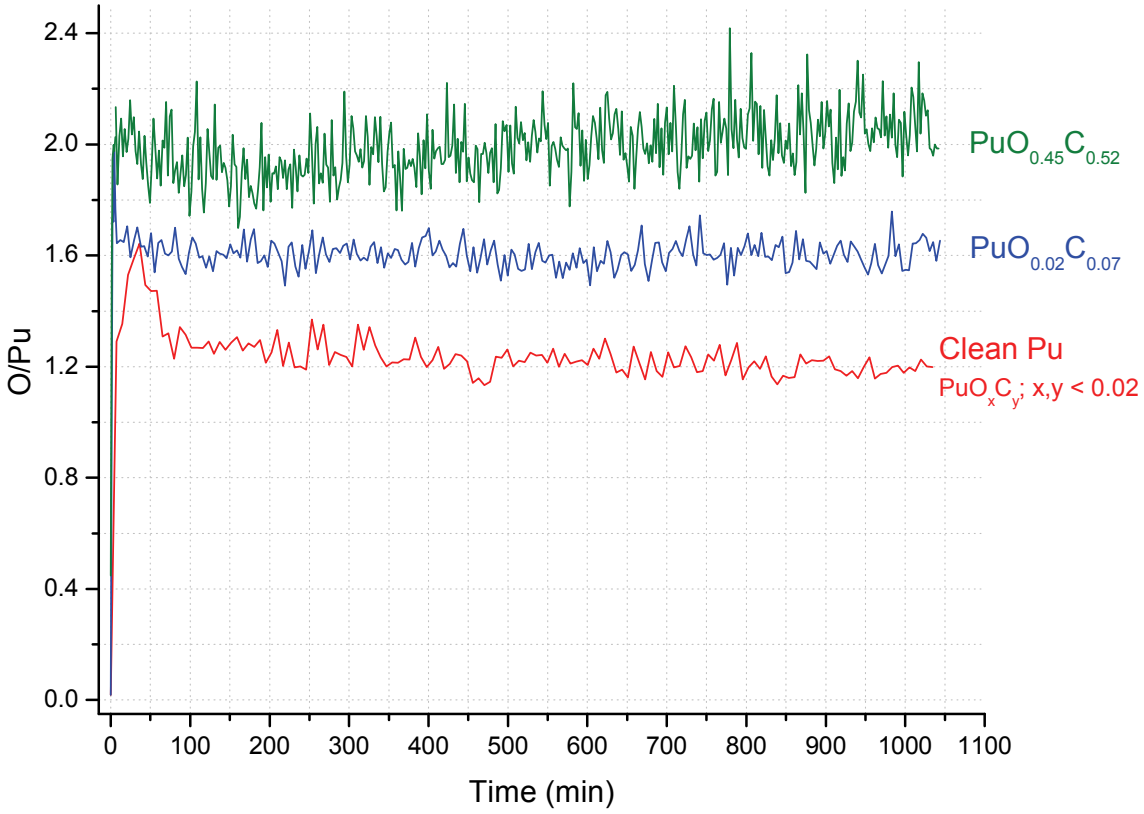

Figure 6.9: AES Pu oxide growth and evolution profile of Pu oxides. The three surfaces examined include a clean Pu metal surface (red trace), a Pu metal surface with a small oxycarbide contamination (blue trace), and a Pu oxycarbide layer on metal (green trace) exposed to 33, 30, and 30 *L* O_2, respectively. After the exposures, the surfaces' stoichiometries were monitored.

expect it to have an influence in the diffusion of oxygen into the metal. The AR of plutonium oxide, driven by the diffusion of oxygen into the metal is an ideal vehicle to probe the effect of an oxycarbide layer. Figure 6.9 shows the effect of the substrate on final stoichiometry of thin Pu oxide films. The clean Pu metal surface (red trace) exhibited a steady rise in stoichiometry (O/Pu) to 1.6. 450 min after the end of the exposure, the stoichiometry decreased to ~1.2, indicating a sub-stoichiometric Pu sesquioxide. The stoichiometry of the Pu surface with slight oxycarbide contamination (blue trace) peaks at ~2.0 after exposure. Once the exposure ends, the final stoichiometry of the film is O/Pu = 1.6. Upon exposure to oxygen, the oxycarbide surface (green trace) quickly reaches an O/Pu stoichiometry of 2.0 and remains at that level. The AR of PuO_2 does not occur to any appreciable extent. The fact that the oxycarbide layer remains near the oxide-metal interface region and the oxide grown on it seems impervious to the AR, suggest that the oxycarbide acts like a barrier to the diffusion of oxygen to the metal substrate, thereby stabilizing PuO_2 at the surface of Pu metal, under non-oxidizing conditions.

6.4 Conclusions

The $2p_{3/2}$ transition in the Ga-Pu alloy has been measured for the first time to be 1115.3 eV with a S.O.S. of 27.0 eV. While the S.O.S. is the same as elemental Ga, the binding energy for the transition is 1.2 eV lower in the Ga-Pu alloy. The binding energy difference may be due to the hybridization of the Ga $4p_{3/2}$ and Pu $5f_{5/2}$ bands that occurs in the Ga-Pu alloy, which is a different chemical environment than in elemental Ga. XPS experiments show that the concentration of Ga is not the same in the oxide as in the Pu

metal. Upon oxidation, the Ga XP signal disappears indicating that the Ga remains near the metal-oxide region.

Two peaks in the XPS C 1s region, carbide and oxy-carbide, have been resolved. XPS and AES experiments show that the oxycarbide species remains near the oxide-metal interface, upon oxidation of Pu. The presence of oxycarbide on the surface of Pu seems to have a stabilizing effect on oxide films, presumably by forming a barrier against oxygen diffusion through the oxide to the metal-oxide interface.

References

[1] Mathieu, H. J. and Landolt, D., *Corrosion Science*, **26** (1986) 547.

[2] Peterson, D. E., Kassner, M. E., *Bull. Alloy Phase Diagr.*, **9** (1988) 261.

[3] Hecker, S. S., *Los Alamos Science*, **6** (2000) 16.

[4] Deloffre, P. D., Truffier, J. L., Falanga, A., *J. Alloys Compd.*, **271** (1998) 370.

[5] Richard, N., Faure, Ph., Rofidal, P., Truffier, J. L., Bazin, D., *J. Alloys Compd.*, **271** (1998) 879.

[6] Faure, Ph., Deslandes, B., Bazin, D., Tailland, C., Doukhan, R., Fournier, J. M., Falanga, A., *J. Alloys Compd.* **244** (1996) 131.

[7] Conradson, S. D., *Appl. Spec.*, **52** (1999) 252.

[8] *NIST X-ray Photoelectron Spectroscopy Database*, NIST SRD 20, Ver. 3.5

[9] Tanuma, S., Powell, C. J., Penn, D. R., *Surf. Interfac. Sci.*, **35** (2003) 268.

[10] Private communications with A. Broach and Dr. D. P. Moore.

[11] Larson, D. T. and Haschke, J. M., *Inorg. Chem.*, **20** (1981) 1145.

[12] Terada, K., Meisel, R. L., Dringman, M. R., *J. Nucl. Mater.*, **30** (1969) 340.

[13] Wick, O. J., Plutonium Handbook- A Guide to the Technology, Vol. I & II, (American Nuclear Society:1980).

[14] Mulford, R. N. R., Ellinger, F. H., Hendrix, G. S., Albrecht, E. D., Plutonium 1960, (Cleaver-HumePress, London, U. K.: 1961) 301.

[15] Chemical Thermodynamics Vol. 4: Chemical Thermodynamics of Neptunium and Plutonium, OECD Nuclear Energy Agency, ed. (Elsevier Science B.V., The Netherlands: 2001) 427.

[16] Gouder T., Havela, L., Schick, A. B., Huber F., Wastin, F., and Rebizant, J., *J. Phys.: Condens. Matter*, **19** (2007) 476201.

Chapter 7: Conclusions

Plutonium is an element with fascinating physical properties and an unusually high reactivity toward other materials. Its peculiar behavior is attributed to the ability of the 5f electrons to be either localized or itinerant [1]. Because of the implications to safety, security, handling and storage stability, the oxidation of plutonium has been extensively studied. Despite many studies dealing with bulk plutonium oxidation by air, water vapor, and other gases, the dearth of fundamental knowledge regarding the behavior, and stability, of oxide films on the surface of plutonium is striking.

Before any surface science investigations of plutonium could occur, a reliable model for the analysis and quantification of XPS data had to be developed. The XPS 4f transition for plutonium 3+ was found to consist of an asymmetrical set of peaks with a set of satellites 16.4 eV from the main photoelectron signal. A relative sensitivity factor (R.S.F.) for an aluminum x-ray source was determined to be 22.68 for Pu. A reliable data fit model and an accurate RSF for analysis and quantification of plutonium is a prerequisite for meaningful interpretation of XPS data from plutonium surfaces. The model and RSF developed during the course of this thesis can be employed to analyze XPS data by any scientist, provided the basic data collection conditions and parameters that were used here are observed.

Sub-stoichiometric plutonium sesquioxide (Pu_2O_{3-y}) films on Pu metal surfaces under reducing environments have been identified and characterized for the first time. It has been established that the existence of sub-stoichiometric plutonium sesquioxides is

not due to carbon, in the form of an oxycarbide. The extent of sub-stoichiometry is a function of oxide film thickness. Very thin films exhibit stoichiometries as low as $PuO_{1.1}$. The stoichiometry of the Pu oxide films may be as high as $PuO_{1.5}$ for the thicker films. The variability of oxide stoichiometries suggests there may exist a large concentration gradient over the thickness of the Pu_2O_{3-y} rather than an uniform stoichiometry for the Pu_2O_3 film, as had been previously assumed before this work.

A detailed analysis of the auto-reduction (AR) of plutonium dioxide (PuO_2) produced some unexpected results. At temperatures less than -20^o C, the AR does not occur and PuO_2 thin films are stable. Within the O_2 pressure and temperature ranges investigated in the course of this dissertation ($5*10^{-8}$ to 10^{-4} Torr, < -70^o to 28^o C), the PuO_2 films grown on the metal did not exceed 20 Å in thickness. The final product of the AR of PuO_2 is not the sesquioxide (Pu_2O_3) as previously thought, but sub-stoichiometric sesquioxides (Pu_2O_{3-y}) where y = 0 - 0.7. The level of sub-stoichiometry depends on the initial thickness and in the amount of carbide contamination present on the surface of the metal.

During the oxidation of Pu, the gallium (Ga) added to stabilize the metal in the δ-phase has been shown to become depleted in the oxide and concentrated at the oxide-metal interface. The binding energy for the $2p_{3/2}$ transition of Ga found in the Ga-Pu alloy has been measured to be 1115.3 eV, a value lower than the value for elemental Ga. Oxycarbide and carbide contamination on the surface of Pu metal remains at the oxide-metal interface during oxidation as the oxide grows above it. Samples with an oxycarbide

layer on the Pu metal surface were shown to be resistant to the AR reduction of PuO_2, as it appears that the oxycarbide acts like a barrier preventing the diffusion of oxygen to the metal-oxide interface, thereby stabilizing the PuO_2.

Interpreted as a whole, the findings of the work presented here indicate that the nature of the oxide system on plutonium is far more complex than previously thought. The thin PuO_2 film on a thicker Pu_2O_3 layer becomes unstable under a reducing environment, auto-reducing not to the expected Pu_2O_3, but to a sub-stoichiometric sesquioxide (Pu_2O_{3-y}). The level of sub-stoichiometry depends on preparation, impurities and thickness of oxide. The level of contamination on the surface of Pu is critical to the stability of the oxide film.

Even though the findings of this investigation have advanced the understating of the nature of plutonium oxides on metal surfaces, new questions have emerged. In particular, why does the oxidation of plutonium yield PuO_2 films whose thickness is nearly constant (< 20 Å)? Under what conditions can this oxide form thicker films? Application of the different oxidation theories that do not depend in chemical potentials to drive the diffusion of oxygen, such as the Mott-Cabrera theory [2], or the Fromhold-Cook theory of coupled currents [3, 4], may help to develop a predictive model of Pu oxidation in the thin film regime. Carbon monoxide (CO) has been shown to readily oxidize Pu metal forming oxycarbide [5, 6]. Controlled exposure with CO should oxidized and cover the Pu metal surface with an oxycarbide layer. This could become a

controlled model system which can be employed to study the effect of oxycarbide on the oxidation of plutonium.

References

[1] Wills, J. M., Erikson, O., *Los Alamos Science*, **6** (2000) 128.

[2] Cabrera, N., Mott, N. F., *Rep. Prog. Phys.*, **12** (1948) 163.

[3] Roosendaal, S. J., Vredenberg, A. M., Habraken, F. H. P. M., *Phys. Rev. Lett.*, **84** (2000) 3366.

[4] Fromhold, A., Theory of Metal Oxidation, (North-Holland, Amsterdam, 1976)

[5] Larson, D. T. and Haschke, J. M., *Inorg. Chem.*, **20** (1981) 1145.

[6] Tull, S., *Ph.D.* Thesis, University of Wales, Cadiff, U. K., 2003.